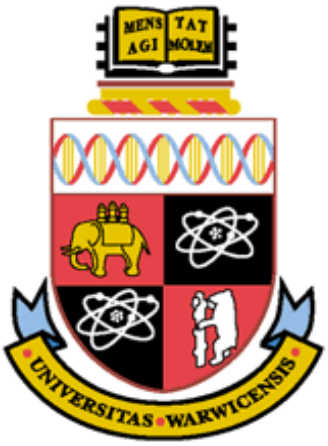

Bubble Dynamics under Dual-Frequency Acoustic Excitation

by

Yuning Zhang

Thesis

Submitted to the University of Warwick

for the degree of

Doctor of Philosophy

School of Engineering

April 2015

Contents

List of Tables

List of Figures

Acknowledgements

Firstly, I would like to show my deepest gratitude to Professor Shengcai Li, who has provided me excellent supervision, academic guidance and encouragements. I would also like to thank Dr. Duncan Billson for his help and valuable suggestions on the writing of this thesis. I would also acknowledge the financial support from China Scholarship Council and the tuition fee support from the School of Engineering, University of Warwick.

I would love to show special appreciations to my parents and my husband for their long-term and unconditional support and encouragements. Without them, I cannot finish this PhD thesis.

I would also like to thank Mr. Huw Edwards, Dr. Ting Chen and Dr. Ching-Hsien Chen for their kind help.

Last but not least, I would like to thank all my lovely friends, especially Xisha Chen, Yaru Chen, Yi Ding, Tianrong Jin, Chunzhi Ju, Xuqin Li, Huaiju Liu, Lei Wang, Zhongnan Wang, Wei Xing, Min Yang, Jinghan Zeng, Yan Zhang, Guanhua Zhang, and Yiming Zhang, for their support.

Declarations

I herewith declare that this thesis contains my own work conducted under the supervision of Professor Shengcai Li and Dr. Duncan Billson. No part of the work in this thesis was previously submitted for a degree at another university.

List of Publications

* indicates the correspondence author

1. **Zhang, Yuning*** and Shengcai Li. "Acoustical scattering cross section of gas bubbles under dual-frequency acoustic excitation." Ultrason. Sonochem. (2015), in press.
2. **Zhang, Yuning***, Duncan Billson and Shengcai Li. "Influences of pressure amplitudes and frequencies of dual-frequency acoustic excitation on the mass transfer across interfaces of gas bubbles." Int. Communications in Heat and Mass Transfer (2015), in press.
3. **Zhang, Yuning** and Shengcai Li*. "Thermal effects on nonlinear radial oscillations of gas bubbles in liquids under acoustic excitation." Int. Communications in Heat and Mass Transfer 53 (2014): 43-49.
4. **Zhang, Yuning***, Yuning Zhang and Shengcai Li. “Bubble dynamics under acoustic excitation with multiple frequencies.” Int. Symp. Cavitation and Multiphase Flow, Oct, 18th-21th, Tsinghua University, Beijing, China.
5. Zhang, Yuning*, **Yuning Zhang**, Xiaoze Du, and Haizhen Xian. "Enhancement of heat and mass transfer by cavitation." Int. Symp. Cavitation and Multiphase Flow, Oct, 18th-21th, Tsinghua University, Beijing, China.

Nomenclature

Roman letters (alphabetical order)

A	amplitude of the incident wave
B/r	amplitude of the divergent spherical scattered wave
c_l	speed of sound in the liquid (m/s)
e_{12}	unit vector pointing from bubble one to bubble two
f_s	frequency of external single-frequency sound field (Hz)
f_1	frequency of external sound field of frequency ω_1 (Hz)
f_2	frequency of external sound field of frequency ω_2 (Hz)
f_B	the secondary Bjerknes force coefficient
F_B	the secondary Bjerknes force (N)
L	separation distance between the centres of two bubbles (m)
N	ratio of the pressure amplitudes of the two component acoustic waves under dual-frequency excitation
P_0	ambient pressure (Pa)
P_s	acoustic pressure amplitude of single-frequency excitation (Pa)
P_{A1}	pressure amplitude of one of the component acoustic wave of the dual-frequency excitation (Pa)
P_{A2}	pressure amplitude of the other of the component acoustic

	wave of the dual-frequency excitation (Pa)
P_e	total input power (Pa)
P_{rad}	radiation pressure (Pa)
P_{rad1}	radiation pressure generated by the oscillations of bubble two at the centre of bubble one (Pa)
P_{rad2}	radiation pressure generated by the oscillations of bubble two at the centre of bubble one (Pa)
∇p_1	pressure gradient generated by bubble one at the centre of bubble two
∇p_2	pressure gradient generated by bubble two at the centre of bubble one
r	radial coordinate from the origin of the centre of the bubble (m)
R	instantaneous bubble radius (m)
R_1	instantaneous radius of bubble one (m)
R_2	instantaneous radius of bubble two (m)
$\dot{R}$	first derivative of the instantaneous bubble radius (m/s)
$\ddot{R}$	second derivative of the instantaneous bubble radius (m/s^2)
R_0	equilibrium bubble radius (m)
R_{01}	equilibrium bubble radius of bubble one (m)
R_{02}	equilibrium bubble radius of bubble two (m)

$R_{\max}$	maximum radius of the bubble during steady-state oscillations (m)
R_{rs}	corresponding resonance bubble radius of the driving frequency of the single-frequency excitation (m)
R_{r1}	corresponding resonance bubble radius of one component driving frequency of the dual-frequency excitation (m)
R_{r2}	corresponding resonance bubble radius of the other component driving frequency of the dual-frequency excitation (m)
t	time (s)
T	period of bubble oscillation (s)
v_1	instantaneous volume of the bubble one (m^3)
v_2	instantaneous volume of the bubble two (m^3)
X	non-dimensional instantaneous bubble radius
X_{max}	non-dimensional maximum bubble radius during steady-state oscillations

Greek Letters (alphabetical order)

β_{ac}	acoustic damping constant
β_{th}	thermal damping constant
β_{tot}	total damping constant
β_{vis}	viscous damping constant
ε_s	non-dimensional amplitude of single-frequency driving sound field
ε_1	non-dimensional amplitude of external sound field of frequency ω_1
ε_2	non-dimensional amplitude of external sound field of frequency ω_2
κ	polytropic exponent
λ_l	wavelength in the liquid (m)
μ_l	viscosity of the liquid (Pa s)
μ_{th}	effective thermal viscosity (Pa s)
ρ_l	density of the liquid (kg/m^3)
σ	surface tension coefficient (N/m)
σ_s	acoustical scattering cross section (m^2)
φ_s	phase of the acoustic wave of the single-frequency excitation
φ_1	phase of one of the component acoustic wave of the

dual-frequency excitation

φ_2 phase of the other the component acoustic wave of the dual-frequency excitation

ω angular frequency of the driving sound field

ω_0 natural frequency of bubble oscillator

ω_s angular frequency of the driving sound field of single-frequency

ω_1 one angular frequency of the driving sound field of dual-frequency

ω_2 another angular frequency of the driving sound field of dual-frequency

Abstract

Acoustic cavitation plays an important role in a broad range of biomedical, chemical and engineering applications, because of its magnificent mechanical and chemical effects. Particularly, the irradiation of the multi-frequency acoustic wave could be favouritely employed to promote these effects, such as enhancing the intensity of sonoluminescence, increasing the efficiency of sonochemical reaction, and improving the accuracy of ultrasound imaging and tissue ablation. Therefore, a thorough understanding of the bubble dynamics under the multi-frequency acoustic irradiation is essential for promoting these effects in the practical applications. The objective of this PhD programme is to investigate the bubble dynamics under dual-frequency excitation systematically with respect to bubble oscillations, the acoustical scattering cross section and the secondary Bjerknes force (a mutual interaction force between two oscillating bubbles). Spherical gas bubbles in water are considered. Both analytical analysis based on perturbation method and numerical simulations have been performed in this thesis.

The analytical solutions of the acoustical scattering cross section and the secondary Bjerknes force under dual-frequency excitation have been

obtained and validated. The value of the secondary Bjerknes force can be considered as the linear combination of the forces derived under the single-frequency approaches. The predictions of those analytical solutions will be impaired for the cases with large acoustic pressure amplitudes.

The numerical simulations reveal some unique features of the bubble dynamics under dual-frequency excitation, e.g., the combination resonances (i.e., their corresponding frequencies corresponding to the linear combinations of the two component frequencies) and the simultaneous resonances (i.e., the simultaneous occurrence of two resonances in certain conditions). The influence of a number of paramount parameters (e.g., the pressure amplitude, the equilibrium bubble radii, the power allocation between the component waves, the phase difference and the driving frequency) on the bubble dynamics under dual-frequency excitation is also investigated with demonstrating examples. Based on that, the parameters for optimizing the dual-frequency approach are proposed. In addition, the effects of thermal effects and mass transfer on the bubble dynamics have also been discussed.

Keywords: cavitation, bubble dynamics, dual-frequency excitation, acoustical scattering cross section, Bjerknes force

Chapter 1 Introduction

1.1 Research background

When stimulated by acoustic waves, bubbles in a liquid will oscillate, termed as “acoustic cavitation” (Plesset and Prosperetti, 1977; Brennen, 1995). Acoustic cavitation has attracted much attention for many years because of its unique physical complexity (Lauterborn and Kurz, 2010), chemical applications (Ashokkumar, 2011) and biomedical significance (Coussios and Roy, 2008). In particular, a considerable body of work has been produced with multiple-frequency acoustic wave irradiation, i.e., two or more acoustic waves with the same or different frequencies acting on the cavitation bubbles simultaneously (as shown in Figure 1.1).

Researchers have found that the use of the multi-frequency ultrasound field could lower the cavitation thresholds (Ciuti et al., 2000), generate more new cavitation nuclei (Dezhkunov, 2003), increase the active cavitational volume (Servant et al., 2003) and improve energy efficiency (Sivakumar et al., 2002). So multi-frequency approaches have been employed to enhance the intensity of sonoluminescence (Hargreaves and

Matula, 2000; Holzfuss et al., 1998; Kanthale et al., 2008; Krefting et al., 2002), to increase the efficiency of sonochemical reactions (Kanthale et al., 2007; Moholkar, 2009; Brotchie et al., 2007; Feng et al., 2002; Tatake and Pandit, 2002), to improve the accuracy of ultrasound imaging (Zheng et al., 2005; Barati et al., 2007; Wyczalkowski and Szeri, 2003) and tissue ablation (Guo et al., 2013). The efficiency of a wide range of engineering applications could be significantly promoted by the multiple frequency ultrasound systems.

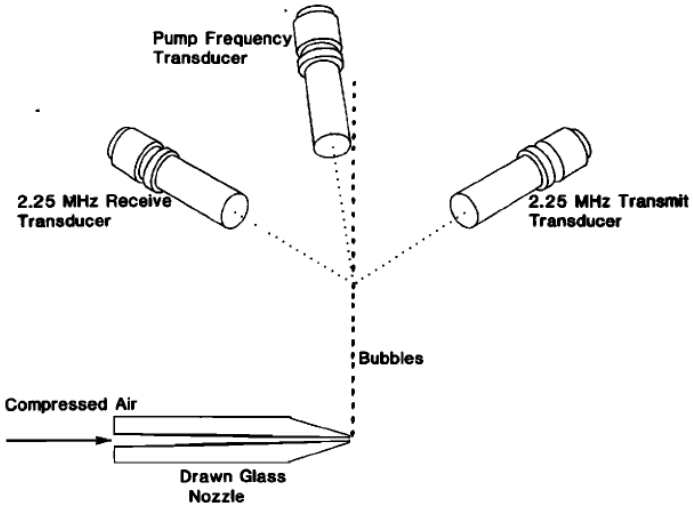

Figure 1.1 A brief demonstration of bubbles under multi-frequency acoustic excitation. This figure was adapted from Fig. 3 of Newhouse and Shankar (1984).

1.1.1 Sonoluminescence under multi-frequency excitation

Marinesco and Trillat (1933) found a photographic plate exposed in an

ultrasound field, which illustrated the phenomenon of multi-bubble sonoluminescence (MBSL). Single-bubble sonoluminescence (SBSL) was firstly fulfiled by Gaitan et al. (1992). The light emitted by the bubble could even be seen by naked eyes. This emission has been attributed to the focus of high energy released during bubble collapse (Brenner et al., 2002). For resent reviews of sonoluminescence, readers are referred to Suslick and Flannigan (2008), Putterman and Weninger (2000). Many papers have reported that the use of multi-frequency acoustical excitation is an efficient way to boost sonoluminescence.

Holzfuss et al. (1998) employed acoustic waves with a combination of the fundamental frequency and its first harmonic with a wide range of amplitudes and relative phases to increase the light emission during bubble oscillations. They reported that the addition of the acoustic wave with the frequency corresponding to the first harmonic can increase the emission of sonoluminescence up to 300%, compared with that emitted by the system with the fundamental frequency alone. It was also found that the relative phase between the two acoustic components plays an important role on the intensity of sonoluminescence. The position of the sonoluminescence bubble was also numerically predicted based on the calculation of the Bjerknes force and the stability criterion, which showed a good agreement

with experimental data.

Krefting et al. (2002) investigated the influential parameters on the SBSL under dual-frequency excitation more systematically. They also added the first harmonic component sound wave into a sinusoidally driven system. Through experimental measurements and numerical simulations, the region of light emission was mapped into the parameter space spanned by the two driving pressure amplitudes and their relative phase. Their results showed that the addition of the second sound wave is able to amplify SBSL in particular parameter zones.

Ciuti et al. (2000; 2003) studied the influential factors of the enhancement of MBSL in acoustic fields with highly different frequencies. In most of the cases, the addition of a low-frequency acoustic wave into the high-frequency field lead to stronger light emission, except the case in which the intensities of both component waves were much higher than the corresponding cavitation thresholds. For resent researches of sonoluminescence under multi-frequency excitation, readers are referred to Hargreaves and Matula (2000), Kanthale et al. (2008), Brotchie et al. (2008), Dezhkunov (2003), and Brotchie et al. (2007).

1.1.2 Sonochemistry

The high temperature and pressure created by the bubble collapse can also promote chemical activities within or near the bubbles, a process termed as “sonochemistry” (Storey and Szeri, 2000). During such processes, the formation of free radicals (e.g., $^{\bullet}OH$, $H^{\bullet}$) could induce new reactions or accelerate existing chemical reactions, such as redox process, degradation of macromolecules and decomposition of organic liquids (Henglein, 1987). The applications of sonochemistry were reviewed recently in a number of works (Adewuyi, 2001; Einhorn et al., 1989; Mason, 1999; Nikitenko et al., 2010).

Like sonoluminescence, the efficiency of sonochemical reactions could be enhanced by multi-frequency ultrasound approaches. Feng et al. (2002) employed both continuous and pulsed dual-frequency systems by combining two ultrasonic transducers: one with frequency of the kilohertz order and the other one with frequency of the megahertz order. A three-frequency system was also involved. They detected the release of iodine, the change of electroconductivity, and the fluorescence formation under different acoustical excitation conditions. The experiments illustrated that a combination of the two sound sources can enhance the yield of chemical products and the addition of the third sound wave could

further increase the efficiency of sonochemistry. Furthermore, they studied the influence of the frequency in the low megahertz range. The lower the frequency was used, the higher cavitation yield was obtained.

The optimization of the cavitation effects in chemical reactors is also an issue concerned in the applications of sonochemistry. Moholkar et al. (2000 and 2009) revealed that the mode and spatial distribution of the cavitation in the reactor could be controlled by adjusting the parameters of the dual-frequency field. For instance, the phase difference between the two ultrasound waves has greater influence on the production of radicals than the frequency ratio does. They demonstrated that it was possible to overcome the directional sensitivity of the cavitation events and the erosion of the sonicator surface by adding extra ultrasound waves. Kanthale et al. (2007) investigated the effects of the intensity and the frequencies of dual-frequency system numerically and compared the results with experimental data in the literature. Their work indicated that there exists an optimum value of the ultrasound intensity in sonochemical processes. And it is more efficient to use lower operating frequencies.

In the last decade, the application of multi-frequency systems in the field of sonochemistry has been studied widely by researchers, such as Tatake

and Pandit (2002), Servant et al. (2003), Sivakumar et al. (2002), Yasuda et al. (2007), and Brotchie et al. (2009).

1.1.3 Biomedical applications

Acoustic cavitation has been applied widely in the field of biomedical engineering. It can enhance the accuracy of ultrasound imaging with the help of the micro-bubbles (Wu et al., 2003; Barati et al., 2007), promote drug and gene transfer into tissue and cells (Song et al., 2007; Hernot and Klibanov, 2008; Newman and Bettinger, 2007), and treat tumours and ablate tissues (Xu et al., 2004; Maxwell et al., 2011). Multi-frequency approach can advance these biomedical applications.

He et al. (2006) developed a high intensity focused ultrasound (HIFU) device which could work both in a single-frequency mode and in a dual-frequency mode. The experimental results showed that the dual-frequency HIFU induced larger tissue lesion than under single-frequency mode within the same time duration, which means that dual-frequency could improve the efficiency of tumour ablation. Meanwhile, this improvement also suggests that the main mechanism of HIFU lesion is cavitation.

Guo et al. (2013) placed tissues at the focus of HIFU transducers under single-frequency, dual-frequency and tri-frequency modes respectively. The multi-frequency mode could yield higher temperatures and a higher growth rate of the temperature during tissue ablation. Their numerical simulation agreed well with the experimental results.

1.2 Physical mechanisms

The underlying mechanisms of the effects of multi-frequency acoustical excitation are still not clear. This section introduces some of the possible candidates briefly.

1.2.1 Dissociation Hypothesis

Ketterling and Apfel (2000) explained the multi-frequency sonoluminescence using phase space diagrams based on the dissociation hypothesis (DH) initially proposed by Lohse and Hilgenfeldt (1997). Because of the high temperature produced during SBSL, the nitrogen and oxygen in air bubbles may dissociate to $^{\bullet}O$ and $^{\bullet}N$ which will compose water soluble chemicals (e.g., NO_3^- and NH_4^+) in subsequent reactions (Lohse and Hilgenfeldt, 1997; Lohse et al., 1997). Meanwhile, the inert gas can accumulate in bubbles under strongly driven acoustic

waves (Lohse et al., 1997; Hilgenfeldt et al., 1996). Therefore, the mass transfer through chemical reaction and rectified diffusion should be considered in SBSL. And the multi-frequency approach could enhance these effects.

Ketterling and Apfel (2000) constructed a phase diagram based on calculations of the equations of bubble motion, diffusive equilibrium and the Mach criterion (assuming that the ratio of the bubble wall velocity and the speed of the gas is larger than one), which separates the response of the bubbles into four regions i.e. stable SL, unstable SL, stable non-SL and unstable non-SL. Comparing their results with the experimental data of Holzfuss et al. (1998), an excellent quantitative agreement is found.

1.2.2 Nucleation

For multiple bubble cavitation, Cuiti et al. (2000 and 2003) proposed that when the liquids are irradiated by the ultrasound field consisting of two highly different frequencies, a large amount of the new nuclei could be generated by the added low-frequency (LF) acoustic wave, leading to the enhancement of sonoluminescence.

According to Figure 1.2, at the moment of switching the LF field off, the

sonoluminescence intensity did not fall down immediately. On the contrary, it increased and then decreased smoothly. This phenomenon suggests that the bubble fragments induced by bubble collapse became new nuclei with smaller radii than the initial equilibrium radius, which were likely to collapse in the high-frequency (HF) field. This mechanism could explain the enhancement of sonoluminescence in the cases of switching-on the LF and HF fields successively with a certain time interval (as shown in Figure 1.3). The new nuclei generated by the LF field could live for at least several seconds so that their oscillation and collapse could strengthen the intensity of sonoluminescence in the HF field.

Feng et al. (2002) investigated the cavitation yield from the aspect of sonochemistry. They also pointed out that the production of new bubbles by the LF field is one of possible mechanisms for the enhancement of cavitation effects.

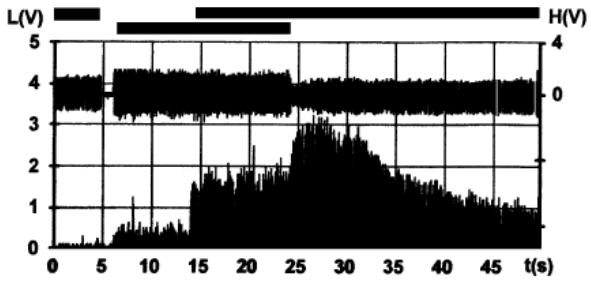

Figure 1.2 Time history of the hydrophone output (upper record) and of the photomultiplier (lower record). The black bars above the image indicate switching-on of the LF field (lower bar) and the HF field (the higher bar). High-frequency (HF) field parameters: pulse period 100 ms; pulse duration 2 ms. This figure was adapted from Fig. 3 of Cuiti et al. (2003).

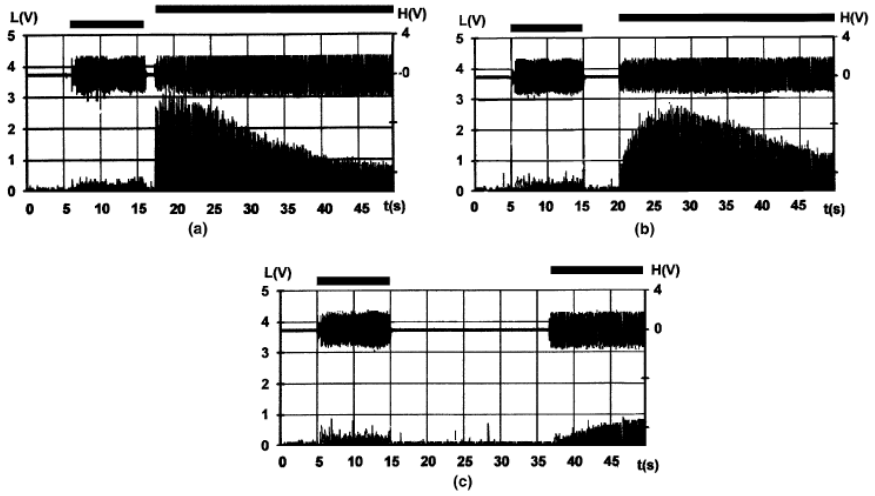

Figure 1.3 Time history of the hydrophone output (upper record) and of the photomultiplier (lower record) for different time intervals Δt between the LF field off and the HF field on: $\Delta t \approx 2s$ (a), 5s (b), 22.5s (c). Other parameters are the same as in Figure 1.2. This figure was adapted from Fig. 3 of Cuiti et al. (2003).

1.2.3 Other mechanisms

1. Periodic decrease in the total quasi-static pressure in the LF field.

The LF field is quasi-static in relation to the HF field when the frequency of the LF field is lower (ten times or more) than that of the HF field. The total pressure (the sum of the hydrostatic pressure and the pressure of the LF field) decreases during the negative pressure amplitude half-period of the LF field, leading to the increase of bubble size and bubble quantity. As a result, in the compression half-period, the increase of the LF-field quasi-static pressure may increase the efficiency of the bubble collapse in the HF-field (Carpendo et al., 1987; Wolfrum et al., 2001; Iernettia et al., 1997).

2. Suppression of the formation of stable bubble clusters.

The bubbles in clusters are close to each other so that they interact strongly with shock waves and the Bjerknes forces (Leighton, 1994). Therefore, bubbles deform under these interactions in the early stage of collapse. The non-spherical collapse is less efficient from the aspect of the energy concentration, which is considered to be one of the reasons decreasing the intensity of MBSL by bubble cluster (Evans, 1996). The addition of the LF acoustic wave can induce large bubbles. The shock waves and liquid microjets produced by the collapse of these large bubbles

could prevent the formation of bubble cluster. Hence, the overall efficiency of the energy concentrated by cavitation bubbles may raise.

3. Optimization of sonochemical reactor.

The modelling and experimental investigation of Tatake and Pandit (2002) revealed that the introduction of the second sound wave results in better distribution of the cavitational activity in the reactor, because the dual-frequency approach uniforms the yields of cavitation, minimises the formation of standing waves and leads to an effective utilization of the reactant volume.

1.3 Bubble dynamics under acoustic excitation

In the above sections, one can find that bubble dynamics play an essential role in the aforementioned cavitation effects and related applications. In this section, the basic features of bubble oscillations are introduced and research in the fields of acoustical scattering cross section, the Bjerknes force and chaos is reviewed.

1.3.1 Oscillations of bubbles

To solve the radial oscillations of gas bubbles in liquids, various models

have been developed and reviewed by Plesset and Prosperetti (1977), Prosperetti (1984a; 1984b), Feng and Leal (1997), Brenner et al. (2002) and Lauterborn and Kurz (2010).

Lauterborn (1976) gave a thorough investigation of the basic properties of nonlinear oscillations of gas bubbles in liquids numerically. The response of a bubble to a single-frequency excitation was calculated and displayed in the form of frequency response curves, i.e., the maximum bubble radius in steady-state oscillation (non-dimensionalized by the equilibrium bubble radius) versus driving frequency. Figure 1.4 shows typical response curves with special features of nonlinear oscillations. The expression n/m (here, m and n are two integers) above the peaks represents the order of the resonance. Cases with m=1 and n=2, 3… correspond to harmonics; cases with m=2, 3… and n=1 correspond to subharmonics; cases with m=2, 3… and n=2, 3… correspond to ultraharmonics. There exist thresholds for subharmonics and ultraharmonics. Figure 1.5 illustrates the threshold for the subharmonic of the order $1/2$ varying with bubble radii. For detailed definition and the descriptions of the resonances and nonlinear phenomena (e.g., jump phenomenon, hysteresis) mentioned above, readers are referred to Lauterborn (1976).

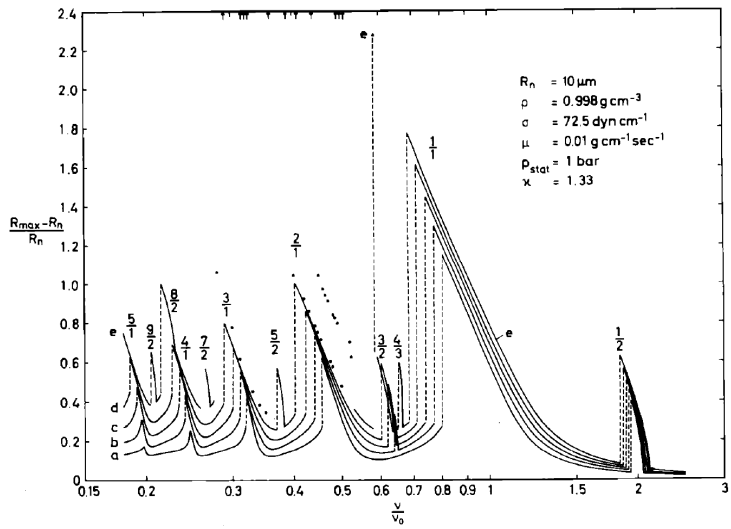

Figure 1.4 Frequency response curves for a bubble in water with a radius at rest of $R_n = 10$ μm for different sound pressure amplitudes P_A of (a) 0.4, (b) 0.5, (c) 0.6, (d) 0.7, and (e) 0.8 bar. ν is the frequency of the driving sound field. ν_0 is the natural frequency of the bubble oscillation. $R_{\max}$ is the maximum radius of the bubble during its steady-state oscillation. The numbers marked above the peaks are the orders of the resonances, represented as n/m. The dots and the arrows belong to curve (e). The arrows indicate that the corresponding stationary solution is out of the range of the diagram or that no stationary solution could be found. In this case the values of the amplitudes were also very high oscillating around some value outside the diagram. This figure was adapted from Fig. 3 of Lauterborn (1976).

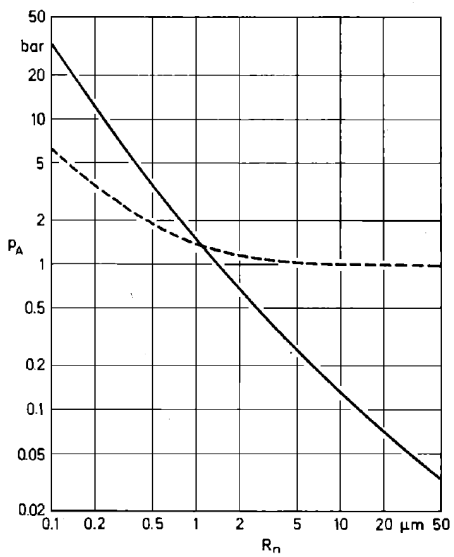

Figure 1.5 Threshold for the occurrence of the first subharmonic oscillation (of order $1/2$ at $\nu/\nu_0 = 2$) versus the equilibrium bubble radius (solid line). ν is the frequency of the driving sound field. ν_0 is the natural frequency of the bubble oscillation. P_A is the amplitude of sound pressure. This figure was adapted from Fig. 13 of Lauterborn (1976).

The power spectrum can be used to describe the property of bubble oscillators. By solving the bubble motion equations, the variations of bubble radius with time could be obtained (as shown in Figure 1.6). Then through the Fourier transform, the "time domain" diagram could be transformed to the "frequency domain" diagram, i.e., the power spectrum [as shown in Figure 1.7(a)], the corresponding frequencies of the bands are the driving frequency ν and its integer multiples, i.e., the main

resonance and its harmonics. In particular conditions, as shown in Figure 1.7(b), there are bands at $\nu/2$, $3\nu/2$ and $5\nu/2$ which represent subharmonic and ultraharmonics respectively. These lines are also typical bands which usually appear in the scattered signals (i.e., acoustical echo of bubble oscillations) in experiments.

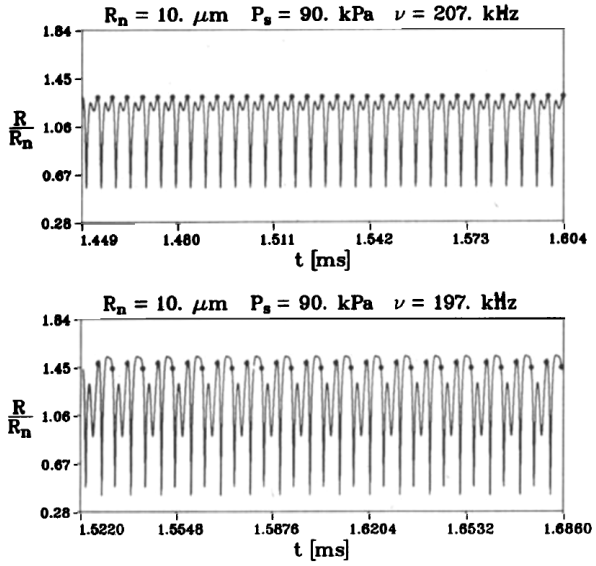

Figure 1.6 Non-dimensionized bubble radius versus time. Equilibrium bubble radius R_n is 10 μm. Sound pressure amplitude is 90 kPa. Driving frequency ν is 207 kHz for upper diagram and 197 kHz for lower diagram. This figure was adapted from Fig. 13 of Lauterborn (1988).

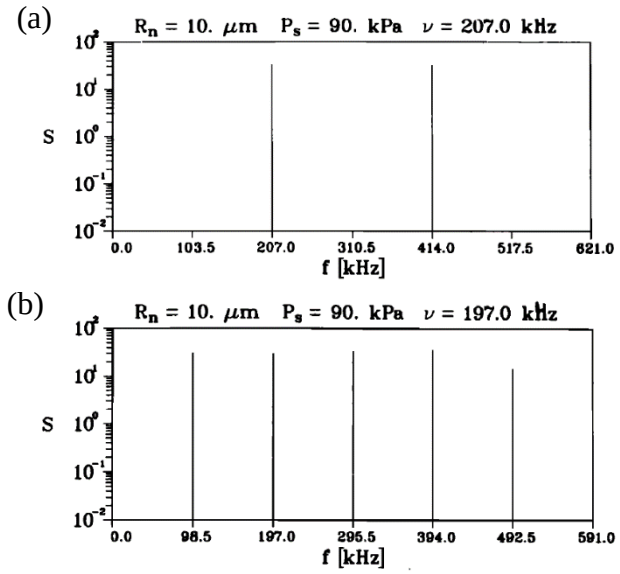

Figure 1.7 Power spectrum of bubble oscillator. Equilibrium bubble radius R_n is 10 μm. Sound pressure amplitude is 90 kPa. Driving frequency *v*: (a) 207 kHz; (b) 197 kHz. This figure was adapted from Fig. 13 of Lauterborn and Parlitz (1988).

Newhouse and Shankar (1984) pointed out that the echo of bubble oscillators under a dual-frequency acoustical excitation with frequencies f_1 and f_2 would contain the bands at $f_1 \pm f_2$ besides the typical bands in single-frequency approach. They further gave the analytical solutions of the radiated pressure at frequencies f_1, f_2, $2f_1$, $2f_2$, $f_1 + f_2$, and $f_1 - f_2$. They (Newhouse and Shankar, 1984; Shankar et al., 1986) also proved that the resonance at $f_1 + f_2$ is much sharper than the resonance at f_2, which means more accurate measurements of bubble size can be obtained through dual-frequency approach.

However, in multi-frequency systems, the scattered echo contains more bands rather than those corresponding to the difference and sum of the driving frequencies. Figure 1.8 is an experimental spectrum of the scattered signal of bubbles excited by a dual-frequency field (with frequencies f_1 and f_2 respectively). In this figure, there are peaks corresponding to main resonances (marked by ■), their harmonics (marked by □), subharmarnics (marked by ▲） and sum and difference (marked by △). But besides these, there are other peaks (marked by ◆), the magnitudes of which are of the same order of the harmonics.

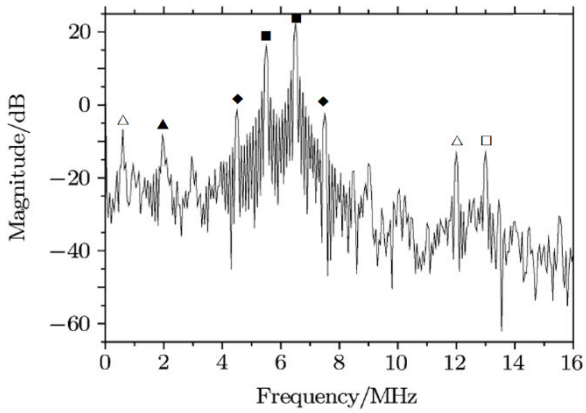

Figure 1.8 Experimental spectrum of the scattered signal from bubbles excited by a dual-frequency ultrasound field. The frequencies of the two sound waves are $f_1 = 5.5$ MHz and $f_2 = 6.5$ MHz, respectively. $f_1 + f_2 = 12$ MHz. $f_2 - f_1 = 1$ MHz. This figure was adapted from Fig. 3 of Ma (2010).

So far as we know, most published papers mainly focused on the application of the sum and difference of the driving frequencies in multi-frequency systems (Wyczalkowski and Szeri, 2003; Phelps and Leighton, 1994; Wu et al., 2005). The fundamental properties of bubble dynamics (for instance, the special bands marked by ◆ shown in Figure 1.8) under multi-frequency acoustical excitation have not been studied systematically. However, these features are essential for understanding the bubble behaviour under multi-frequency excitation as well as expanding their applications.

1.3.2 Acoustical scattering cross section

During the oscillations of bubbles, a diverging spherical wave can be emitted and radiation pressure can be generated within the liquid surrounding the bubbles. The acoustical scattering cross section, defined as the square of the ratio between the amplitude of the radiated wave by bubbles and the amplitude of the incident acoustic wave (Medwin, 1977), is usually employed as a criterion of the scattering ability of the bubbles. This scattering force of cavitation bubbles is essential for facilitating the reaction of chemical processes (Shah et al., 1999; Gogate et al., 2001; Vichare et al., 2000; Yoo and Han, 1982), measuring bubble size distributions (Newhouse and Shankar, 1984; Sutin et al, 1998; Czerski,

2012), de-agglomerating particle clusters (Wagterveld et al., 2011; Sauter et al., 2008; Marković et al., 2008), refining grain structures of metals (Eskin and Eskin, 2003; Eskin, 1994; Komarov et al., 2013), explaining unusual bubbles in stranding marine mammals caused by anthropogenic sounds (e.g., sonar) (Jepson et al., 2003; Cox et al., 2006; Crum et al., 2005), and performing non-invasive therapy and drug delivery (Coussios et al., 2008; ter Haar and Daniels, 1981; Dollet et al., 2008).

The acoustical scattering cross section of gas bubbles has been studied by many researchers over several decades. The most widely cited formula for acoustical scattering cross section of gas bubbles was mainly developed by Wildt (1946) and Medwin (1977). A near-resonance correction based on the Wildt-Medwin formula was initially proposed by Weston (1967) and recently generalized by Zhang (2013a). d'Agostino and Brennen (1988) studied the acoustical absorption and scattering cross sections of spherical bubble clouds. Leroy et al. (2009) studied the scattering behaviour of a monodisperse layer of bubbles. Hilgenfeldt et al. (1998) proposed a unified theory for the scattering phenomenon of bubbles for diagnostic ultrasound. Clarke and Leighton (2000) investigated the effects of the transient state on the scattering cross section of bubbles. However, in the literature, the acoustical cross section of bubble under dual-frequency

excitation has not yet been studied.

1.3.3 Bjerknes forces

When gas bubbles are driven by a sound field in a liquid, the radiation force induced by the acoustic pressure gradient could cause mutual interaction between bubbles, this phenomenon was firstly reported by Bjerknes (Bjerknes, 1906). The force due to the direct effect of the sound field is named as “primary Bjerknes force”. The force generated by other oscillating bubbles which causes the mutual attraction or repulsion between bubbles is named as “secondary Bjerknes force” (Crum, 1975; Leighton, 1994).

The Bjerknes forces are widely present in bubble systems. In a chemical reactor, such as a bubble column, the acoustic waves can enhance the mass transfer rate and the liquid-phase turbulence significantly through the Bjerknes forces (Fan and Cui, 2005; Ellenbergur et al., 2005; Waghmare et al., 2007). The Bjerknes forces will also affect the intensity and the active volume of cavitation of the chemical reactor (Kanthale et al., 2003). In medical practices, the Bjerknes forces can be employed to manipulate micro bubbles filled with drugs (Shortencarier et al., 2004; Rychak et al., 2005; Yoshida et al., 2011).

As a basic phenomenon of acoustic cavitation, the mutual interaction between bubbles induced by the secondary Bjerknes force has been investigated theoretically and experimentally by many researchers. According to the linear theory (Bjerknes, 1906; Mettin et al., 1997; Doinikov, 1999), the direction of the secondary Bjerknes force between two bubbles depends on the relationships between the frequency of the driving acoustic wave and the linear resonance frequencies of the two bubbles. If the driving frequency lies between the linear resonance frequencies of the two bubbles, the interaction force between the two bubbles is repulsive. Otherwise, they will attract each other. However, this theory is based on the assumptions of the small pressure amplitude of the acoustic field and the large distance between bubbles. There are many experimental results which could not explained by this theory. For instance, the bubbles in a strong sound field will accumulate and form ribbon-like structures termed as “streamers” (Akhatov et al., 1994; Lauterborn and Ohl, 1997; Mettin et al., 1999). The direction of the secondary Bjerknes force reverses at a specific distance (Yoshida et al., 2011). And periodic motion pattern appears when the bubbles of equal sizes are forced near their resonance frequency (Barbat et al., 1999).

In the past decades, many efforts have been made on the development of the theory propose by Bjerknes (1906). The nonlinearity of the bubble oscillators is one of the primary factors leading to sign reversals of the Bjerknes force. Oguz and Prosperetti (1990) reported that the repulsion also exists in the case of the driving frequency below the linear resonance frequencies of the two bubbles, even there is slightly nonlinear oscillation when the driving pressure amplitude is below 0.5 bar. Mettin et al. (1997) found the same phenomenon in the cases of the oscillating bubbles with strong collapse under the acoustic field with a high pressure amplitude. Doinikov (1999) and Pelekasis et al. (2004) investigated the effects of the harmonics of bubble oscillations on the secondary Bjerknes force. The secondary Bjerknes force is also related to the distance between the bubbles. The sign of the secondary Bjerknes force changes during the bubbles getting close to each other (Harkin et al., 2001; Doinikov and Zavtrak, 1995; Ida, 2003). The viscosity (Doinikov, 2002) and the compressibility (Doinikov and Zavtrak, 1997) of the liquid also influence the mutual interactions between bubbles. For other recent studies of the secondary Bjerknes force, readers are referred to Doinikov et al. (2005), Pelekasis and Tsamopoulos (1993a and 1993b) and Ida (2005 and 2009).

However, as far as the author is aware, no researcher has systematically

studied the secondary Bjerknes force under the multi-frequency excitation, which is an important topic for the further application of multi-frequency approaches.

1.3.4 Bifurcation and Chaotic oscillations

For a bubble oscillator forced by a sound wave with period *T*, the period of its radial oscillation should be equal to *T* according to the linear theory. If the pressure amplitude is higher than the threshold, the subharmonic oscillation appears where the corresponding driven frequency is $2\nu_0$ (ν_0 is the natural frequency of bubble oscillations), as shown in Figure 1.4. Meanwhile, the period of bubble oscillation becomes *2T*. This change of the oscillation state is called "**period-doubling**" (Lauterborn and Parlitz, 1988). Not only the change of pressure amplitude but also the variation of driven frequency could induce period-doubling, as shown in Figure 1.7.

Figure 1.9 demonstrates period-doubling by adjusting one particular parameter of the oscillating system. The trajectory shown at the beginning is a typical phase space diagram (see "Jordan and Smith, 2007" for the details of the phase diagram) of a bubble oscillating with the period of the driving sound wave, named as "limit cycle". When the parameter of the system, μ, becomes μ_1, the period doubles to *2T*. If the parameter further

changes to μ_2, the period reaches *4T*. Then after infinitely successive doubling, there is no certain period for bubble oscillating and it turns into **chaotic oscillation**. The changing parameter is called the **control parameter**. The changes of the state of the bubble at particular values of the parameter are called **bifurcations**. If the limit sets (named "attractors") of the bubble oscillator are plotted versus the control parameter, a bifurcation diagram can be obtained.

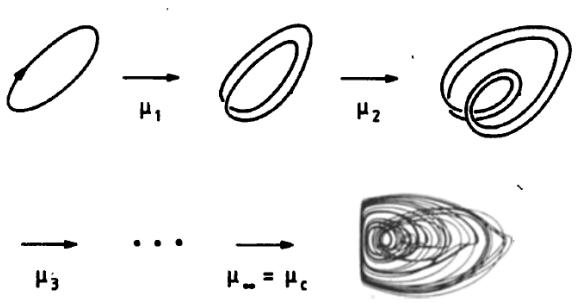

Figure 1.9 Period-doubling route to chaos via an infinite cascade of period-doubling bifurcations. This figure was adapted from Fig. 8 of Lauterborn and Parlitz (1988).

As shown in Figure 1.9, the local bifurcations could lead to a route to chaos. There are three basic routes to chaos, i.e., via Hopf bifurcations, via saddle-node bifurcations and via period-doubling bifurcations respectively (Eckmann, 1981). Parlitz et al. (1990) studied the bifurcation structures and resonances of a gas bubble oscillator driven by an ultrasound wave in water. The frequency bifurcation diagram shown in Figure 1.10 illustrates

how the attractors vary with the driven frequency. The arrows indicate the saddle-node bifurcation points, and the "bubble" like structure near the resonance $R_{1,2}$ (i.e., subharmonic) indicates period-doubling bifurcation points. Figure 1.11 further illustrates the sequences of the period-doubling bifurcation structure of resonance $R_{1,2}$, leading to chaos. All these results reveal the evolution of bifurcation structures along with the frequency and the pressure amplitude of the external excitation.

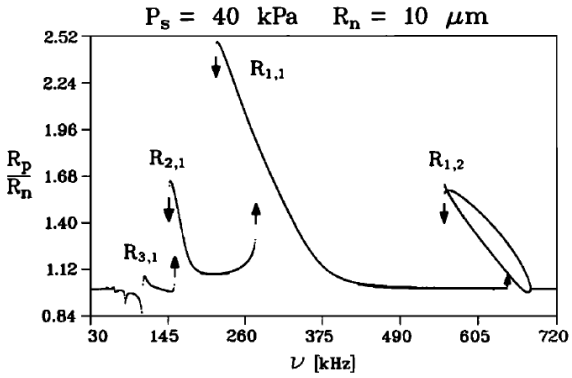

Figure 1.10 Frequency bifurcation diagram for $P_s = 40$ kPa. ν is the frequency of the driving sound field. P_s is the pressure of driving sound. R_n is the equilibrium radius of the bubble. The arrows indicate transitions at saddle-node bifurcation points. This figure was adapted from Fig. 8 of Parlitz et al. (1990).

Behnia et al. (2009a) calculated the sets of bifurcation diagrams of single bubble oscillation under ultrasound waves with several different control parameters, such as sound pressure, driving frequency, bubble radius,

surface tension and viscosity. The results illustrated rich patterns of bifurcation and chaotic phenomenon. Behnia et al. (2009b) proposed that R_0/λ (where R_0 is the initial bubble radius and λ is the wavelength of the sound wave) could be a criterion to classify the patterns of the nonlinear bubble behaviour. For other recent works on chaotic behaviour and bifurcation of bubble oscillations, readers are referred to Lauterborn and Cramer (1981); Lauterborn, et al. (1994, 2008), Simon et al. (2002), Cabeza et al. (1998), and Behnia et al. (2013a, 2013b).

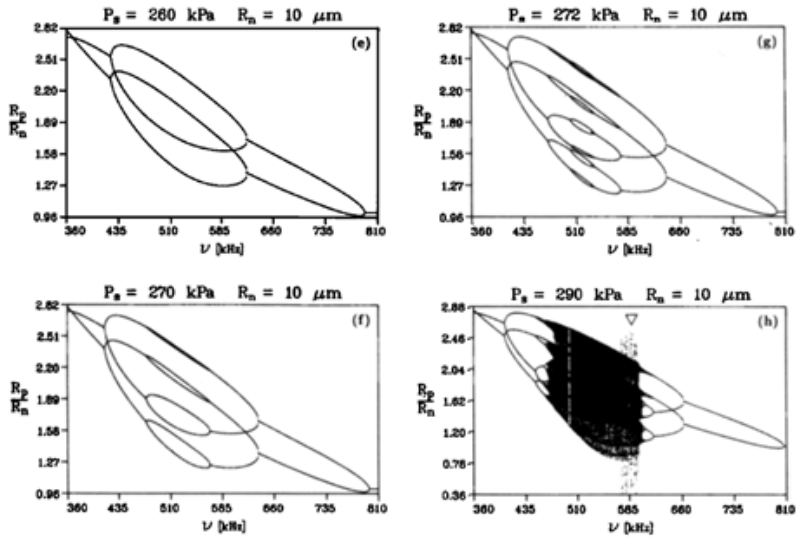

Figure 1.11 Bifurcation diagrams showing the evolution of the resonance $R_{1,2}$ for increasing sound pressure. This figure was adapted from Fig 15 of Parlitz et al. (1990).

In the chaos, a system obeys certain physical laws so that its future behaviour is deterministic, while the system could also exhibit

unpredictable behaviour owing to the sensitivity to initial conditions (Ott, 2002; Giordano and Nakanishi, 2006). Chaos widely exists in dynamical systems. Because of its unpredictability, chaotic oscillation should be avoided in the practices of sonochemistry, ultrasound enhanced drug delivery and surgery. The addition of the second forcing term is one method to control chaos, which has been successively applied in a pendulum system (Braiman and Goldhirsch, 1991), Duffing-Holmes oscillator (Chacón and Bejarano, 1993; Jing and Wang, 2005) and electric circuit (Tamura et al., 1999). Behnia et al. (2009c) found that the addition of the second sound wave, i.e., the usage of the dual-frequency system, could also reduce the chaotic oscillations of the bubbles to the regular ones. They discussed the influence of the frequency of the second wave and the phase difference between two waves. And numerical simulations were performed on the progress of HIFU tumour ablation.

However, the studies of Behnia et al. (2009c) were performed in a very narrow range of parameter zones, i.e., the pressure amplitude was from 1.55 MPa to 1.7 MPa. Actually, multi-frequency excitation may lower the critical pressure amplitude corresponding to the appearance of chaotic oscillation (Szeri and Leal, 1991), which means that the addition of the second sound wave may induce chaos. Therefore, for a deeper

understanding of bubble behaviour under multi-frequency excitation and better applications of multi-frequency systems in the fields mentioned before, a systematic investigation of the chaotic oscillation of bubbles under multi-frequency excitation is necessary.

1.4 Objectives of thesis

In this thesis, the bubble dynamics under dual-frequency excitation have been investigated systematically in respects of the basic properties of bubble oscillations, the acoustical scattering cross section, and the secondary Bjerknes force. The whole thesis is organized as follows:

Chapter 2 focuses on the fundamental properties of bubble oscillations under dual-frequency excitation. By employing the power spectrum and the response curves, the unique features (termed as “combination resonance” and “simultaneous resonance”) of bubble oscillations under dual-frequency excitation are revealed and investigated quantitatively. The influence of several paramount parameters, such as the pressure amplitude, the equilibrium bubble radius, the power allocation between the component waves, the phase difference and the driving frequency, on the bubble dynamics is discussed.

In Chapter 3, both the analytical solutions and the numerical simulations for the acoustical scattering cross section of gas bubbles under dual-frequency excitation are obtained. And the validity of the analytical solution is verified. The nonlinear characteristics (e.g., the combination resonances) as well as the enhancement of the scattering cross section in dual-frequency approach are revealed. Furthermore, the influential parameters (e.g., the pressure amplitude, the energy allocation between two component acoustic waves and the driving frequencies) on scattering cross section are also investigated with demonstrating examples.

In Chapter 4, the analytical solution for the secondary Bjerknes force under dual-frequency excitation is obtained and validated. The values of the secondary Bjerknes force under dual-frequency excitation are investigated numerically in a wide range of equilibrium bubble radii. And the parameter zone is classified into different regions according to the sign of the secondary Bjerknes force. The unique characteristics (i.e., the combination resonances and the complicated patterns of the parameter zone for sign change) of the secondary Bjerknes force under dual-frequency excitation are revealed. Moreover, the influence of pressure amplitude on the secondary Bjerknes force is also revealed.

In Chapter 5, the contributions obtained from this PhD work to the further understanding of the bubble dynamics under dual-frequency excitation are summarized and the possible future works on this subject are proposed.

Chapter 2 Fundamentals of Bubble Dynamics under Dual-Frequency Excitation

In this chapter, the basic properties of gas bubbles oscillating in liquid under dual-frequency acoustical excitation are investigated numerically. The whole chapter is organized as below: in Sec. 2.1, the basic equations related to bubble motion and the numerical methods for solving those equations are briefly introduced; in Sec. 2.2, the fundamentals of bubble oscillations under dual-frequency excitation are studied; in Sec. 2.3, the influential parameters on bubble oscillations (e.g., pressure amplitude, energy allocation and driving frequencies) are discussed. The primary assumptions employed in this chapter (and following chapters) are:

1. The gas and liquids are both Newtonian fluids.
2. The bubble oscillates spherically symmetrically: The bubbles studied in this thesis are smaller than 100 μm under acoustic excitation with low pressure amplitude, so due to surface tension, they will keep spherical. For very strong excitation, the shape stability will be an important issue (Eller and Crum, 1970; Shaw, 2006).
3. Only radial motion of bubble is considered: this thesis focuses on

revealing the new features of the dual-frequency excitation so that the influence of translational motion on the radial oscillation is not taken into consideration to make the analysis simpler. Therefore, the effects of gravity and buoyancy, leading to position moving, are also omitted. For the studies in which the translational motion is coupled with the radial oscillation, readers are referred to Doinikov (2001 and 2004).

4. Vapour pressure is negligible: the saturated vapour pressure in air is only 2300 Pa at 20℃, which is far less than the gas pressure inside bubble [i.e., $P_{in,gas} = P_0 \left(R_0 / R \right)^{3\kappa}$].

2.1 Basic equations and solutions

The equation of bubble motion can be written as (Keller and Miksis, 1980)

$$\left(1-\frac{\dot{R}}{c_l}\right) R\ddot{R} + \frac{3}{2}\left(1-\frac{\dot{R}}{3c_l}\right)\dot{R}^2 = \left(1+\frac{\dot{R}}{c_l}\right)\frac{p_{ext}(R,t)-p_s(t)}{\rho_l} + \frac{R}{\rho_l c_l}\frac{d[p_{ext}(R,t)-p_s(t)]}{dt}, \quad (2.1)$$

where

$$p_{ext}(R,t) = \left(P_0 + \frac{2\sigma}{R_0}\right)\left(R_0 / R\right)^{3\kappa} - \frac{4\left(\mu_l + \mu_{th}\right)}{R}\dot{R} - \frac{2\sigma}{R}, \quad (2.2)$$

with

$$p_s(t) = P_0\left[1+\varepsilon_s \cos(\omega_s t + \varphi_s)\right] \quad (2.3)$$

for single-frequency excitation,

or with

$$p_s(t) = P_0\left[1+\varepsilon_1\cos(\omega_1 t+\varphi_1)+\varepsilon_2\cos(\omega_2 t+\varphi_2)\right] \tag{2.4}$$

for dual-frequency excitation.

Here, R is the instantaneous bubble radius; the overdot denotes the time derivative; c_l is the speed of sound in the liquid; ρ_l is the density of the liquid; t is the time; P_0 is the ambient pressure; σ is the surface tension coefficient; R_0 is the equilibrium bubble radius; κ is the polytropic exponent; μ_l is the viscosity of the liquid; μ_{th} is the effective thermal viscosity; ε_s, ε_1 and ε_2 are the non-dimensional amplitude of the external acoustic excitation; ω_s, ω_1 and ω_2 are the angular frequencies of the external acoustic excitation; φ_s, φ_1 and φ_2 are the phases of the external acoustic waves. The natural frequency of the bubble oscillator is referenced to (Brennen, 1995; Leighton, 1994):

$$\omega_0^2 = \frac{1}{\rho_l R_0^2}\left[3\kappa\left(P_0+\frac{2\sigma}{R_0}\right)-\frac{2\sigma}{R_0}\right]. \tag{2.5}$$

For numerical simulations, Eqs. (2.1)-(2.4) are solved by the fourth order Runge-Kutta Mehtod (Dormand and Prince, 1980) with fixed step size of time (Δt). Then the time domain solution $R(t)$ is transformed to a frequency domain function $Y(f)$ by the Fast Fourier Transform (FFT). Here, the numerical solution of $R(t)$ is a vector composed by discrete

values. The total number of the elements is *J*. Its Fourier transform is

$$Y_k = \sum_{j=0}^{J-1} R\left(j\Delta t\right) e^{2\pi i \cdot jk/J} \tag{2.6}$$

Where Y_k is corresponding to the discrete frequency $f_k = k/\left(J\Delta t\right)$.

The power of the corresponding frequency is given by

$$P\left(f_k\right) = \left|Y\left(f_k\right)\right| \tag{2.7}$$

Thus, the power spectrum of bubble oscillations is obtained by plotting the function $P\left(f_k\right)$. For convenience, the radial oscillations of air bubbles in water are considered. And the effects of damping caused by the heat transfer across bubble interfaces are ignored (i.e., $\mu_{th} = 0$). In this chapter, discussions focus on cases with small and moderate acoustic pressure amplitudes.

The constants employed in numerical method are listed in Appendix A. In the following figures and discussions, non-dimensional values are used, such as ω/ω_0, ε, $X = \left(R - R_0\right)/R_0$ and $X_{\max} = \left(R_{\max} - R_0\right)/R_0$. Here, $R_{\max}$ is the maximum radius of the bubble during steady-state oscillations. The ratio of the pressure amplitudes of the two component acoustic waves is defined as $N = P_{A2}/P_{A1}$, which reflects the power allocation between the high-frequency component and the low-frequency component. For comparison, the total input power, $P_e = \left(P_{A1}^2 + P_{A2}^2\right)^{1/2}$, remains constant during the simulations of the cases with different *N*. In the following

sections, all the discussions are based on the results of numerical solutions.

2.2 Response of bubbles under dual-frequency acoustic excitation

In this section, the basic properties of bubble oscillation under dual-frequency acoustic excitation are investigated. In this section, for simplicity, we assume $\varepsilon_1 = \varepsilon_2$. For more general cases (e.g., two acoustic waves with unequal amplitudes), readers are referred to Sec. 2.3.

2.2.1 Basic structures

To avoid the effects of resonance (e.g., the strong nonlinear property near the natural frequency of the bubble oscillator), the sound frequencies employed in this section are far below the resonant frequency of bubbles. Hence, $\omega_1 = 0.03\omega_0$ and $\omega_2 = 1.9\omega_1 = 0.057\omega_0$. The equilibrium bubble radius R_0 is 10 μm. The non-dimensional pressure amplitude of the sound wave, P_e/P_0, is 0.0707 (i.e., $\varepsilon_1 = \varepsilon_2 = 0.05$).

Figures 2.1 and 2.2 show the variations of the non-dimensional bubble radius X [$X = (R - R_0)/R_0$] versus time under single- and dual-frequency excitation respectively. As shown in Figure 2.1, for single-frequency

acoustic excitation, gas bubbles show steady oscillations with their amplitude and frequency unchanged, while for dual-frequency acoustic excitation (as shown in Figure 2.2), the oscillations of gas bubbles are much more complicated with the significant oscillations of the frequency and amplitude. The corresponding FFT analysis of the variations of the instantaneous bubble radius under single- and dual-frequency acoustic excitation are shown in Figures 2.3 and 2.4. For the case under single-frequency excitation (as shown in Figure 2.3), the power spectrum is quite simple, including a main band corresponding to the driving frequency of the acoustic excitation ($\omega/\omega_0 = 0.03$) and its first ($\omega/\omega_0 = 0.06$) and the second harmonics ($\omega/\omega_0 = 0.09$).

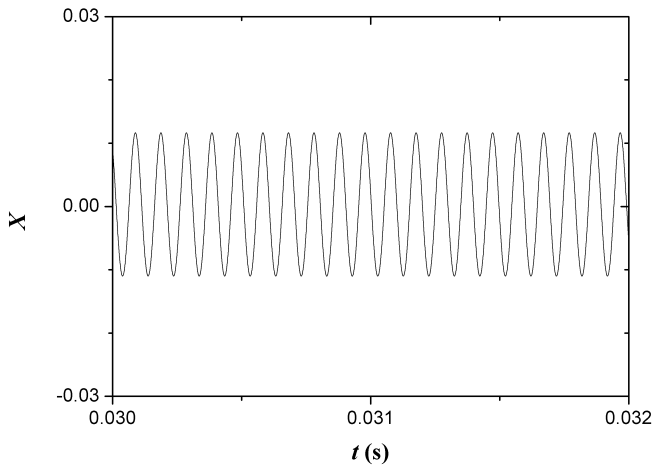

Figure 2.1 Variations of the non-dimensional bubble radius during its oscillation under single-frequency acoustic excitation versus time. $X = (R - R_0)/R_0$. $R_0 = 10$ μm. $\omega_s = 0.03\omega_0$. $\varepsilon = 0.05$.

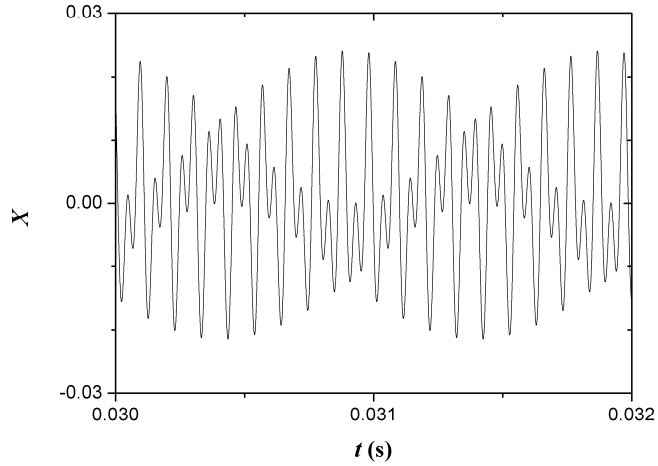

Figure 2.2 Variations of the non-dimensional bubble radius during its oscillation under dual-frequency acoustic excitation versus time. $X=\left(R-R_0\right)/R_0$. $R_0=10$ μm. $\omega_1=0.03\omega_0$. $\omega_2=1.9\omega_1=0.057\omega_0$. $\varepsilon_1=\varepsilon_2=0.05$.

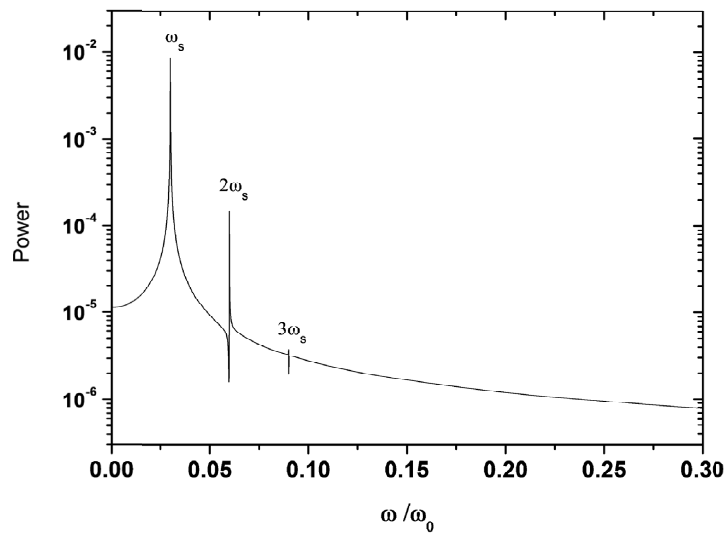

Figure 2.3 Power spectrum of bubble oscillations under single-frequency acoustic excitation. $R_0=10$ μm. $\omega_s=0.03\omega_0$. $\varepsilon=0.05$.

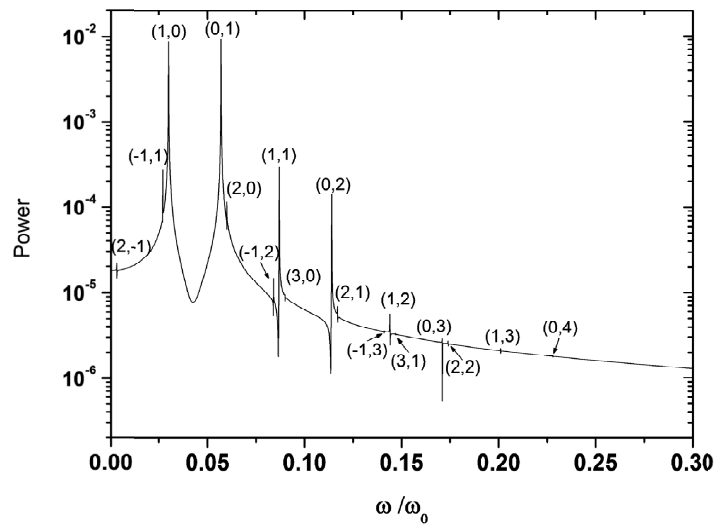

Figure 2.4 Power spectrum of bubble oscillations under dual-frequency acoustic excitation. $R_0 = 10$ μm. $\omega_1 = 0.03\omega_0$. $\omega_2 = 1.9\omega_1 = 0.057\omega_0$. $\varepsilon_1 = \varepsilon_2 = 0.05$. The integers with brackets above the peaks stand for (*n*,*m*), corresponding to the frequency $\omega_p = n\omega_1 + m\omega_2$. Readers are referred to the text for the details.

As shown in Figure 2.4, even for a relatively low pressure amplitude (e.g., $\varepsilon_1 = \varepsilon_2 = 0.05$), the oscillations of gas bubbles under dual-frequency excitation are already very complex. Besides the bands corresponding to the main resonances and the harmonics, the power spectrum illustrates much more bands. Furthermore, the corresponding frequencies of these bands can be expressed by the linear combination of the frequencies of the two component sound waves, i.e., $\omega_p = n\omega_1 + m\omega_2$ (*n* and *m* are two integers). In Figure 2.4, the integers with brackets above the peaks stand

for (n,m).

According to the values of *n* and *m*, the bands in the power spectrum can be classified into the following categories:

a) Bands corresponding to the main resonances, e.g., the bands marked with (1,0) and (0,1).

b) Bands corresponding to the harmonics, e.g., the bands marked with (*n*,0) and (0,*m*), where *n* =1-3 and *m* =1-4.

c) Bands corresponding to the combination resonances, e.g., the bands marked with (n,m), where both *n* and *m* are not equal to zero.

The categories of the bands and the value of their power are shown in Table 2.1.

Table 2.1 The categories of the bands in Figure 2.4 and their power.

$\omega_1 = 0.03\omega_0$. $\omega_2 = 1.9\omega_1 = 0.057\omega_0$. $R_0 = 10$ μm. $\varepsilon_1 = \varepsilon_2 = 0.05$.

	n	*m*	ω/ω$_0$	Power
Main bands	1	0	0.030	8.57×10^{-3}
	0	1	0.057	9.09×10^{-3}
Harmonics	2	0	0.060	1.16×10^{-4}
	3	0	0.090	9.53×10^{-6}
	0	2	0.114	1.42×10^{-4}
	0	3	0.171	2.88×10^{-6}
	0	4	0.228	1.83×10^{-6}
Combination bands	-1	1	0.027	2.76×10^{-4}
	-1	2	0.084	1.46×10^{-5}
	-1	3	0.141	3.58×10^{-6}
	1	1	0.087	2.93×10^{-4}
	1	2	0.144	5.62×10^{-6}
	1	3	0.201	2.24×10^{-6}
	2	-1	0.003	2.17×10^{-5}
	2	1	0.117	6.85×10^{-6}
	2	2	0.174	2.72×10^{-6}
	3	1	0.147	3.32×10^{-6}
	3	2	0.204	2.06×10^{-6}

To investigate the properties of these bands, the power of the bands in Figure 2.4 are plotted versus *n* and *m* in Figure 2.5. The size of the circle reflects the amplitude of the power of the band shown in Figure 2.4. From Figure 2.5, one can conclude that the power of the band decreases with the increase of $|n|+|m|$. Table 2.2 summarizes the relationship between $|n|+|m|$ and the band power. Basically, for the same value of $|n|+|m|$, the power of the bands is of the same order. In this section, for the purpose of simplification, we assume that $\varepsilon_1 = \varepsilon_2$. For more general cases, readers are referred to Sec. 2.3.

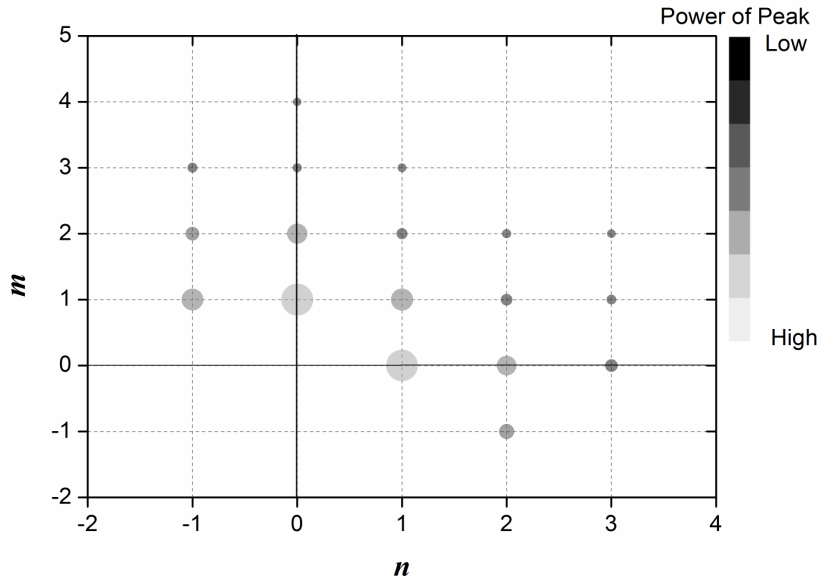

Figure 2.5 The power of various resonances shown in Figure 2.4 plotted versus n and m. $R_0 = 10$ μm. $\omega_1 = 0.03\omega_0$. $\omega_2 = 1.9\omega_1 = 0.057\omega_0$. $\varepsilon_1 = \varepsilon_2 = 0.05$. The size and the greyscale of the circles in the figure represent the power of the bands.

Table 2.2 The power of the bands in Figure 2.4, as a function of *n*, *m* and $|n|+|m|$.

n	*m*	$\|n\|+\|m\|$	Power
1	0	1	8.57×10^{-3}
0	1		9.09×10^{-3}
1	1	2	2.93×10^{-4}
-1	1		2.76×10^{-4}
0	2		1.42×10^{-4}
2	0		1.16×10^{-4}
2	-1	3	2.17×10^{-5}
-1	2		1.46×10^{-5}
3	0		9.53×10^{-6}
2	1		6.85×10^{-6}
1	2		5.62×10^{-6}
0	3		2.88×10^{-6}
-1	3	4	3.58×10^{-6}
3	1		3.32×10^{-6}
2	2		2.72×10^{-6}
1	3		2.24×10^{-6}
0	4		1.83×10^{-6}
3	2	5	2.06×10^{-6}

2.2.2 Combination resonances

By comparing Figures 2.3 and 2.4, one can find that the combination resonance is one of the unique features of the bubble oscillations under dual-frequency excitation. In this section, the combination resonance at $\omega_p \approx \omega_1 + \omega_2$, i.e., band (1,1), is taken as an example to illustrate the characteristics of the combination resonance.

To investigate the influence of the driving frequencies on combination resonances, four cases with the fixed ω_1 (equal to $0.35\omega_0$) and different ω_2 (equal to $0.65\omega_0$, $0.45\omega_0$, $0.25\omega_0$ and $0.85\omega_0$ respectively) are studied. Figure 2.6 shows a comparison of the power spectra between the four cases, and the value of $|\omega_1 + \omega_2 - \omega_0|$ increases from image (a) to (d). The powers of the main band (1,0) and the combination band (1,1) [represented as P(1,0) and P(1,1) respectively] are listed in Table 2.3. For comparison between different cases, the power of band (1,1) is non-dimensionalized using the power of band (1,0). Figure 2.6 and Table 2.3 both reveal that P(1,1) reaches a maximum value when $\omega_1 + \omega_2 = \omega_0$ (i.e., $\omega_2 = 0.65\omega_0$), which is even higher than the power of main band P(1,0). Moreover, the value of P(1,1) decreases with the increase of the value of $|\omega_1 + \omega_2 - \omega_0|$.

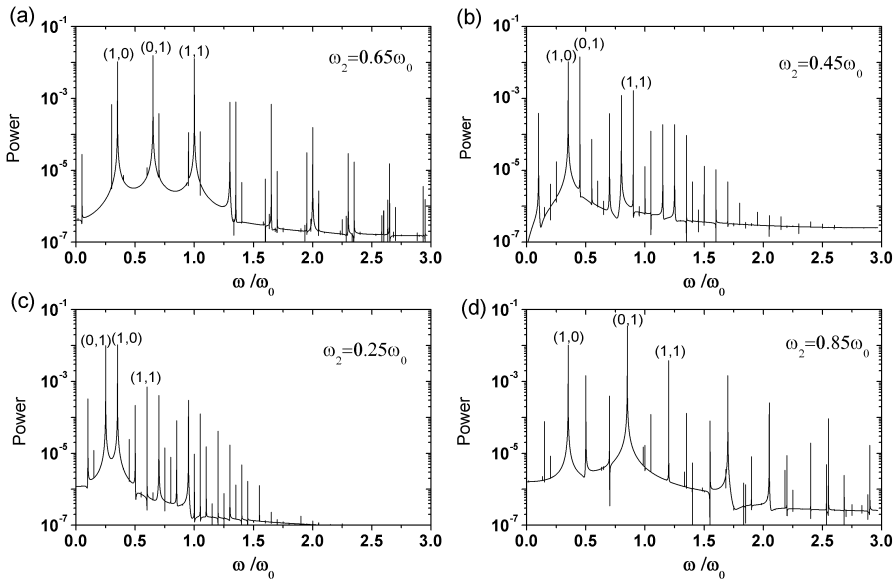

Figure 2.6 Power spectra of bubble oscillations under dual-frequency acoustic excitation. $\omega_1 = 0.35\omega_0$. (a) $\omega_2 = 0.65\omega_0$; (b) $\omega_2 = 0.45\omega_0$; (c) $\omega_2 = 0.25\omega_0$; (d) $\omega_2 = 0.85\omega_0$. $R_0 = 10$ μm. $\varepsilon_1 = \varepsilon_2 = 0.05$.

Table 2.3 The power of bands (1,0) and (1,1) for different cases shown in Figure 2.6.

	ω_2			
	$0.65\,\omega_0$	$0.45\,\omega_0$	$0.25\,\omega_0$	$0.85\,\omega_0$
P(1,0)	0.0105	0.0107	0.0106	0.0104
P(1,1)	0.0128	0.0012	0.0007	0.0038
P(1,1)/P(1,0)	1.22	0.11	0.07	0.37

For a more direct investigation, frequency response curves of bubble oscillation amplitudes [represented by $X_{\max} = \left(R_{\max} - R_0\right)/R_0$] are calculated by fixing the frequency of one component of the driving sound waves while changing the other. Figures 2.7 and 2.8 compare the response curves of gas bubble oscillations under single- and dual-frequency excitation with P_e/P_0 equalling to 0.0707 and 0.424 respectively. One of the component frequencies (ω_1) remains as $0.35\omega_0$. The integers with brackets above the peaks stand for (*n*,*m*). Same as the definition in Sec. 2.2.1, the peaks can be classified into:

a) Main resonance, i.e., (0,1).

b) Harmonics, e.g., (0,*m*). *m*=1,2,….

c) Subharmonics, e.g., $\left(0, \frac{1}{2}\right)$ as shown in Figure 2.8.

d) Combination resonances, e.g., (n, m) with both *n* and *m* not equal to zero.

Both curves in Figure 2.7 show harmonics (0,2), but only the curve corresponding to the dual-frequency excitation shows combination resonances, i.e., peaks marked by (1,1) and (-1,1). In the regions below and above the main resonance, the oscillation amplitudes of the bubble under dual-frequency excitation are higher than those under single-frequency excitation. In contrast, in the region near the main

resonance, the oscillation amplitudes under dual-frequency excitation are smaller than those under single-frequency excitation. Therefore, in the regions below and above the main resonance, the addition of the second acoustic wave can strengthen the bubble oscillations while in the region near the main resonance, the addition of the second acoustic wave would not enhance the bubble oscillation. In Figure 2.8, the combination resonances of higher orders, e.g., peaks marked with (2,1), (1,2), (-3,1), are present in the case with a relatively high pressure amplitude ($P_e/P_0 = 0.424$). The appearance of these combination resonances strengthens the bubble oscillations under dual-frequency excitation significantly. However, the subharmonic resonance marked as $\left(0, \frac{1}{2}\right)$ is suppressed under the dual-frequency excitation.

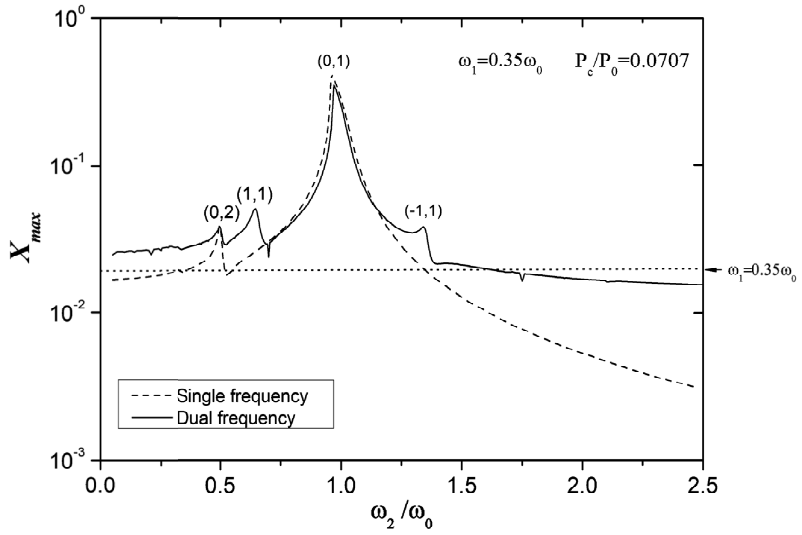

Figure 2.7 Response curves of gas bubble oscillations under the single-frequency excitation (dashed line) and the dual-frequency excitation (solid line). The horizontal line (dotted line) indicates the oscillation amplitude of bubbles under single-frequency excitation with frequency ω_1 . $\omega_1 = 0.35\omega_0$. $R_0 = 10$ μm. N =1. $P_e/P_0 = 0.0707$. $X_{\max} = \left(R_{\max} - R_0\right)/R_0$.

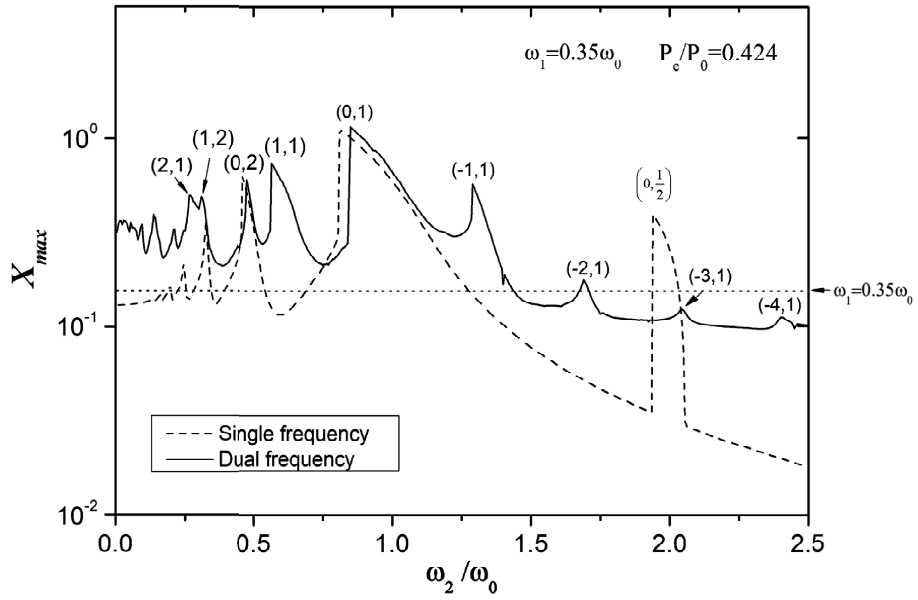

Figure 2.8 Response curves of gas bubble oscillations under the single-frequency excitation (dashed line) and the dual-frequency excitation (solid line). The horizontal line (dotted line) indicates the oscillation amplitude of bubbles under the single-frequency excitation with frequency ω_1. $\omega_1 = 0.35\omega_0$. $R_0 = 10$ μm. N =1. $P_e/P_0 = 0.424$. $X_{\max} = \left(R_{\max} - R_0\right)/R_0$.

2.2.3 Simultaneous resonances

For oscillators under multi-frequency excitation, more than one resonance might occur simultaneously (Nayfeh and Mook, 1979). For instance, simultaneous resonances may occur: when $\omega_1 \approx (2/3)\omega_0$ and $\omega_2 \approx (1/3)\omega_0$ (i.e., $\omega_1 + \omega_2 \approx \omega_0$), harmonic (0,3) and combination resonance (1,1) happen together; when $\omega_1 \approx (1/2)\omega_0$ and $\omega_2 \approx 2\omega_0$ (i.e., $\omega_2 - 2\omega_1 \approx \omega_0$), harmonic (2,0), subharmonic $\left(0, \frac{1}{2}\right)$ and combination resonance (-2,1) happen together.

Figure 2.9 demonstrates typical simultaneous resonances. When ω_2/ω_0 varies between 0.35 and 0.65, the response curves of bubble oscillation for the cases with different ω_1 (equal to $1.4\omega_0$, $1.45\omega_0$, $1.5\omega_0$, and $1.6\omega_0$ respectively) are compared. As shown in Figure 2.9, there are two peaks in the range of ω_2, i.e., the combination resonance (1,-1) and the harmonic (0,2), for the cases with ω_1 equalling to $1.4\omega_0$, $1.45\omega_0$, and $1.6\omega_0$. And with the value of ω_1 approaching to $1.5\omega_0$, the combination resonance (1,-1) is getting close to the harmonic resonance (0,2). When $\omega_1 = 1.5\omega_0$, the two peaks merge into one peak at $\omega_2 = 0.5\omega_0$, which means that the combination resonance and the first harmonic occur simultaneously in this situation.

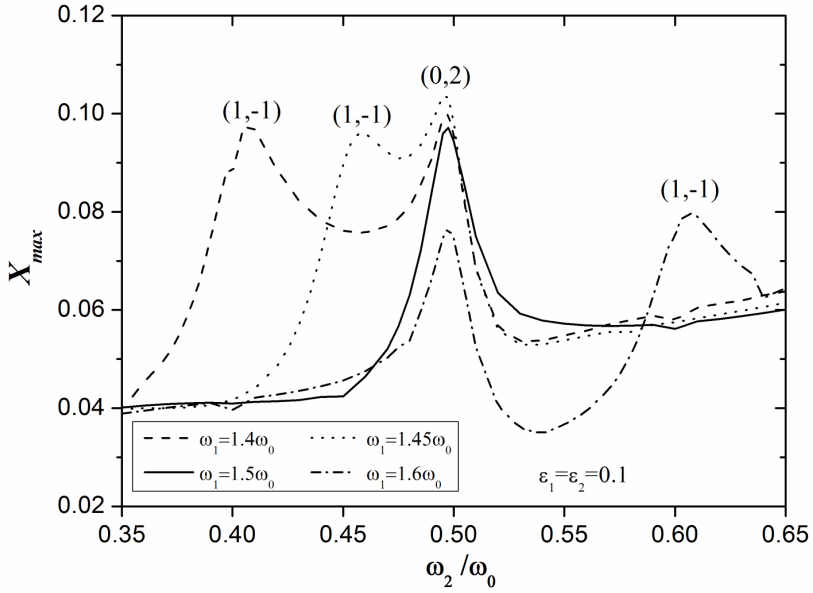

Figure 2.9 Response curves of bubble oscillation under dual-frequency excitation when $\omega_2/\omega_0 = 0.35-0.65$ with: $\omega_1 = 1.4\omega_0$ (dashed line); 1.45 ω_0 (dotted line); 1.5 ω_0 (solid line); 1.6 ω_0 (dash-dotted line) respectively. $R_0 = 10$ μm. N =1. $P_e/P_0 = 0.141$. $X_{\max} = \left(R_{\max} - R_0\right)/R_0$.

2.3 Influential parameters on bubble dynamics under dual-frequency excitation

In this section, the influence of several essential parameters of the dual-frequency approach is numerically investigated, including the acoustic pressure amplitude (P_e/P_0), the equilibrium radius of bubble (R_0), the energy allocation between two component frequencies (N), the frequency of the acoustic wave (ω_1) and the phase difference between two component acoustic waves ($\Delta\varphi = \varphi_2 - \varphi_1$).

2.3.1 Influence of the amplitude of sound pressure and the bubble size

Figures 2.10-2.12 show the response curves of bubble oscillations under dual-frequency excitation with different pressure amplitude. The equilibrium radii of bubbles are 1 μm, 10 μm, and 50 μm respectively. Similar with the characteristics of the response curves under single-frequency excitation (as shown in Figure 1.4), the amplitudes of the main resonances, the harmonics and the subharmonics increase with the increase of the acoustic pressure amplitude. And they lean over towards smaller bubble radii at higher acoustic pressure amplitudes, as shown in Figures 2.11 and 2.12. The amplitudes of the combination resonances also increase with increasing pressure amplitude. The amplitudes of the combination resonances of higher orders (i.e., large values of $|n|+|m|$) are smaller than those of lower orders (i.e., small values of $|n|+|m|$), but may grow faster with the increase of the pressure amplitude. As shown in Figure 2.12, there exist thresholds for subharmonics. The width of all the resonances grows with the increase of pressure amplitude.

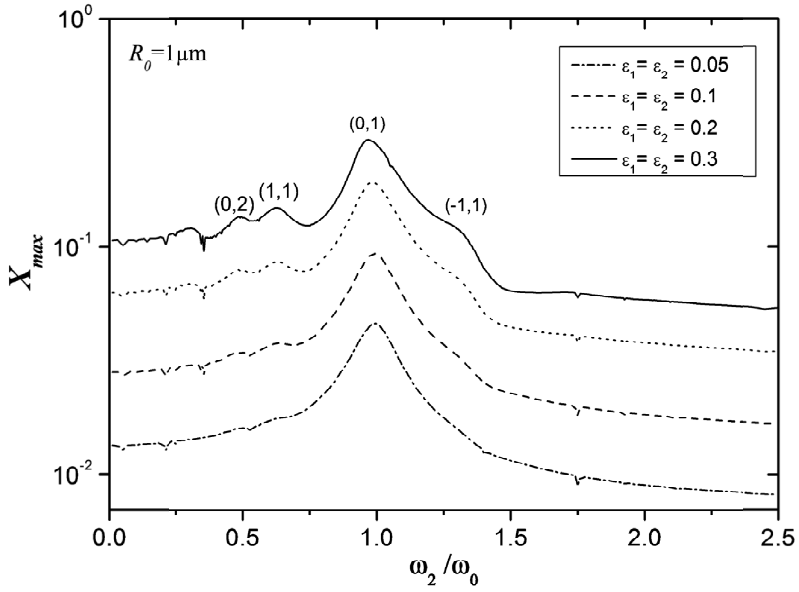

Figure 2.10 Response curves of bubble oscillation under dual-frequency excitation with different pressure amplitudes: $\varepsilon_1 = \varepsilon_2 = 0.05$ (dash-dotted line), 0.1 (dashed line), 0.2 (dotted line), 0.3 (solid line). $R_0 = 1\,\mu$m. $\omega_1 = 0.35\omega_0$. $X_{\max} = \left(R_{\max} - R_0\right)/R_0$.

The equilibrium radii of bubbles can also affect the bubble oscillations. For small bubbles (R_0 =1 μm, shown in Figure 2.10), the bubble oscillation is damped, leading to a strong suppression of the harmonics and the combination resonances. In contrast, under the same pressure amplitude, the harmonics and the combination resonances of high orders are more obvious in the cases with bigger bubble radii ($R_0 = 10$ μm and 50μm, shown in Figures 2.11 and 2.12). Furthermore, in Figure 2.12, the response curves of bubble with equilibrium radius of 50 μm show several

subharmonics or a combination of subharmonics, such as $\left(0,\frac{1}{2}\right)$, $\left(\frac{1}{2},\frac{1}{2}\right)$, and $\left(\frac{1}{2},1\right)$, which reveals that the increase of the bubble size will lower the thresholds of the subharmonics.

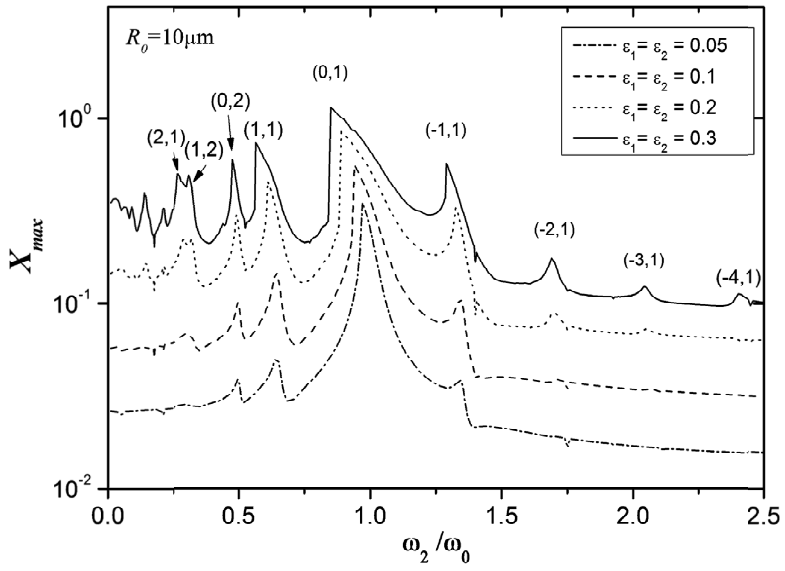

Figure 2.11 Response curves of bubble oscillation under dual-frequency excitation with different pressure amplitudes: $\varepsilon_1 = \varepsilon_2 = 0.05$ (dash-dotted line), 0.1 (dashed line), 0.2 (dotted line), 0.3 (solid line). $R_0 = 10$ μm. $\omega_1 = 0.35\omega_0$. $X_{\max} = \left(R_{\max} - R_0\right)/R_0$.

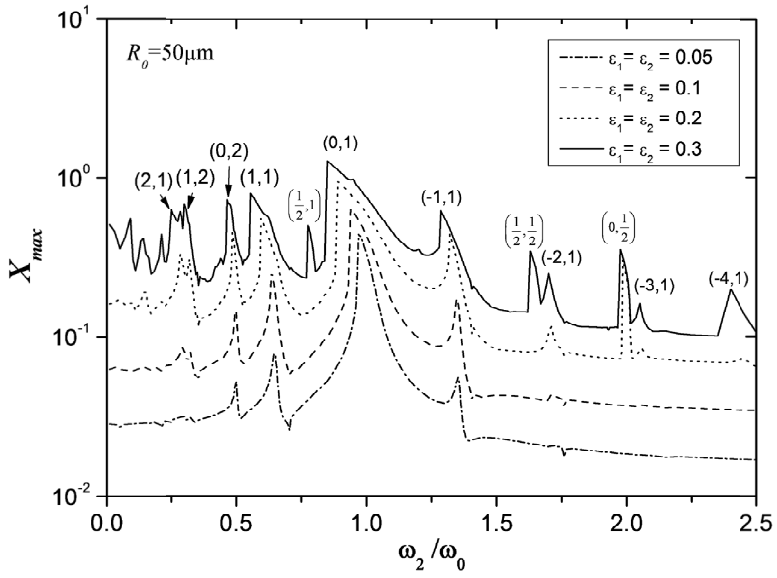

Figure 2.12 Response curves of bubble oscillation under dual-frequency excitation with different pressure amplitudes: $\varepsilon_1 = \varepsilon_2 = 0.05$ (dash-dotted line), 0.1 (dashed line), 0.2 (dotted line), 0.3 (solid line). $R_0 = 50$ μm. $\omega_1 = 0.35\omega_0$. $X_{\max} = \left(R_{\max} - R_0\right)/R_0$.

2.3.2 Influence of the energy allocation between two component sound waves

The energy allocated between the two component sound waves, indicated by N ($N = P_{A2}/P_{A1}$), can affect the power spectrum of bubble oscillations. Figure 2.13 shows the power spectra of bubble oscillations under dual-frequency excitation with different N. The frequencies of the external acoustic waves employed here are far below the natural resonance, i.e., $\omega_1 = 0.03\omega_0$ and $\omega_2 = 1.9\omega_1 = 0.057\omega_0$. R_0 is 10 μm. As shown in Figure 2.13, when the pressure amplitude of one component wave rises, the power of the bands corresponding to its main resonance and harmonics [i.e., the peaks of (n,0) or (0,m)] will increase. On the contrary, with the decrease of the pressure amplitude of this component wave, the power of the corresponding bands decreases, even possibly disappears. For instance, the peaks of (0,3), (1,3), (0,4) vanish when N<1. Compared to the case with $N = 1$, the change of N suppresses the power of combination resonances (1,1) and (-1,1).

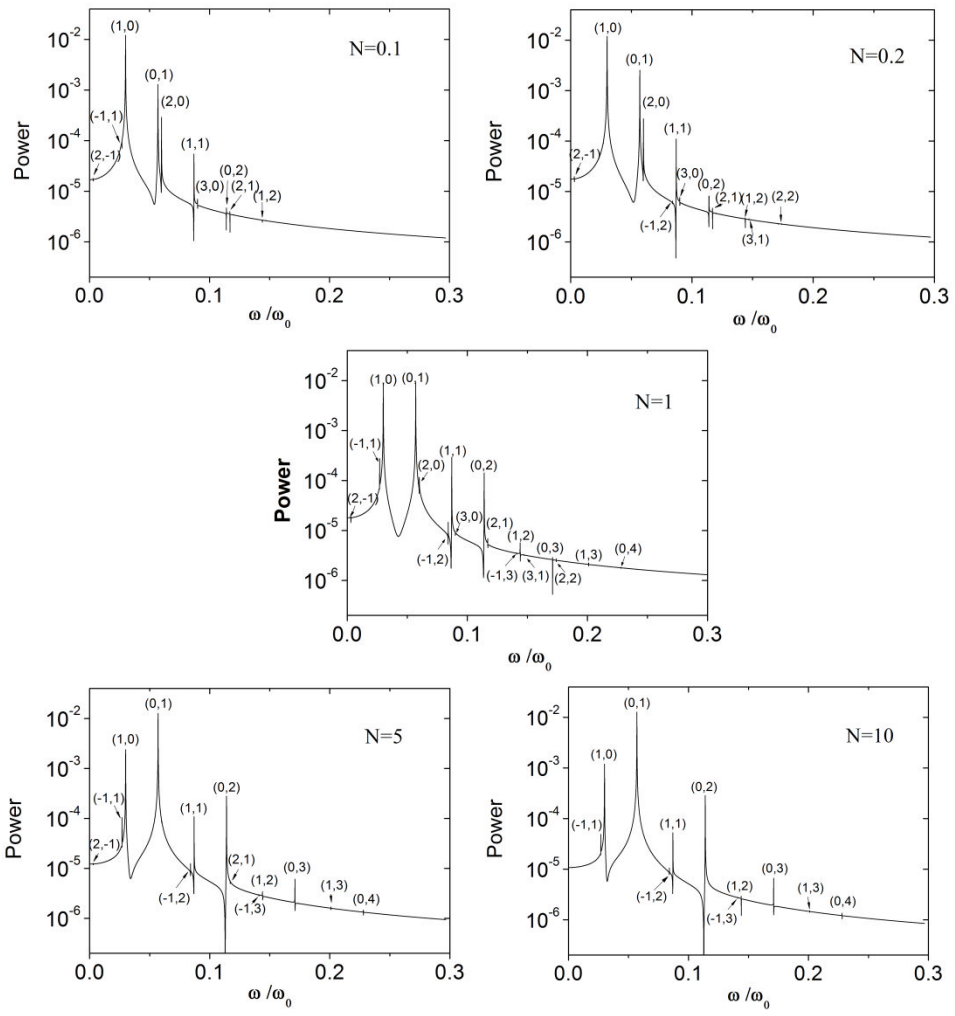

Figure 2.13 Power spectra of bubble oscillations under dual-frequency excitation with N = 0.1, 0.2, 1, 5, and 10 respectively. $R_0 = 10$ μm. $\omega_1 = 0.03\omega_0$. $\omega_2 = 1.9\omega_1 = 0.057\omega_0$. $P_e/P_0 = 0.0707$.

The response curves under the dual-frequency excitation with different *N* are compared with the response curve under the single-frequency excitation in Figures 2.14 and 2.15. For the dual-frequency excitation, one of the component frequencies is fixed at $\omega_1 = 0.35\omega_0$ and the other frequency ω_2 varies from $0.01\omega_0$ to $2.5\omega_0$. The total power input P_e/P_0 remains as constant 0.0707 in Figure 2.14 and 0.424 in Figure 2.15. *N*=0.2, 0.5, 1, 2, and 5 respectively. When ω_2 is above the main resonance, with decreasing *N*, the oscillation amplitudes increase except for the subharmonics [e.g., resonance at $\left(0,\frac{1}{2}\right)$] which are suppressed when $N \le 1$. In contrast, when ω_2 is near the main resonance, with increasing *N*, the oscillation amplitudes increase. When ω_2 is below the main resonance, the influence of *N* on bubble oscillations is much more complicated. For *N*<1, the oscillation amplitudes near the harmonics [i.e., (0,2)] decrease with decreasing *N* while they do not differ much when $N \ge 1$. However, for combination resonances (1,1) and (-1,1), the maximum values of oscillation amplitude are obtained in the case with *N*=1. The combination resonances of higher order are illustrated in Figure 2.15(b). The combination resonances (2,1), (1,2), (1,3), (2,2) reach their maximum values when $N \approx 1$. Figure 2.16 shows the influence of *N* on the amplitudes of combination resonances (1,1), (-1,1), (2,1) and (1,2) in details. ▲ indicates the maximum value of the amplitude of bubble

oscillations. One can find that the value of N corresponding to the maximum values of the combination resonances approximates to 1 and varies slightly with the order of the resonances.

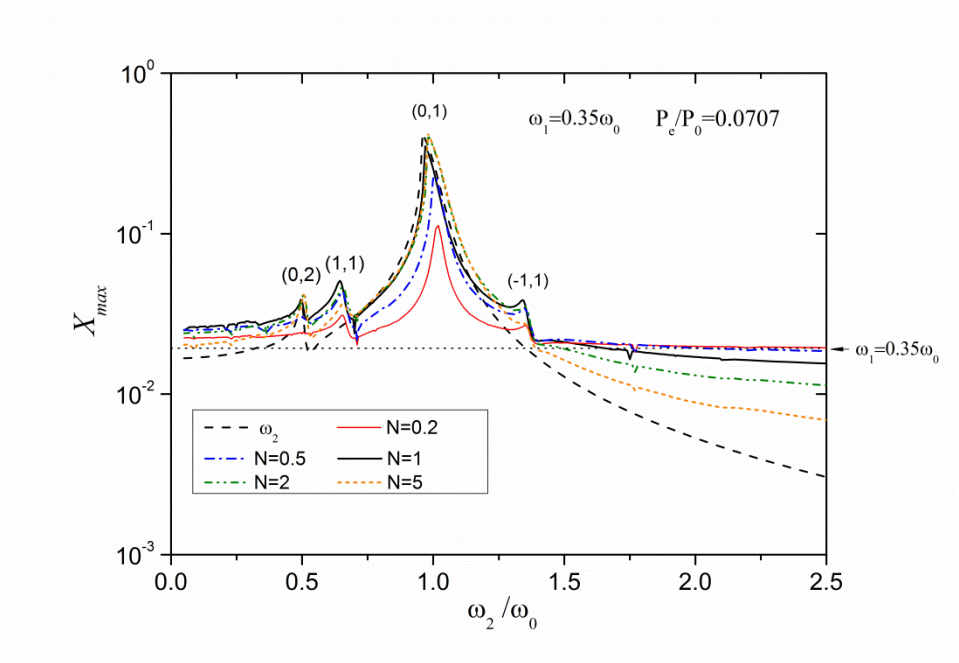

Figure 2.14 The response curves of bubble oscillation under single-frequency (dashed line) and dual-frequency acoustic excitation (with different N). The horizontal line indicates the oscillation amplitude of bubbles under single-frequency excitation with frequency ω_1. $R_0 = 10$ μm. $\omega_1 = 0.35\omega_0$. $P_e/P_0 = 0.0707$. N= 0.2, 0.5, 1, 2, 5 respectively. $X_{\max} = \left(R_{\max} - R_0\right)/R_0$.

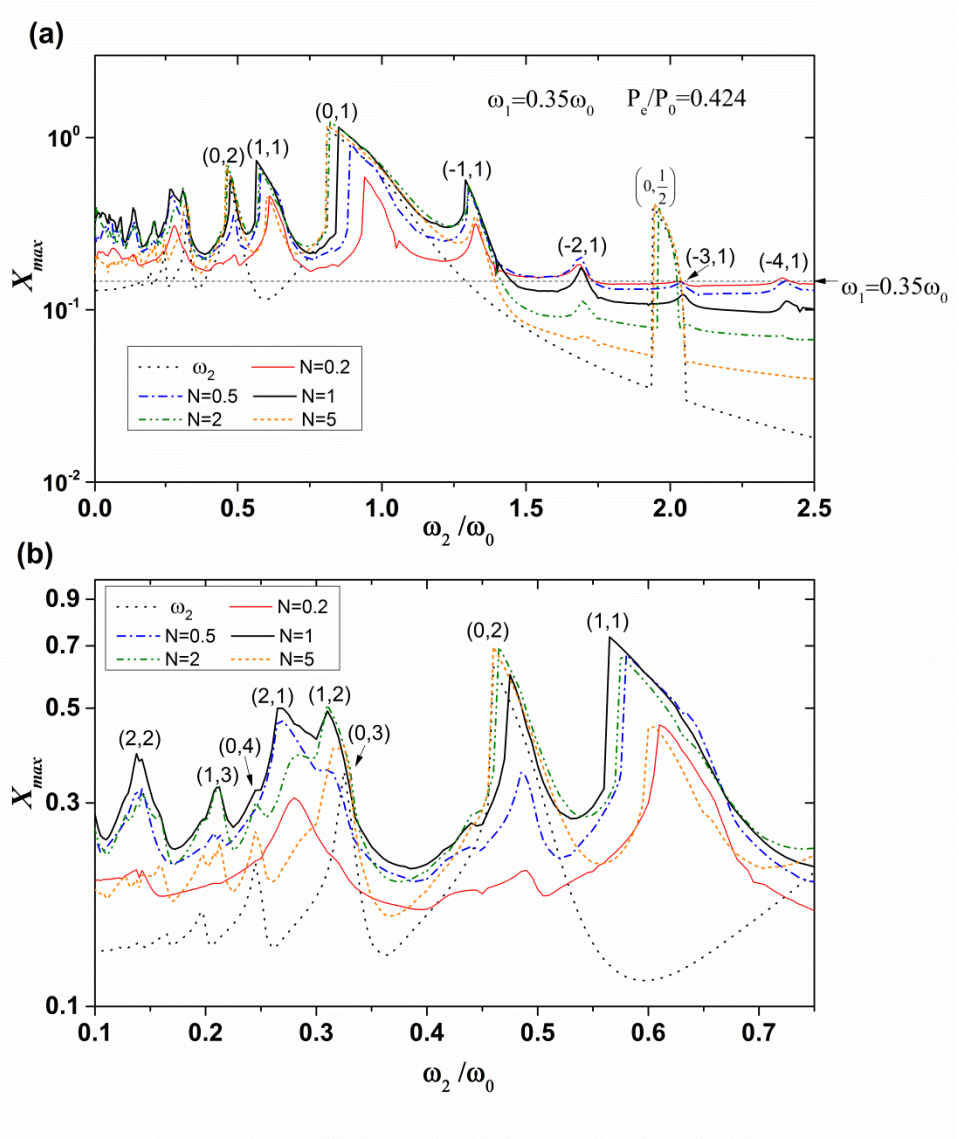

Figure 2.15 The response curves of bubble oscillation under single-frequency (dotted line) and dual-frequency acoustic excitation (with different *N*). The horizontal line indicates the oscillation amplitude of bubbles under single-frequency excitation with frequency ω_1. $R_0 = 10$ μm. $\omega_1 = 0.35\omega_0$. $P_e/P_0 = 0.424$. *N* = 0.2, 0.5, 1, 2, 5 respectively. The two numbers with brackets above the peaks stand for (*n*,*m*). $X_{\max} = \left(R_{\max} - R_0\right)/R_0$.

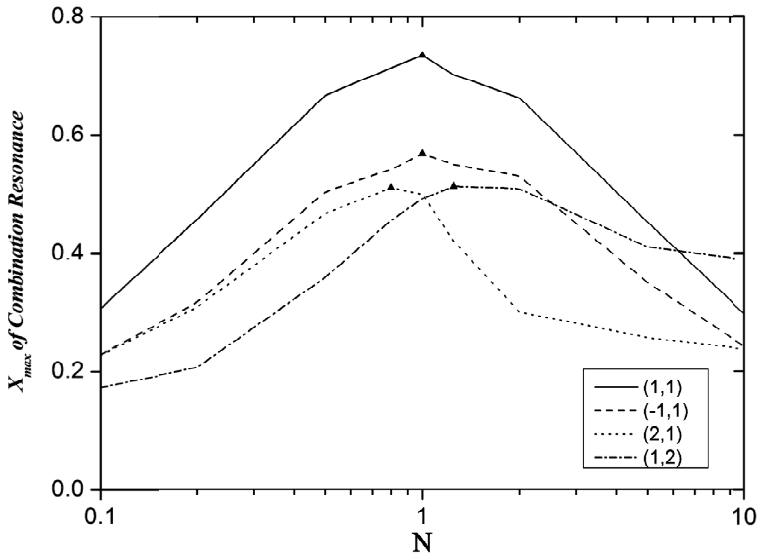

Figure 2.16 Amplitude of bubble oscillations versus power allocation *N* at different combination resonances: (1,1) solid line, (-1,1) dashed line, (2,1) dotted line, (1,2) dash-dotted line. ▲ indicates the maximum value of $X_{\max}$. $R_0 = 10$ μm. $\omega_1 = 0.35\omega_0$. $P_e/P_0 = 0.424$. $X_{\max} = \left(R_{\max} - R_0\right)/R_0$.

2.3.3 Influence of phase difference

Figure 2.17 shows the bubble oscillations (steady oscillation) under dual-frequency excitation with the phase difference between the component acoustic waves equal to zero, $\pi/2$, π , and $3\pi/2$ respectively. As shown in Figure 2.17, the waveforms of the bubble motion for different cases are quite different. For further investigation, the corresponding response curves for different phase difference are shown in Figure 2.18. The response curves overlap, which means that the amplitude of bubble oscillations is not influenced by the phase difference between the component acoustic waves.

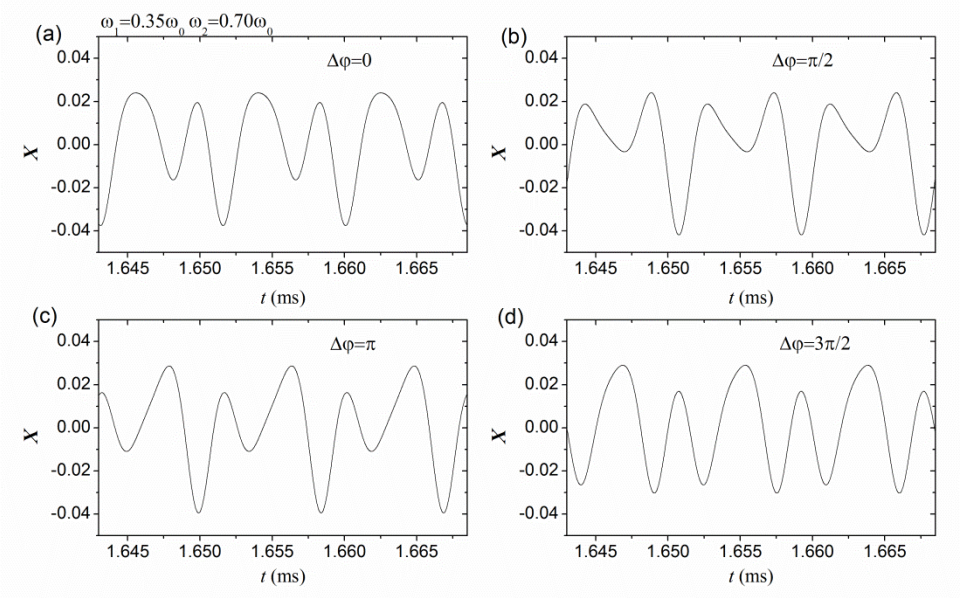

Figure 2.17 Variations of the non-dimensional bubble radius during its oscillation under dual-frequency acoustic excitation versus time. $\Delta\varphi = \varphi_2 - \varphi_1 =$ 0 (a), $\pi/2$ (b), π (c), $3\pi/2$ (d) respectively. $\omega_1 = 0.35\omega_0$. $\omega_2 = 0.7\omega_0$. $\varepsilon_1 = \varepsilon_2 = 0.05$. $R_0 = 10$ μm. $X = \left(R - R_0\right)/R_0$.

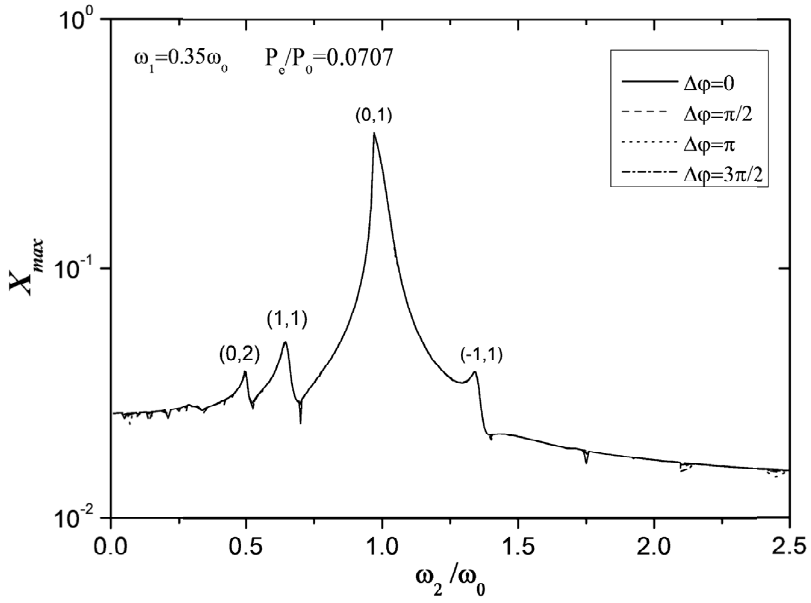

Figure 2.18 Response curves of bubble oscillations under dual-frequency excitation with different phase difference: $\Delta\varphi = \varphi_2 - \varphi_1 = 0$ (solid line), π/2 (dashed line), π (dotted line), 3π/2 (dash-dotted line) respectively. $X_{\max} = \left(R_{\max} - R_0\right)/R_0$. $\omega_1 = 0.35\omega_0$. $\omega_2 = 0.7\omega_0$. $\varepsilon_1 = \varepsilon_2 =$ 0.05. $R_0 = 10$ μm.

2.3.4 Influence of driving frequency

Figure 2.19 compares the response curves of bubble oscillations under dual-frequency excitation with different driving frequency ω_1. Firstly, the variation of ω_1 would influence the positions of the combination resonances, for instance, the position of the peaks (1,1) and (-1,1). Secondly, the amplitude of bubble oscillations under single-frequency excitation with different driving frequencies (i.e., ω_1) decreases following

the order ω_1 equalling to $0.8\omega_0$, $0.5\omega_0$, $0.35\omega_0$, $2.35\omega_0$ (indicated as the horizontal lines in Figure 2.19). In the regions below and above the main resonance, the amplitudes of bubble oscillations decrease following the same order. Particularly, for the case with $\omega_1 = 2.35\omega_0$, the amplitude of bubble oscillations under dual-frequency excitation is even smaller than those under single-frequency excitation. Thirdly, in the region near the main resonance, the amplitudes of bubble oscillation do not differ much between cases with different driving frequencies.

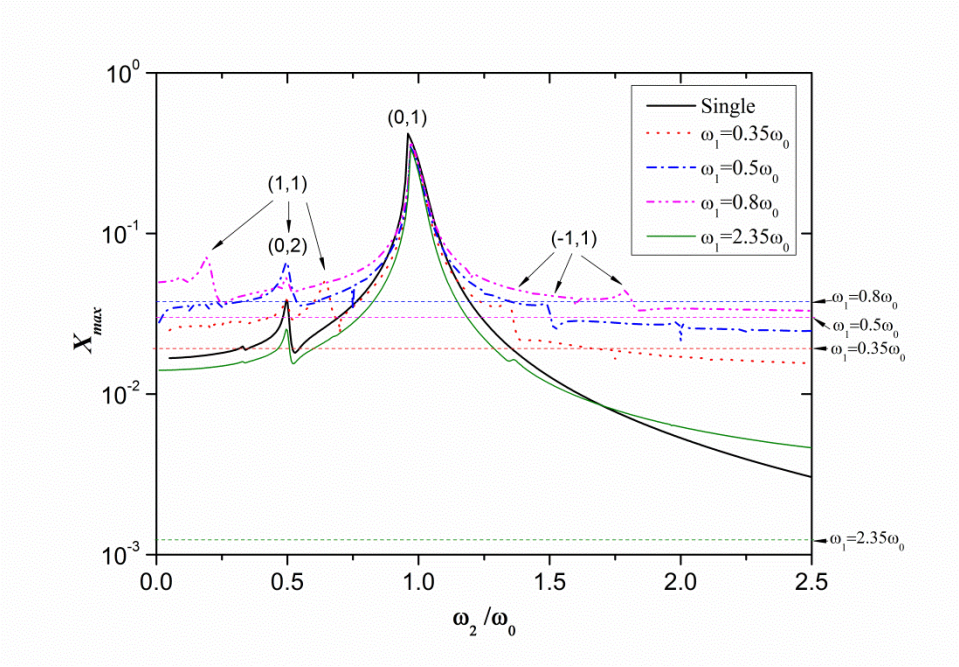

Figure 2.19 Response curves of bubble oscillation under dual-frequency excitation with frequencies: $\omega_1 = 0.8\omega_0$, $0.5\omega_0$, $0.35\omega_0$, $2.35\omega_0$. The horizontal line (dashed line) indicates the oscillation amplitude of bubbles under single-frequency excitation with frequency ω_1. $\varepsilon_1 = \varepsilon_2 = 0.05$. $R_0 = 10$ μm. $X_{\max} = (R_{\max} - R_0)/R_0$.

2.4 Summary

In this chapter, the bubble motion equation has been solved by the fourth order Runge-Kutta method. It is assumed that the bubble oscillates spherically symmetrically in a Newtonian fluid (i.e., water). Only radial motion of the bubble is considered. And vapour pressure in the bubble is omitted. Then, FFT and response curves were employed to reveal the fundamentals of the bubble dynamics under dual-frequency excitation.

Both the power spectrum and the response curve under dual-frequency excitation show the main, harmonic and subharmonic resonances corresponding to the two component acoustic waves. Besides these resonances, for the dual-frequency approach, there exist combination and simultaneous resonances. The corresponding frequencies of the resonances can be expressed by a linear combination of the two component frequencies, i.e., $n\omega_1 + m\omega_2 = \omega_0$. The power of the bands of the resonances decreases with the value of $|n| + |m|$ in the power spectrum. By comparing the response curves of single- and dual-frequency excitation, one can conclude that in the regions below and above the main resonance, the addition of the second acoustic wave could strengthen the bubble oscillations while in the region near the main resonance, the addition of the second acoustic wave would not enhance the amplitudes of

bubble oscillations. For a dual-frequency approach, if the driving frequencies satisfy particular conditions, several resonances (e.g., combination resonances and harmonics, or combination resonances and subharmonics) may occur simultaneously.

The influential parameters of the dual-frequency approach on bubble oscillations are also discussed in this chapter, including the pressure amplitude, the equilibrium bubble radius, the power allocation between the component waves, the phase difference and the driving frequency.

With increasing pressure amplitude, all the resonances increase and lean over toward lower frequency. There exist pressure thresholds for subharmonics and ultraharmonics. For the cases with small equilibrium bubble radius, the resonances are suppressed. For the cases with large equilibrium bubble radius, the thresholds of the subharmonics and the ultraharmonics are reduced.

The power allocation between the two component driving waves (indicated by N) also affects the bubble dynamics. With decreasing N, the oscillation amplitude increases in the region above the main resonance and decreases in the region near the main resonance. For $N<1$, the oscillation

amplitudes near the harmonics decrease with the decrease of N while they do not differ much when $N \geq 1$. The oscillation amplitudes near the combination resonances reach the maximum values when $N \approx 1$.

The phase difference between the two driving acoustic waves influences the waveform of the bubble motion significantly while it leads to little change of the oscillation amplitudes. The variations of the driving frequency ω_1 induce the change of position of the combination resonances. In the regions below and above the main resonance, the oscillation amplitudes of bubbles change with ω_1. In the region near the main resonance, the influence of ω_1 is very limited.

Chapter 3 Acoustical Scattering Cross Section of Gas Bubbles under Dual-Frequency Acoustic Excitation

In this chapter, the acoustical scattering cross section of gas bubbles in liquids excited by dual-frequency acoustic waves is theoretically investigated. Parts of this chapter have been accepted as a journal paper (Zhang and Li, 2015, in press).

The whole chapter is organized as follows. In Sec. 3.1, equations relating with the acoustical scattering cross section of gas bubbles are briefly introduced. In Sec. 3.2, both the analytical solution and the numerical simulation of the acoustical scattering cross section are given. In Sec. 3.3, the analytical solution and the numerical simulation are compared, together with the discussions of the valid region of the analytical solution. In Sec. 3.4, the nonlinear nature of the acoustical scattering cross section of gas bubbles under dual-frequency excitation is revealed with examples demonstrated. In Sec. 3.5, the influence of several paramount parameters

(e.g., the acoustic pressure amplitude, the energy allocation between two component waves and the ratio of the two frequencies) on the scattering cross section is shown. In this chapter, it is assumed that the bubble oscillates spherically symmetrically in a Newtonian fluid (i.e., water). Only radial motion of the bubble is considered. And vapour pressure in the bubble is omitted.

3.1 Basic equations

In this section, basic equations relating to the acoustical cross section are introduced. The basic equation of bubble motion is the Keller-Miksis equation [Eqs. (2.1)-(2.4)] (Keller and Miksis, 1980).

The radiation pressure at radial coordinate r from the origin of bubble centre can be given as[1] (Yang and Church, 2005)

$$P_{rad}(r,t) = \frac{\rho_l R}{r}\left(2\dot{R}^2 + R\ddot{R}\right). \tag{3.1}$$

Here, P_{rad} is the radiation pressure; r is the radial coordinate with the

[1] This equation can be rewritten as $P_{rad} = \frac{\rho_l}{4\pi r}\cdot\frac{d^2 v}{dt^2}$, where v is the instantaneous volume of the bubble. Hence, the radiation pressure is related with the acceleration of the bubble volume, which, according to Eq. (3.4), has a phase difference with the time variation of the bubble radius. As a result, in Figures 3.1 and 3.2, when the bubble radius reaches its maximum, the corresponding radiation pressure reaches its minimum, and *vise versa*.

origin at the bubble centre. Solving Eqs. (2.1)-(2.4), one can obtain the solution of the bubble motion (e.g., the dynamic oscillations of R, $\dot{R}$ and $\ddot{R}$). Substituting this solution into Eq. (3.1), the radiation pressure generated by bubble oscillations can be obtained.

According to Eq. (3.1), one can find that the radiation pressure is a function of radial coordinate and hence it is not convenient for comparisons with cases with different parameters (e.g., bubble radius). Usually, another parameter, e.g., acoustical scattering cross section, which reflects the square of the ratios between scattered waves and incident waves, is employed. For convenience, the amplitude of the radiation pressure can be written as

$$\left|P_{rad}\right| = \left|\frac{B}{r}\right|.$$

Here, B/r is the amplitude of the divergent spherical scattered wave generated by bubble oscillations.

Following the definition proposed by Wildt (Wildt, 1946, Eq. 6), the acoustical scattering cross section (σ_s) of an oscillating gas bubble in a liquid can be defined as

$$\sigma_s = 4\pi \left|B / A\right|^2. \tag{3.2}$$

Here, A is the amplitude of the incident wave. Hence, σ_s reflects the

scattering ability of gas bubbles when they are excited by acoustic waves[2].

3.2 Solutions

3.2.1 Analytical solution

In this section, the analytical solution for acoustical scattering cross section under dual-frequency acoustic excitation is obtained. Assume that the solution of the Keller-Miksis equation under dual-frequency acoustic excitation [Eqs. (2.1), (2.2) and (2.4)] is

$$R/R_0 = 1 + \varepsilon_1 x\,. \tag{3.3}$$

Here, $\varepsilon_1 = P_{A1}/P_0$.

The solution of the equation of bubble motion under dual-frequency excitation [Eqs. (2.1), (2.2) and (2.4)] is (Zhang, 2012a)

$$x = A_{11}\cos\left(\omega_1 t + \delta_{11}\right) + A_{12}\cos\left(\omega_2 t + \delta_{12}\right), \tag{3.4}$$

where

[2] For a plane wave, the sound intensity (i.e., the average rate at which sound energy crosses a unit cross-sectional area of the soundbeam) is $I_0 = \dfrac{|A|^2}{2\rho_l c}$. The intensity of the wave scattered by the bubble at the distance r is $I_s = \dfrac{|P_{rad}|^2}{2\rho_l c} = \dfrac{|B|^2}{2\rho_l c r^2}$. Therefore, the total scattered energy at the distance r from the bubble centre $4\pi r^2 I_s = \sigma_s I_0$. For a bubble driven by a certain sound field, the bigger σ_s is, the higher the energy scattered by the bubble is. For more details, readers are referred to Wildt (1946).

$$A_{11} = -\frac{P_0}{M\rho_l R_0^2}\left[\frac{1+\left(\omega_1 R_0 / c_l\right)^2}{\left(\omega_0^2-\omega_1^2\right)^2+4\beta_{tot}^2\omega_1^2}\right]^{1/2}; \tag{3.5}$$

$$\delta_{11} = \tan^{-1}\left[\frac{\left(\omega_1 R_0 / c_l\right)\left(\omega_0^2-\omega_1^2\right)-2\beta_{tot}\omega_1}{\left(\omega_0^2-\omega_1^2\right)+2\beta_{tot}\omega_1^2 R_0 / c_l}\right]; \tag{3.6}$$

$$A_{12} = -\frac{P_0\varepsilon_{21}}{M\rho_l R_0^2}\left[\frac{1+\left(\omega_2 R_0 / c_l\right)^2}{\left(\omega_0^2-\omega_2^2\right)^2+4\beta_{tot}^2\omega_2^2}\right]^{1/2}; \tag{3.7}$$

$$\delta_{12} = \tan^{-1}\left[\frac{\left(\omega_2 R_0 / c_l\right)\left(\omega_0^2-\omega_2^2\right)-2\beta_{tot}\omega_2}{\left(\omega_0^2-\omega_2^2\right)+2\beta_{tot}\omega_2^2 R_0 / c_l}\right]; \tag{3.8}$$

$$\varepsilon_{21} = P_{A2} / P_{A1}.$$

with

$$M = 1+\frac{R_0}{c_l}\frac{4\mu_l}{\rho_l R_0^2},$$

$$\beta_{tot} = \beta_{vis}+\beta_{ac} = 2\mu_l / \rho_l R_0^2 M + \omega_0^2 R_0 / 2c_l, \tag{3.9}$$

$$\omega_0^2 = \frac{3\kappa(P_0+2\sigma / R_0)-2\sigma / R_0}{\rho_l R_0^2 M}. \tag{3.10}$$

Here, ω_0 is the natural frequency of the gas bubbles oscillating in the liquids; β_{tot}, β_{vis} and β_{ac} are the total, viscous and acoustic damping constants respectively.

Substituting Eq. (3.3) into Eq. (3.1) and only keep terms up to the first order of ε_1, one can obtain

$$B = \rho_l R_0^3 \varepsilon_1\left(A_{11}^2\omega_1^4 + A_{12}^2\omega_2^4\right)^{1/2}. \tag{3.11}$$

Therefore, acoustical scattering cross section is

$$\sigma_s = 4\pi \left| B / A \right|^2 = \frac{4\pi}{1+\varepsilon_{21}^2} \left(\rho R_0^3 / p_0 \right)^2 \left(A_{11}^2 \omega_1^4 + A_{12}^2 \omega_2^4 \right). \qquad (3.12)$$

For dual-frequency acoustic excitation, the amplitude of the incident wave (A) is the root of the sum of the square of the powers of the amplitudes of two frequencies P_e [$P_e = \left(P_{A1}^2 + P_{A2}^2 \right)^{1/2}$].

For single-frequency acoustic excitation, the generalized analytical solution of σ_s is (Zhang, 2013a)

$$\sigma_s = \frac{4\pi R_0^2}{\left[\frac{\omega_0^2}{\omega^2} - 1 \right]^2 M^2 + \left[\frac{4\mu_l}{\omega \rho_l R_0^2} + \frac{R_0}{\omega c_l} M \omega_0^2 \right]^2} C_1, \qquad (3.13)$$

with

$$C_1 = \frac{\left[\sin(2\pi R_0 / \lambda_l) / (2\pi R_0 / \lambda_l) \right]^2}{1 + \left(2\pi R_0 / \lambda_l \right)^2}.$$

Here, λ_l is the wavelength of acoustic wave in the liquid.

3.2.2 Numerical simulations

For the numerical simulations, Eqs. (2.1)-(2.4) are directly solved using an explicit Runge-Kutta formula (Dormand and Prince, 1980) for a range of parameters, including the bubble radius, pressure amplitude and the frequency of the acoustic excitation. Then Eqs. (3.1) and (3.2) are employed to obtain the radiation pressure and acoustical scattering cross section generated by the oscillating bubbles

The constants employed in analytical and numerical methods are the same as those shown in Appendix A. The distance from the origin r is 1×10^{-3} m. For simplicity, the values of the acoustical scattering cross section of individual air bubbles are normalized using their respective geometrical cross sections (i.e., πR_0^2). The ratio of pressure amplitudes of the two acoustic waves is defined as $N = P_{A2}/P_{A1}$. For comparison, the total input power, $P_e = \left(P_{A1}^2 + P_{A2}^2\right)^{1/2}$, remains as a constant during simulations of different cases.

In the following paragraphs, examples of the radiation pressure and the acoustical scattering cross section generated by an oscillating bubble under dual-frequency acoustic excitation within a wide range of parameters are shown. For comparison, cases under single-frequency acoustic excitation are also provided. In Sec. 3.3, the analytical solution in Sec. 3.2.1 and the numerical simulations in Sec. 3.2.2 are compared to show the differences between two approaches and hence the validity of the analytical solution is determined. Then, nonlinear characteristics and influential parameters (e.g., bubble radii, driving frequencies and power allocation between two acoustic waves) of the acoustical cross section are shown in Secs. 3.4 and 3.5.

Figures 3.1 and 3.2 demonstrate the variations of non-dimensional instantaneous bubble radius [$\left(R-R_0\right)/R_0$] and the radiation pressure versus time for a 10 μm bubble oscillating under single-frequency excitation and dual-frequency excitation respectively. During the expBoth the bubble oscillations and radiation pressure curves under single- and dual-frequency approaches clearly show periodical oscillations. However, the bubble oscillations and the radiation pressure curves under dual-frequency excitation exhibit much more complicated patterns. Additionally, the addition of the extra 200 kHz acoustic wave leads to a great increase of the amplitude of bubble oscillations (about two times) and radiation pressure (about seven times).

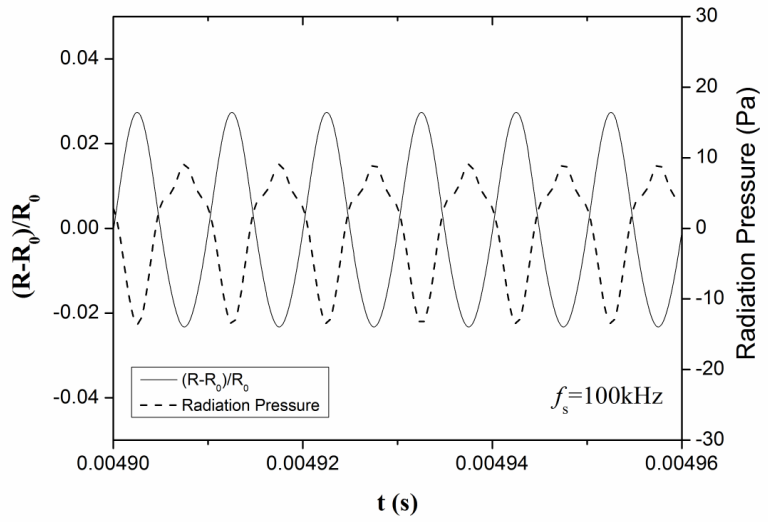

Figure 3.1 The non-dimensional instantaneous bubble radius under the single-frequency acoustic excitation (thin line) and corresponding radiation pressure (thick line) versus time. $f_s = 100$ kHz. $R_0 = 10$ μm. $P_e / P_0 = 0.1$. r =1 mm.

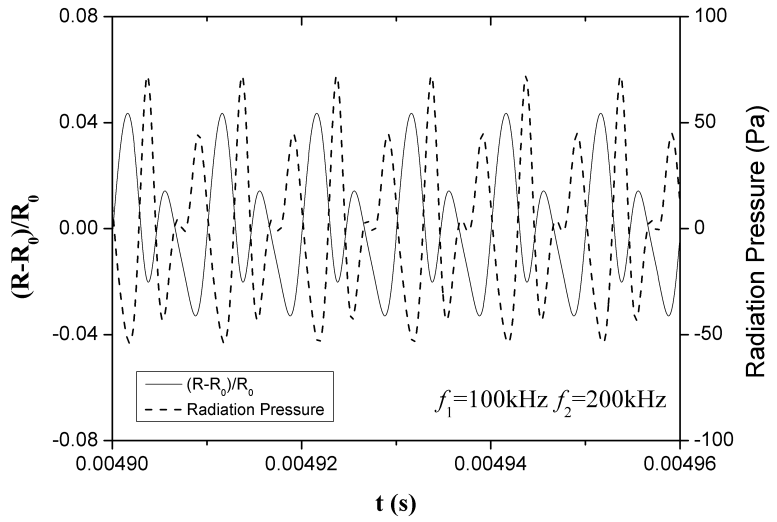

Figure 3.2 The non-dimensional instantaneous bubble radius under dual-frequency acoustic excitation (thin line) and corresponding radiation pressure (thick line) versus time. $f_1 = 100$ kHz. $f_2 = 200$ kHz. $R_0 = 10$ μm. $P_e / P_0 = 0.1$. $N = P_{A2} / P_{A1} = 1$. r =1 mm.

3.3 Comparisons between analytical solution and numerical simulations

Figures 3.3 and 3.4 show the acoustical scattering cross section curves (i.e., curves of $\sigma_s / \pi R_0^2$ versus equilibrium bubble radius) predicted by the analytical and numerical approaches under single-frequency excitation ($f_s = 100$ kHz) and dual-frequency excitation ($f_1 = 100$ kHz and $f_2 = 200$ kHz). The labels marked in Figures 3.3 and 3.4 reflect the nonlinear characteristics of the acoustical scattering cross section of gas

bubbles, which will be discussed in details in Sec. 3.4. When the acoustic pressure amplitude is small, e.g., $P_e/P_0 = 0.01$, a good agreement between the analytical solution and the numerical simulation has been found across the full range of R_0. According to Eqs. (3.12) and (3.13), the analytical solution of the acoustical scattering cross section is independent of the pressure amplitude of acoustic waves. With increasing P_e, the curves of σ_s predicted by numerical simulation show strong nonlinearity. For instance, harmonics are generated as shown in Figures 3.3 and 3.4. For P_e/P_0 = 0.05 and 0.1, the generation of the first harmonic is significant. When P_e/P_0 is beyond 0.1, the harmonics of higher orders are shown. Detailed discussions of those nonlinear features are given in Sec. 3.4. The analytical solution fails to predict those nonlinear phenomena, although the analytical solution still agrees well with the numerical prediction in the region away from resonances[3]. Near resonance, compared to those predicted by analytical solution, the curves predicted by the numerical simulations bend to the left, termed as "bending phenomenon" (Lauterborn and Kurz, 2010). This is also a nonlinear feature of the bubble

[3] Harmonics is one of the nonlinear features of the bubble oscillation system, determined by the nature of Eqs. (2.1)-(2.4). And there is no threshold for harmonics, so they increase with the growing pressure and becomes more obvious in Figures 3.3 and 3.4 even when P_e/P_0 = 0.05. The prediction of analytical solution may be more accurate in the region of resonances, if higher order of ε_1 in Eq. (3.3) is considered. However, the solution will be very complicated then and it is not necessary in this thesis which focuses on the special features under dual-frequency excitation. For more details about the solution up to higher order under single-frequency excitation, readers are referred to Prosperetti (1974).

motion equation Eqs. (2.1)-(2.4). For a more detailed discussion, readers are referred to Lauterborn and Kurz (2010). Hence, in the following sections, only the numerical approach is employed to study the acoustical scattering cross section generated by bubble oscillations.

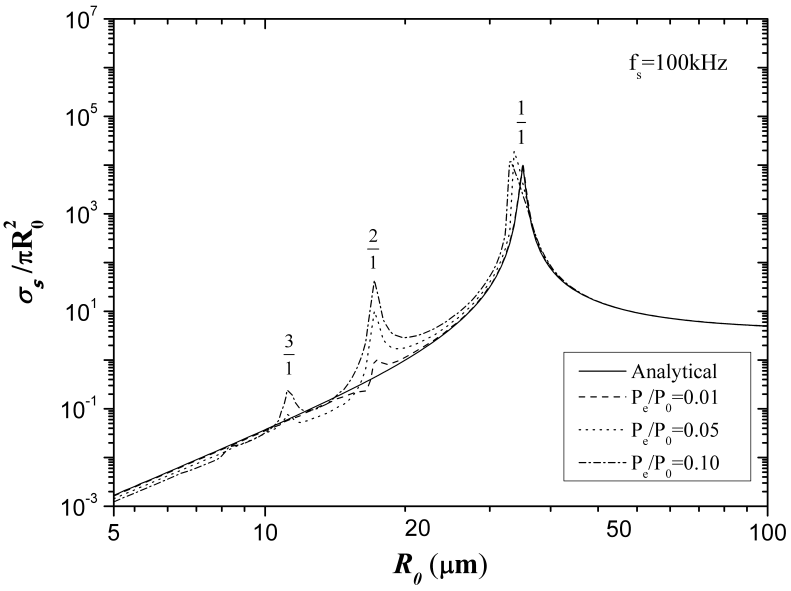

Figure 3.3 Predictions of acoustical scattering cross section versus equilibrium bubble radius under single-frequency acoustic excitation by analytical solution (solid line) and numerical method with $P_e/P_0 = 0.01$ (dashed line), 0.05 (dotted line), 0.1 (dash-dotted line) respectively. $f_s = 100$ kHz. Readers are referred to Sec. 3.4 for details of the labels above the peaks.

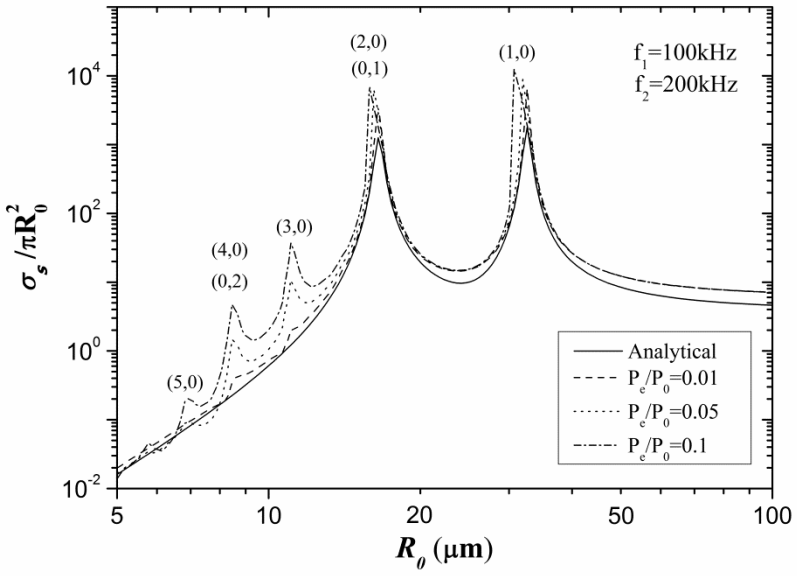

Figure 3.4. Predictions of acoustical scattering cross section versus equilibrium bubble radius under dual-frequency acoustic excitation by the analytical solution (solid line) and the numerical method with $P_e/P_0 = 0.01$ (dashed line), 0.05 (dotted line), 0.1 (dash-dotted line) respectively. $f_1 = 100$ kHz. $f_2 = 200$ kHz. $N = P_{A2}/P_{A1} = 1$. The two numbers with brackets above the peaks stand for (*a*,*b*). Readers are referred to Sec. 3.4 for details.

3.4 Nonlinear characteristics of the scattering cross section under dual-frequency acoustic excitation

Figure 3.5 shows the predicted scattering cross section curves under single-frequency excitation ($f_s = 100$ kHz) with different acoustic pressure amplitudes. The expressions n/m (here, m and n are two integers) marked above the peaks of the curves are the orders of the resonances. For details of the definitions of resonances, readers are referred to Sec. 1.3.1, Lauterborn (1976) and Lauterborn and Kurz (2010). For a certain value of P_e, the value of the scattering cross section reaches a maximum when the bubble radius is equal to the resonant bubble radius corresponding to the driving frequency, i.e., at the main resonance. The scattering cross section curves show nonlinear features, such as harmonic, subharmonic (e.g., the cases with $P_e/P_0 \geq 0.3$) and ultraharmonic (e.g., the case with $P_e/P_0 = 0.7$) resonances. With the increase of P_e, both the harmonic and subharmonic resonances grow significantly, and the peaks of those resonances bend toward smaller bubble radii. This “bending phenomenon” is a nonlinear feature determined by Keller-Miksis equation in Sec. 2.1. In contrast, the values of the scattering cross section in the regions above resonance do not increase with P_e. Unlike harmonics, the appearances of the subharmonics and ultraharmonics have clear thresholds

of acoustic pressure amplitude.

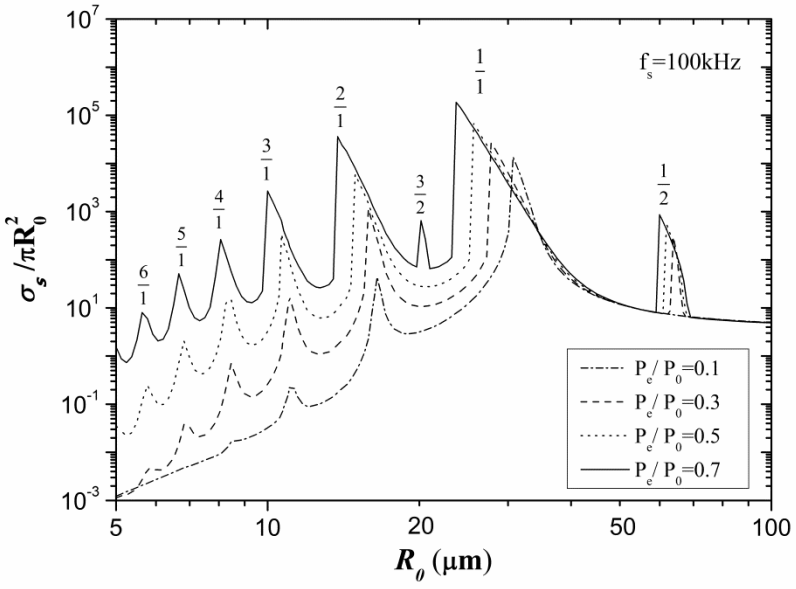

Figure 3.5 Acoustical scattering cross section versus equilibrium bubble radius under single-frequency acoustic excitation with $P_e/P_0 = 0.1$ (dash-dotted line), 0.3 (dashed line), 0.5 (dotted line) and 0.7 (solid line) respectively. $f_s = 100$ kHz. The numbers above the peaks represent the orders of the resonances: main resonance ($\frac{1}{1}$), harmonics ($\frac{2}{1}$, $\frac{3}{1}$,…), subharmonic ($\frac{1}{2}$) and ultraharmonic ($\frac{3}{2}$).

Figure 3.6 compares the scattering cross section curves under single-frequency and dual-frequency excitation (N=1) with acoustic pressure amplitude $P_e/P_0 = 0.3$. The two numbers within the brackets, i.e., (a,b), marked above the peaks, represent the resonance corresponding to the frequency $f = af_1 + bf_2$. According to the values of a and b, the peaks can be classified into following categories:

a) Main resonance, i.e., (1,0), (0,1).

b) Harmonics, e.g., (a,0), (0,b). a,b=1,2,….

c) Subharmonics, e.g., $\left(\frac{1}{2},0\right)$, $\left(0,\frac{1}{2}\right)$.

d) Combination resonances, e.g., (1,1), (-1,1) and subharmonic combination resonance, e.g., $\left(\frac{1}{2},\frac{1}{2}\right)$ as shown in Figure 3.7. The existence of the combination resonances is one of the unique features of the dual-frequency approach.

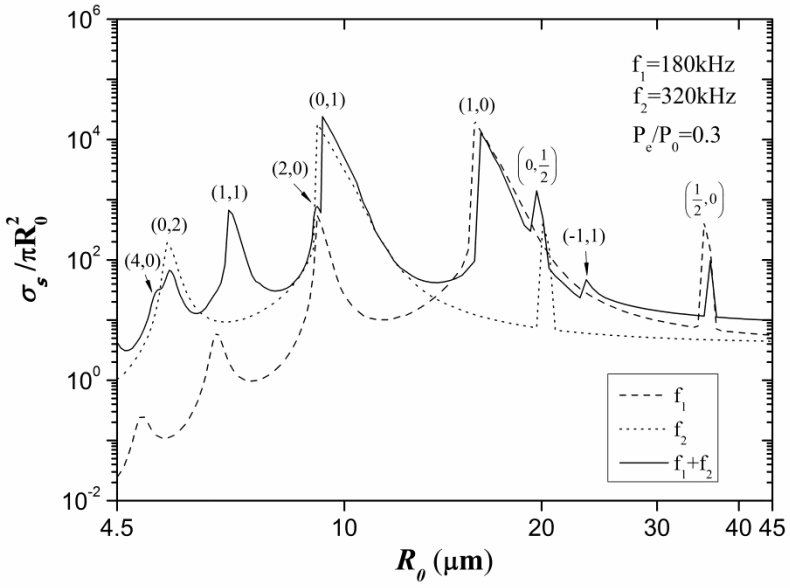

Figure 3.6 Acoustical scattering cross section under single-frequency [marked as " f_1 " (dashed line) and " f_2 " (dotted line)] and dual-frequency [marked as " $f_1 + f_2$ " (solid line)] acoustic excitation. $f_1 = 180$ kHz. $f_2 = 320$ kHz. $P_e / P_0 = 0.3$. $N = P_{A2} / P_{A1} = 1$. The two numbers with brackets above the peaks stand for (*a*,*b*).

Therefore, compared to the single-frequency approach, the dual-frequency approach can generate more resonance regions involving all the main, harmonic and subharmonic resonances corresponding to the two component frequencies respectively and a number of combination resonances. As shown in Figure 3.6, the signal strengths in terms of the amplitude of σ_s under dual-frequency excitation are much stronger than those under single-frequency excitation within a wide range of bubble

radii.

Sometimes, the bubble radii corresponding to the two resonances are quite close, leading to the merging of the resonances. For example, the frequency corresponding to the first harmonic [marked as (2,0) in Figure 3.6] of the acoustic wave f_1 is 360 kHz, which is quite close to the main resonance [marked as (0,1) in Figure 3.6] of the acoustic wave f_2 (320 kHz). Hence, the two resonances merge into one peak. Resonances (1,0) and $\left(0,\frac{1}{2}\right)$ also show the tendency of merging.

3.5 Influential parameters on scattering cross section

In this section, the influence of several parameters of the dual-frequency approach, e.g., the acoustic pressure amplitude, the energy allocation between two frequencies (*N*) and the ratio of the two frequencies (f_2/f_1), on the scattering cross section is numerically investigated.

Figure 3.7 illustrates the scattering cross section curves under dual-frequency excitation with different acoustic pressure amplitudes (P_e). As with the single-frequency approach, the main resonances, the harmonics and subharmonics all increase with the increase of P_e. And

they lean over towards smaller bubble radii at higher acoustic pressure amplitudes. Furthermore, the amplitude of the combination resonances [e.g., resonances marked as (1,1) and (-1,1) in Figure 3.7] increase significantly with the increase of P_e. The width of the resonances is also growing with the increase of P_e, leading to the merging of the resonances. For instance, in the case with $P_e/P_0 = 0.4$, resonance $\left(0, \frac{1}{2}\right)$ merges into resonance (1,0) while resonance (0,1) merges with the resonance (2,0) as well.

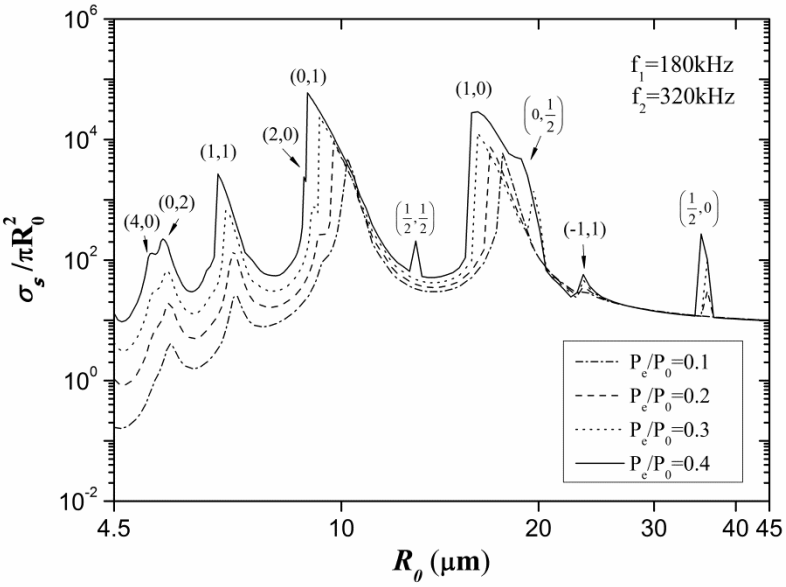

Figure 3.7 Acoustical scattering cross section versus equilibrium bubble radius under dual-frequency acoustic excitation with $P_e/P_0 = 0.1$ (dash-dotted line), 0.2 (dash line), 0.3 (dotted line) and 0.4 (solid line) respectively. $f_1 = 180$ kHz. $f_2 = 320$ kHz. $N = P_{A2}/P_{A1} = 1$. The two numbers with brackets above the peaks stand for (*a*,*b*).

The energy allocation between the two component waves, indicated by *N*, can also affect the scattering cross section. Figure 3.8 shows the predictions of the scattering cross section curves under single-frequency and dual-frequency acoustic excitation with different *N*. For N <1, as *N* decreases, the peaks of the main resonance (0,1) become much lower and narrower, while those of main resonance (1,0) almost remain the same as those under single-frequency excitation with frequency f_1. For N >1, with the increasing *N*, the peaks of main resonance (1,0) become much lower and narrower, while those of main resonance (0,1) almost remain the same as those under single-frequency excitation with the frequency f_2. Furthermore, *N* influences the values of the scattering cross section near subharmonics in the same way, i.e., the more energy allocated to one of the component frequencies, the lower the peaks of main resonance and subharmonics of the other component frequency, and *vice versa*. However, for combination resonances [e.g., (1,1) and (-1,1)], the maximum values of scattering cross section are obtained in the case with $N = 1$. The influence of *N* on harmonics is much more complicated. Nevertheless, for N <1, the values of scattering cross section near the harmonics [e.g., (0,2), (2,0), (3,0)] decrease with decreasing *N* while they do not differ much when $N \geq 1$. So generally speaking, $N \approx 1$ could generate a relatively high value of scattering cross section within the whole range of R_0.

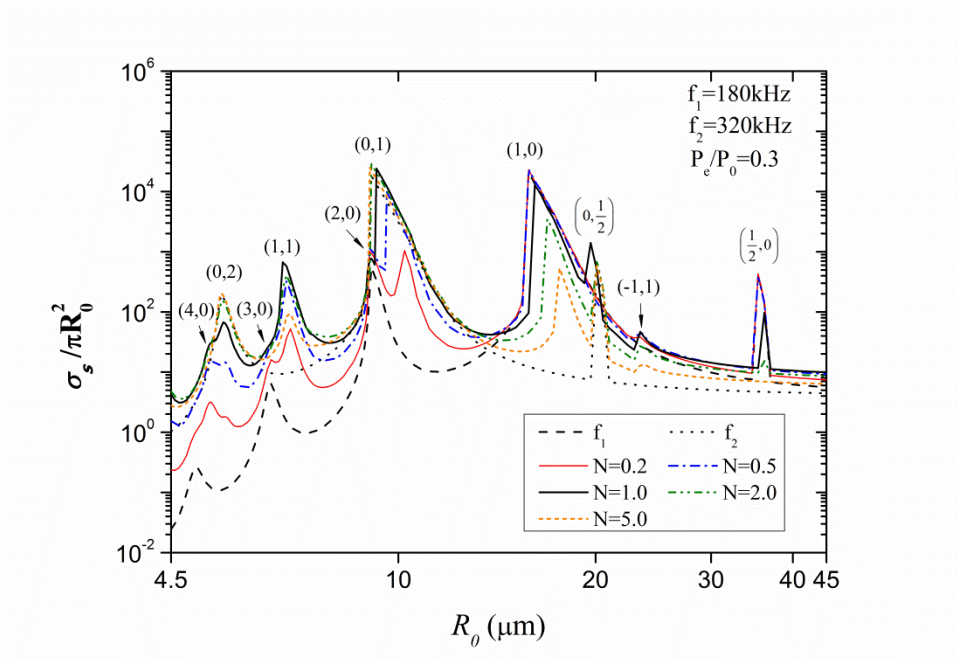

Figure 3.8 The predictions of acoustical scattering cross section under single-frequency [marked as " f_1 " (dash line) and " f_2 " (dotted line)] and dual-frequency [marked as " $f_1 + f_2$ " with different N] acoustic excitation. $f_1 = 180$ kHz. $f_2 = 320$ kHz. $N = P_{A2}/P_{A1} =$ 0.2, 0.5, 1, 2, 5 respectively. The two numbers with brackets above the peaks stand for (a,b).

The influence of the ratio of frequencies is indicated in Figure 3.9, in which f_1 is 100 kHz and f_2 is 160 kHz, 200 kHz and 300 kHz respectively. Obviously, f_2/f_1 would influence the positions of the resonances. Particularly, the "distance" between the two main resonances increases with the increase of f_2/f_1. Meanwhile, the values of scattering cross section in the region between the two resonances decreases with the increase of f_2/f_1. With increasing f_2/f_1 but fixing f_1, the values of scattering cross section increase in the region below the main resonance of f_2, decrease in the region between two main resonances, and nearly keep constant above the main resonance of f_1.

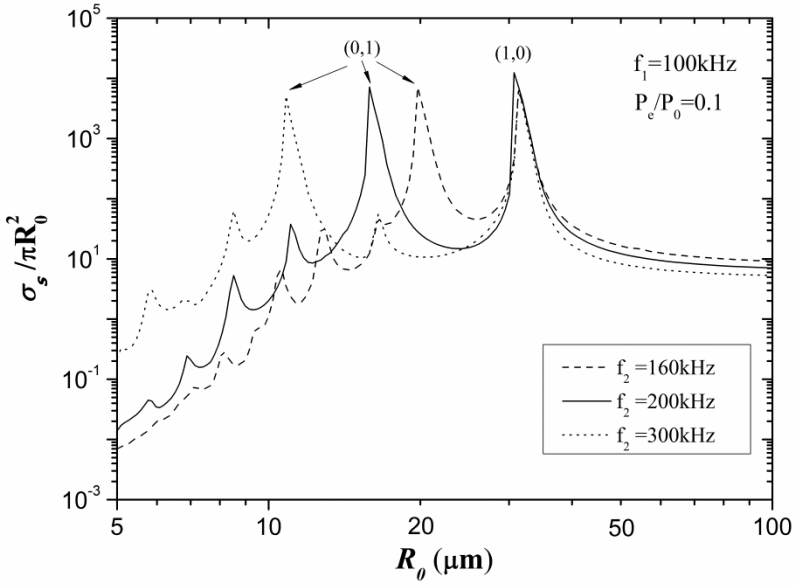

Figure 3.9 Acoustical scattering cross section versus equilibrium bubble radius under dual-frequency acoustic excitation with $f_1 = 100$ kHz and $f_2 = 160$ kHz (dashed line), 200 kHz (solid line), 300 kHz (dotted line) respectively. $P_e / P_0 = 0.1$. $N = P_{A2} / P_{A1} = 1$. The two numbers with bracket above the peaks indicated the main resonances.

3.6 Summary

In this chapter, both the analytical and numerical solutions of acoustical scattering cross section of gas bubbles under dual-frequency excitation are obtained. It is assumed that the bubble oscillates spherically symmetrically in a Newtonian fluid (i.e., water). Only radial motion of the bubble is considered. And vapour pressure in the bubble is omitted. The predictions of the values of scattering cross section by the analytical method agree well with the numerical simulations at low acoustic pressure amplitudes for both single-frequency excitation and dual-frequency excitation. However, the validity of the analytical solution will be violated when the acoustic pressure amplitude increases because many nonlinear features (e.g., bending phenomenon, harmonics, subharmonics, and ultraharmonics) will be present.

The nonlinear characteristics of the scattering cross section curve under dual-frequency excitation are investigated numerically. Generally, the scattering cross section curves show typical nonlinear features such as harmonics, subharmonics and ultraharmonics. Furthermore, the dual-frequency approach displays more resonances termed as “combination resonances”. Compared to the single-frequency approach, the dual-frequency approach could enhance the acoustical scattering cross

section significantly within a much broader range of bubble sizes due to the generation of more resonances.

The influence of several essential parameters in the dual-frequency system on the prediction of scattering cross section has been discussed. With the increase of the pressure amplitude, all amplitudes of resonances increase and the peaks of resonances lean over towards smaller bubble radii. The energy allocated between the two frequencies (i.e., *N*) and the ratio of the two component frequencies (i.e., f_2/f_1) can also affect the scattering cross section. The driving frequency affects the positions of the resonances. According to these results, for an effective enhancement of scattering cross section, the energy allocated to the two component frequencies should be almost equal and the ratio of two frequencies should be relatively large.

Chapter 4 The Secondary Bjerknes Force under Dual-Frequency Excitation

In this chapter, the characteristics of the secondary Bjerknes force under dual-frequency excitation are investigated. Parts of this chapter have been submitted as a journal paper (Zhang and Li, 2015, under review)

The chapter is organized as follows: in Sec. 4.1, the basic equations are introduced and the corresponding analytical solution is obtained; in Sec. 4.2, the results calculated from the analytical and numerical solutions are compared, together with the discussions of the valid region of the analytical solution; in Sec. 4.3, the basic features of the secondary Bjerknes force under dual-frequency excitation are investigated based on the numerical simulations; in Sec. 4.4, the influence of pressure amplitude is discussed. In this chapter, it is assumed that bubbles oscillate spherically symmetrically in a Newtonian fluid (i.e., water). Only radial motion of bubbles is considered. For solving the equations of bubble motion, the translational motion of bubbles is not taken into consideration. And vapour pressure in the bubble is omitted.

4.1 Equations and solutions

In this section, the basic equations for calculating the secondary Bjerknes force under dual-frequency excitation are introduced. Then, the analytical solution and the numerical simulation for solving these equations are given.

4.1.1 Basic equations

Here, the mutual interaction force (e.g., the secondary Bjerknes force) between two oscillating bubbles (numbered as “bubble 1” and “bubble 2” respectively) in liquids under the dual-frequency acoustic excitation is considered. According to the literature (e.g., Mettin et al., 1997), the radiation pressure generated by bubble 2 at the centre of bubble 1 (p_{rad1}) or *vice versa* (p_{rad2}) can be expressed as

$$p_{rad1} = \frac{\rho_l}{L}\frac{d}{dt}\left(\dot{R}_2 R_2^2\right), \tag{4.1}$$

$$p_{rad2} = \frac{\rho_l}{L}\frac{d}{dt}\left(\dot{R}_1 R_1^2\right). \tag{4.2}$$

Here, p_{rad1} is the radiation pressure generated by the oscillations of bubble 2 at the centre of bubble 1; p_{rad2} is the radiation pressure generated by the oscillations of bubble 1 at the centre of bubble 2; ρ_l is the density of the liquid; L is the separation distance between the centres of the two bubbles; t is the time; R_1 and R_2 are the instantaneous bubble radii of bubbles 1 and 2 respectively; overdot denotes the time derivative.

Then, with involving the radiation pressure generated by other bubbles, the equations of bubble motion [i.e., Eqs. (2.1)-(2.4)] for two interacting bubbles should be (Mettin et al., 1997, Eq. 7)

$$\left(1-\frac{\dot{R}_1}{c_l}\right)R_1\ddot{R}_1+\frac{3}{2}\left(1-\frac{\dot{R}_1}{3c_l}\right)\dot{R}_1^2=\left(1+\frac{\dot{R}_1}{c_l}\right)\frac{p_1(R_1,t)-p_s(t)}{\rho_l}$$
$$+\frac{R_1}{\rho_l c_l}\frac{d[p_1(R_1,t)-p_s(t)]}{dt}-\frac{1}{L}\frac{d}{dt}\left(\dot{R}_2R_2^2\right), \quad (4.3)$$

$$\left(1-\frac{\dot{R}_2}{c_l}\right)R_2\ddot{R}_2+\frac{3}{2}\left(1-\frac{\dot{R}_2}{3c_l}\right)\dot{R}_2^2=\left(1+\frac{\dot{R}_2}{c_l}\right)\frac{p_2(R_2,t)-p_s(t)}{\rho_l}$$
$$+\frac{R_2}{\rho_l c_l}\frac{d[p_2(R_2,t)-p_s(t)]}{dt}-\frac{1}{L}\frac{d}{dt}\left(\dot{R}_1R_1^2\right), \quad (4.4)$$

where

$$p_1(R_1,t)=\left(P_0+\frac{2\sigma}{R_{01}}\right)\left(R_{01}/R_1\right)^{3\kappa}-\frac{2\sigma}{R_1}-\frac{4\left(\mu_l+\mu_{th}\right)}{R_1}\dot{R}_1; \quad (4.5)$$

$$p_2(R_2,t)=\left(P_0+\frac{2\sigma}{R_{02}}\right)\left(R_{02}/R_2\right)^{3\kappa}-\frac{2\sigma}{R_2}-\frac{4\left(\mu_l+\mu_{th}\right)}{R_2}\dot{R}_2; \quad (4.6)$$

$$p_s(t)=P_0\left(1+\varepsilon_1e^{i\omega_1t}+\varepsilon_2e^{i\omega_2t}\right). \quad (4.7)$$

Here, c_l is the undisturbed speed of sound in the liquid; P_0 is the ambient pressure; ρ_l is the density of the liquid; σ is the surface tension coefficient; R_{01} and R_{02} are the equilibrium bubble radii of bubbles 1 and 2 respectively; κ is the polytropic exponent; μ_l is the viscosity of the liquid; μ_{th} is effective thermal viscosity; ε_1 and ε_2 are

the non-dimensional amplitudes of the driving sound wave; ω_1 and ω_2 are the angular frequencies of the driving sound waves.

4.1.2 Analytical solutions

In this section, a traditional perturbation method is employed to solve the equations in Sec. 4.1.1. For details of solving procedure, readers are referred to Doinikov (1999) and Zhang and Du (2015). The framework of Zhang and Du (2015) has been extended to investigate the secondary Bjerknes force under dual-frequency excitation. Here, for convenience, most of the nomenclatures in Zhang and Du (2015) are adopted.

We assume the solutions of Eqs. (4.3) and (4.4) as

$$R_1 = R_{01}(1+x_1), \tag{4.8}$$

$$R_2 = R_{02}(1+x_2). \tag{4.9}$$

Then based on Eqs. (4.3) and (4.4), one can obtain

$$\ddot{x}_1 + 2\beta_1\dot{x}_1 + \omega_{01}^2 x_1 + \frac{R_{02}^2}{R_{01}^2}\xi_2\ddot{x}_2 = -\frac{\alpha_1}{M_1}\left(N_{11}\varepsilon_1 e^{i\omega_1 t} + N_{12}\varepsilon_2 e^{i\omega_2 t}\right), \tag{4.10}$$

$$\ddot{x}_2 + 2\beta_2\dot{x}_2 + \omega_{02}^2 x_2 + \frac{R_{01}^2}{R_{02}^2}\xi_1\ddot{x}_1 = -\frac{\alpha_2}{M_2}\left(N_{21}\varepsilon_1 e^{i\omega_1 t} + N_{22}\varepsilon_2 e^{i\omega_2 t}\right), \tag{4.11}$$

where

$$\omega_{0j}^2 = \frac{1}{M_j\rho_l R_{0j}^2}\left[3\kappa\left(P_0 + \frac{2\sigma}{R_{0j}}\right) - \frac{2\sigma}{R_{0j}}\right], \tag{4.12}$$

$$\beta_j = \beta_{vj} + \beta_{thj} + \beta_{acj} = \frac{2\left(\mu_l + \mu_{th}\right)}{\rho_l R_{0j}^2 M_j} + \frac{R_{0j}}{2c_l}\omega_{0j}^2, \tag{4.13}$$

$$\xi_j = \frac{R_{0j}}{L}, \tag{4.14}$$

$$\alpha_j = \frac{P_0}{\rho_l R_{0j}^2}, \tag{4.15}$$

$$M_j = 1 + \frac{R_{0j}}{c_l}\frac{4\mu_l}{\rho_l R_{0j}^2}, \tag{4.16}$$

$$N_{jk} = 1 + \frac{\omega_k R_{0j}}{c_l} i. \tag{4.17}$$

Here, j =1, 2; k =1, 2; ω_{0j} is the natural frequency of the bubble j; β_j, β_{vj}, β_{thj} and β_{acj} are the total, viscous, thermal and acoustic damping constants of the bubble j respectively. In this section, as only linear oscillations of bubbles (up to the first order of ε) are considered, the solution of x_1 and x_2 can be expressed as

$$x_1 = A_{11}e^{i\omega_1 t} + A_{12}e^{i\omega_2 t}, \tag{4.18}$$

$$x_2 = A_{21}e^{i\omega_1 t} + A_{22}e^{i\omega_2 t}. \tag{4.19}$$

Then with substituting Eqs. (4.18) and (4.19) into Eqs. (4.10) and (4.11), one can obtain

$$\left(\omega_{01}^2 - \omega_1^2 + 2\beta_1\omega_1 i\right)A_{11} - \frac{R_{02}^2}{R_{01}^2}\xi_2\omega_1^2 A_{21} = -\frac{\alpha_1}{M_1}N_{11}\varepsilon_1 e^{i\omega_1 t}, \tag{4.20}$$

$$\left(\omega_{02}^2 - \omega_1^2 + 2\beta_2\omega_1 i\right)A_{21} - \frac{R_{01}^2}{R_{02}^2}\xi_1\omega_1^2 A_{11} = -\frac{\alpha_2}{M_2}N_{21}\varepsilon_1 e^{i\omega_1 t}, \tag{4.21}$$

$$\left(\omega_{01}^2 - \omega_2^2 + 2\beta_1\omega_2 i\right)A_{12} - \frac{R_{02}^2}{R_{01}^2}\xi_2\omega_2^2 A_{22} = -\frac{\alpha_1}{M_1}N_{12}\varepsilon_2 e^{i\omega_2 t}, \tag{4.22}$$

$$\left(\omega_{02}^2-\omega_2^2+2\beta_2\omega_2 i\right)A_{22}-\frac{R_{01}^2}{R_{02}^2}\xi_1\omega_2^2A_{12}=-\frac{\alpha_2}{M_2}N_{22}\varepsilon_2 e^{i\omega_2 t}. \tag{4.23}$$

By solving Eqs. (4.20)-(4.23), we got

$$A_{11}=-\frac{\alpha_1\varepsilon_1}{X_1}\left[\frac{N_{21}}{M_2}\xi_2\omega_1^2+\frac{N_{11}}{M_1}\left(\omega_{02}^2-\omega_1^2+2\beta_2\omega_1 i\right)\right], \tag{4.24}$$

$$A_{21}=-\frac{\alpha_2\varepsilon_1}{X_1}\left[\frac{N_{11}}{M_1}\xi_1\omega_1^2+\frac{N_{21}}{M_2}\left(\omega_{01}^2-\omega_1^2+2\beta_1\omega_1 i\right)\right], \tag{4.25}$$

with

$$X_1=\left(\omega_{01}^2-\omega_1^2+2\beta_1\omega_1 i\right)\left(\omega_{02}^2-\omega_1^2+2\beta_2\omega_1 i\right)-\xi_1\xi_2\omega_1^4. \tag{4.26}$$

and

$$A_{12}=-\frac{\alpha_1\varepsilon_2}{X_2}\left[\frac{N_{22}}{M_2}\xi_2\omega_2^2+\frac{N_{12}}{M_1}\left(\omega_{02}^2-\omega_2^2+2\beta_2\omega_2 i\right)\right], \tag{4.27}$$

$$A_{22}=-\frac{\alpha_2\varepsilon_2}{X_2}\left[\frac{N_{12}}{M_1}\xi_1\omega_2^2+\frac{N_{22}}{M_2}\left(\omega_{01}^2-\omega_2^2+2\beta_1\omega_2 i\right)\right], \tag{4.28}$$

with

$$X_2=\left(\omega_{01}^2-\omega_2^2+2\beta_1\omega_2 i\right)\left(\omega_{02}^2-\omega_2^2+2\beta_2\omega_2 i\right)-\xi_1\xi_2\omega_2^4. \tag{4.29}$$

As the secondary Bjerknes force is a mutual interaction between two interacting bubbles, only the force on bubble 1 needs to be determined [Eqs. (4.37) and (4.38) prove rigorously that the force on bubble 2 has the same value and opposite direction in the same coordinate system]. The secondary Bjerknes force is defined as (Bjerknes, 1906)

$$F_B=-\left\langle v_1\nabla p_2\right\rangle, \tag{4.30}$$

with

$$v_1 = \frac{4}{3}\pi R_1^3, \tag{4.31}$$

$$\nabla p_2 = \frac{\rho_l}{L^2}\frac{d}{dt}\left(\dot{R}_2 R_2^2\right)\boldsymbol{e_{12}}. \tag{4.32}$$

Here, F_B denotes the secondary Bjerknes force; v_1 is the instantaneous volume of the bubble 1; ∇p_2 is the pressure gradient generated by bubble 2 at the centre of bubble 1; $\langle\ \rangle$ denotes the time average during one oscillation period; $\boldsymbol{e_{12}}$ is the unit vector pointing from bubble 1 to bubble 2. Here, following the framework of Doinikov (1999), one can define $v_1 = \mathrm{Im}(V_1)$ and $\nabla p_2 = \mathrm{Im}(\nabla P_2)$. For linear cases, Eqs. (4.31) and (4.32) can be represented as

$$V_1 = V_C + V_{11} + V_{12} \approx \frac{4}{3}\pi R_{01}^3\left(1 + 3A_{11}e^{i\omega_1 t} + 3A_{12}e^{i\omega_2 t}\right), \tag{4.33}$$

$$\nabla P_2 = \nabla P_{21} + \nabla P_{22} \approx \frac{\rho_l}{L^2}R_{02}^3\ddot{x}_2\boldsymbol{e}_{12} = -\frac{\rho_l}{L^2}R_{02}^3\left(\omega_1^2 A_{21}e^{i\omega_1 t} + \omega_2^2 A_{22}e^{i\omega_2 t}\right)\boldsymbol{e_{12}}. \tag{4.34}$$

In Eq. (4.33), as V_C is a constant, $\langle V_C \nabla P_2 \rangle = 0$ and this term will not contribute to the secondary Bjerknes force. Then after time averaging, $\left\langle e^{2i\omega_1 t}\right\rangle = 0$ and $\left\langle e^{2i\omega_2 t}\right\rangle = 0$. The secondary Bjerknes force can be expressed as

$$F_B = -\frac{1}{2}\mathrm{Re}\left(\bar{V}_{11}\nabla P_{21} + \bar{V}_{12}\nabla P_{22}\right). \tag{4.35}$$

Here, a bar over the symbol denotes the complex conjugate. By substituting Eqs. (4.33) and (4.34) into Eq. (4.35), the final expression of

the secondary Bjerknes force under dual-frequency excitation is obtained as

$$F_B = 2\pi\rho_l R_{01}^2 R_{02}^2 \xi_1 \xi_2 \left[\omega_1^2 \,\mathrm{Re}\left(\bar{A}_{11} A_{21}\right) + \omega_2^2 \,\mathrm{Re}\left(\bar{A}_{12} A_{22}\right) \right]. \qquad (4.36)$$

Hence, up to the second order of ε_1 (or ε_2), based on Eq. (4.36), the secondary Bjerknes force under dual-frequency approach can be considered as the linear combination of those under the two component single-frequency approaches. With the generations of harmonics, the solution will be very complex, causing problems for physical interpretation. For details, readers are referred to Doinikov (1999).

4.1.3 Numerical simulations

Substituting Eqs. (4.31) and Eqs. (4.32) into Eq. (4.30), one can obtain

$$F_B = -\left\langle v_1 \nabla p_2 \right\rangle = -\left\langle v_1 \frac{\rho_l}{L^2} \frac{d}{dt}\left(\dot{R}_2 R_2^2\right) \right\rangle \boldsymbol{e_{12}} = -\left\langle \frac{\rho_l}{4\pi L^2} v_1 \frac{d^2 v_2}{dt^2} \right\rangle \boldsymbol{e_{12}}. \qquad (4.37)$$

Integrating Eq. (4.37) over a period of the volume oscillations, one can obtain the formula for the secondary Bjerknes force,

$$F_B = -\frac{\rho_l}{4\pi L^2} \left\langle \dot{v}_1 \dot{v}_2 \right\rangle \boldsymbol{e_{12}}, \qquad (4.38)$$

where

$$\dot{v}_1 = 4\pi R_1^2 \dot{R}_1, \qquad (4.39)$$

$$\dot{v}_2 = 4\pi R_2^2 \dot{R}_2. \qquad (4.40)$$

For numerical simulations, Eqs. (4.3) and (4.4) are solved by an explicit Runge-Kutta formula (Dormond and Prince, 1980). Then Eqs. (4.38)-(4.40) are employed to obtain the secondary Bjerknes force. Based on Eq. (4.38), the distance (i.e., L) does not affect the direction of the Bjerknes force, so the results are represented by the secondary Bjerknes force coefficient (Mettin et al., 1997)

$$f_B = \frac{\rho_l}{4\pi}\langle \dot{v}_1 \dot{v}_2 \rangle . \tag{4.41}$$

Therefore, if $f_B > 0$, the bubbles attract each other; if $f_B < 0$, the bubbles repulse each other.

The corresponding resonant bubble radii of the driving frequencies are calculated based on Eq. (4.12), and are represented as R_{rs} (single-frequency approach) and R_{r1} and R_{r2} (dual-frequency approach). The constants employed in analytical and numerical methods are: σ =0.0725 N/m; c_l =1486 m/s; $\kappa = 1.4$. And other constants are listed in Appendix A. The distance between the centres of the bubbles is $L = 1\times10^{-3}$ m. For comparison, the total input power, $P_e/P_0 = \left(\varepsilon_1^2 + \varepsilon_2^2\right)^{1/2}$, remains constant in both the single-frequency excitation and dual-frequency excitation cases.

4.2 Comparison between the analytical solution and the numerical simulations

In this section, the predictions by the analytical solution [Eq. (4.36)] are compared with those predicted by the numerical simulation to illustrate the validity of the analytical solution.

For comparison, the equilibrium radius of bubble 1 is fixed ($R_{01} = 10$ μm) and the variations of f_B with the change of the radius of bubble 2 are calculated. Figures 4.1 and 4.2 show the curves of f_B predicted by the analytical and numerical approaches under the single-frequency excitation ($f_s = 100$ kHz) and the dual-frequency excitation ($f_1 = 100$ kHz and $f_2 = 200$ kHz) respectively. The resonance bubble radii corresponding to the driving frequencies are marked in the figures as R_{rs}, R_{r1} and R_{r2}.

As shown in Figure 4.1, for single-frequency excitation, the value of f_B reaches maximum when $R_{02} \approx R_{rs}$. Then the sign of f_B changes from positive to negative at $R_{02} \approx R_{rs}$, which can also be concluded from the well-known formula (Bjerknes, 1906; Doinikov, 1999):

$$F_B = \frac{2\pi |A|^2 \omega^2 R_{01} R_{02}}{\rho L^2 (\omega_{01}^2 - \omega^2)(\omega_{02}^2 - \omega^2)}. \tag{4.42}$$

where ω_{01} and ω_{02} are the natural frequencies of bubble 1 and bubble 2 respectively.

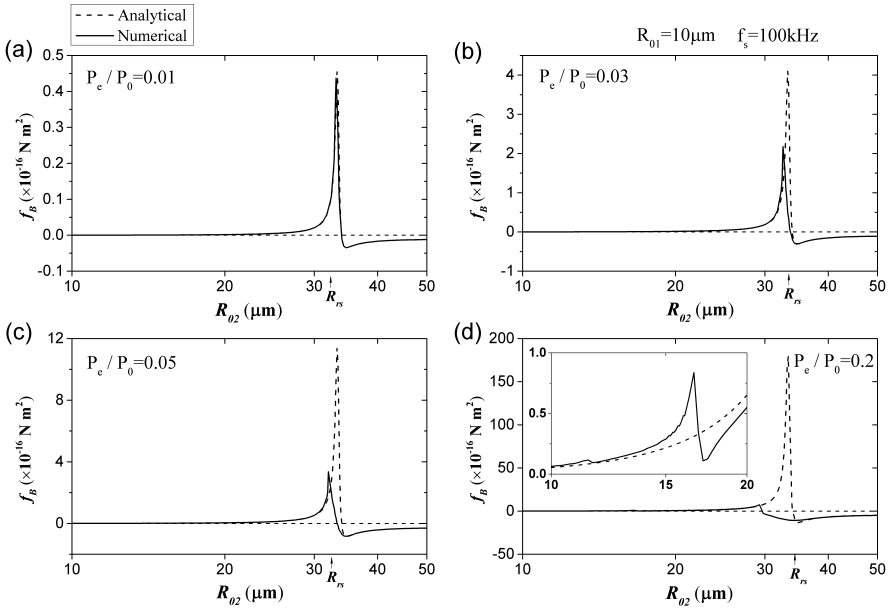

Figure 4.1 Predictions of the secondary Bjerknes force coefficient f_B versus the equilibrium radius of bubble 2 under single-frequency excitation by the analytical solution (dashed line) and the numerical simulations (solid line). (a) $P_e/P_0 = 0.01$. (b) $P_e/P_0 = 0.03$. (c) $P_e/P_0 = 0.05$. (d) $P_e/P_0 = 0.2$. The subplot in (d) shows the magnification of f_B for R_{02} between 10 μm and 20 μm. $f_s = 100$ kHz. $R_{01} = 10$ μm. R_{rs} corresponds to the resonance radius of the driving frequency. The horizontal line indicates where $f_B = 0$.

Therefore, according to Eq. (4.42), if the driving frequency lies between the two linear resonance frequencies (i.e., $R_{01} < R_{rs} < R_{02}$ or $R_{02} < R_{rs} < R_{01}$), the bubbles repulse each other; otherwise (i.e., "$R_{rs} < R_{01}$ and $R_{rs} < R_{02}$" or "$R_{01} < R_{rs}$ and $R_{02} < R_{rs}$") they attract each other.

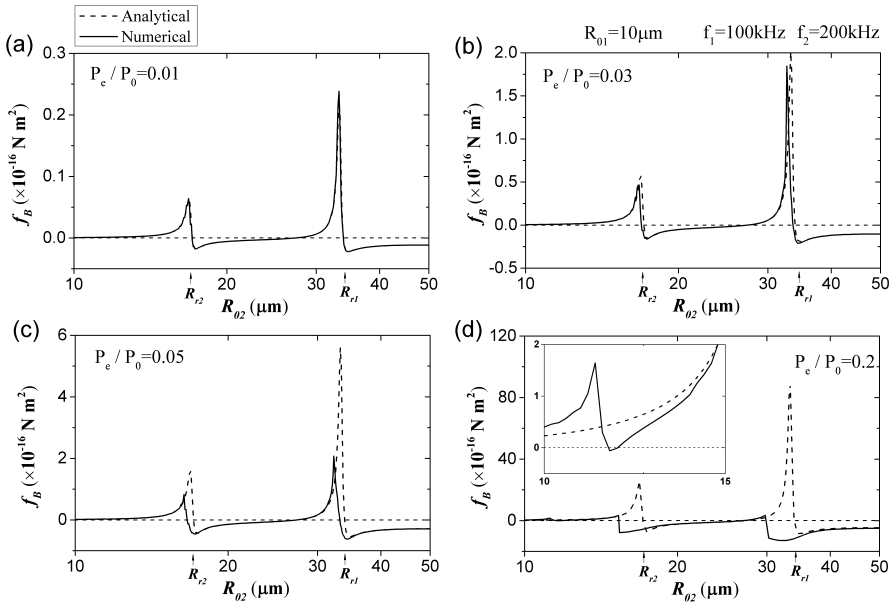

Figure 4.2 Predictions of the secondary Bjerknes force coefficient f_B versus the equilibrium radius of bubble 2 under dual-frequency excitation by the analytical solution (dashed line) and the numerical simulations (solid line). (a) $P_e/P_0 = 0.01$. (b) $P_e/P_0 = 0.03$. (c) $P_e/P_0 = 0.05$. (d) $P_e/P_0 = 0.2$. The subplot in (d) shows the magnification of f_B for R_{02} between 10 μm and 15 μm. $f_1 = 100$ kHz. $f_2 = 200$ kHz. $R_{01} = 10$ μm. R_{r1} and R_{r2} indicate the corresponding resonance radii of the driving frequencies respectively. The horizontal line indicates $f_B = 0$.

The curves under the dual-frequency excitation in Figure 4.2 show two peaks at $R_{02} \approx R_{r2}$ and $R_{02} \approx R_{r1}$ respectively. The characteristics of the secondary Bjerknes force under dual-frequency excitation will be discussed in detail in Sec. 4.3. When the acoustic pressure is low [as

shown in Figures 4.1(a) and 4.2(a)], e.g., $P_e/P_0 = 0.01$, the analytical solution and the numerical simulation agree well under both single- and dual-frequency excitation. With increasing values of P_e, the values of f_B near resonances increase dramatically. The values of f_B near resonances predicted by the analytical solution are higher than those predicted by the numerical simulation and the difference between the two approaches increases with increasing P_e. The positions of the peaks of the curves predicted by the numerical simulation move towards smaller bubble radii. The influence of the acoustical pressure will be discussed in Sec. 4.4. When P_e/P_0 is up to 0.2, as the subplot in Figure 4.1(d) shows, another peak appears at the resonance radius corresponding to $2f_s$ (the first harmonic, see Sec. 4.3 for details) in the numerical approach. Similarly, in the subplot in Figure 4.2(d), a peak appears at the resonance radius corresponding to $f_1 + f_2$ (the combination resonance, see Sec. 4.3 for details) in the numerical approach. The analytical approach fails to predict these phenomena. Therefore, the analytical solution is only valid when the pressure amplitude is low.

4.3 The basic features of the secondary Bjerknes force under dual-frequency excitation

In this section, a numerical approach is employed to study the characteristics of the secondary Bjerknes force. The basic features of the secondary Bjerknes force under dual-frequency excitation are investigated. For comparison, the predictions of the secondary Bjerknes force under single-frequency excitation are also shown.

Figure 4.3 shows the variation of the secondary Bjerknes force coefficient f_B in the $R_{01} - R_{02}$ plane under low sound pressure amplitude ($P_e/P_0 = 0.03$). The repulsive forces (i.e., $f_B < 0$) are represented by red areas while the attractive forces (i.e., $f_B > 0$) are represented by grey scales. The darker the colour is, the higher the absolute value of f_B is.

Figures 4.3(a) and 4.3(b) are the predictions of f_B under single-frequency excitation ($f_s = 100$ kHz and $f_s = 200$ kHz respectively). As shown in these figures, there are four regions in $R_{01} - R_{02}$ planes, divided by the "boundaries" corresponding to the resonance radius of the driving frequency (for a simpler description, the

equilibrium radius of the bigger bubble is represented as $R_{0\max}$ and the equilibrium radius of the smaller bubble is represented as $R_{0\min}$):

a) Repulsive regions ($f_B < 0$): $R_{0\min} < R_{rs} < R_{0\max}$.

b) Attractive regions ($f_B > 0$): $R_{rs} < R_{0\min} < R_{0\max}$.

Figure 4.3(c) shows the f_B between two bubbles under the dual-frequency excitation ($f_1 = 100$ kHz and $f_2 = 200$ kHz). Divided by the resonance bubble radii corresponding to the component driving frequencies, there are nine regions in the $R_{01} - R_{02}$ plane, which could be classified into three categories:

a) Repulsive regions ($f_B < 0$): $R_{0\min} < R_{r2} < R_{r1} < R_{0\max}$.

b) Attractive regions ($f_B > 0$): $R_{r2} < R_{r1} < R_{0\min} < R_{0\max}$;

$R_{r2} < R_{0\min} < R_{0\max} < R_{r1}$; $R_{0\min} < R_{0\max} < R_{r2} < R_{r1}$.

c) Uncertain regions (where f_B could be positive or negative):

$R_{0\min} < R_{r2} < R_{0\max} < R_{r1}$; $R_{r2} < R_{0\min} < R_{r1} < R_{0\max}$.

This classification could also be explained by Eq. (4.36). In regions a) and b), the values of f_B under the two component single-frequency excitation have the same sign. According to Eq. (4.36), the values of f_B under the dual-frequency excitation can be considered as a linear combination of the values of f_B under the two component single-frequency excitation if the value of P_e is limited. Hence, in

regions a) and b), the sign of f_B remains unchanged under dual-frequency excitation. In region c), f_B could be enforced or suppressed by adding the second acoustic excitation, leading to the sign change, which depends on the relative values of f_B the secondary Bjerknes force corresponding to the two component frequencies.

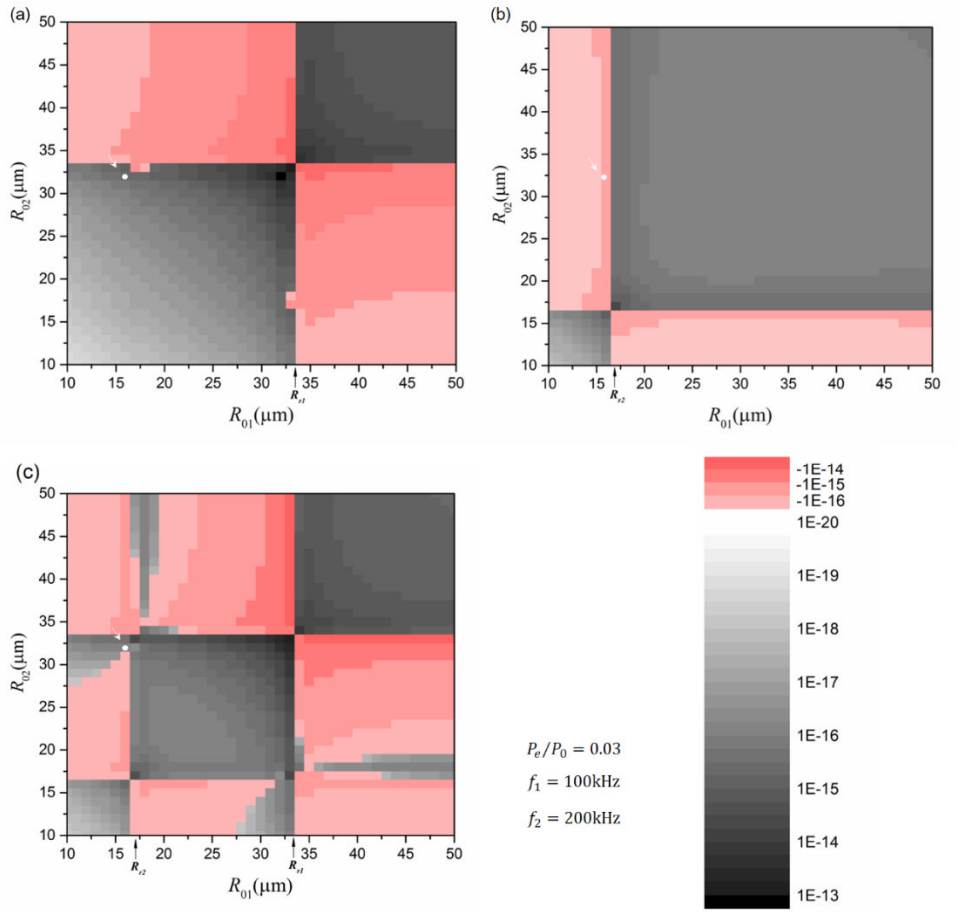

Figure 4.3 The variations of the secondary Bjerknes force coefficient f_B in the $R_{01} - R_{02}$ plane under single-frequency [$f_s = 100$ kHz (a), $f_s = 200$ kHz (b)] and dual-frequency [$f_1 = 100$ kHz and $f_2 = 200$ kHz (c)] excitation. $P_e / P_0 = 0.03$. R_{r1} and R_{r2} indicate the corresponding resonance radii of the driving frequencies respectively. The repulsive forces (i.e., $f_B < 0$) are represented by red areas while the attractive forces (i.e., $f_B > 0$) are represented by grey scales. The scale bars are located at the bottom right corner. The white points and the arrows indicate the two-bubble system with $R_{01} = 16$ μm and $R_{02} = 32$ μm.

For further illustration, the values of f_B versus the equilibrium radius of bubble 2 (R_{02}) is shown in Figure 4.4 for three typical cases: $R_{01} < R_{r2} < R_{r1}$ ($R_{01} = 10$ μm), $R_{r2} < R_{01} < R_{r1}$ ($R_{01} = 25$ μm) and $R_{r2} < R_{r1} < R_{01}$ ($R_{01} = 40$ μm). For the cases under single-frequency excitation, the absolute values of f_B rise significantly near the resonance. Furthermore, the sign of f_B would change near the resonance. For dual-frequency excitation, there are peaks near both resonance bubble radii corresponding to the two frequencies, which means that the sign of f_B may change two or three times in the full range of R_{02} (10-50 μm). Moreover, in the region away from the resonance radius, the values of f_B under dual-frequency excitation are between the corresponding values of f_B under two component single-frequency excitation. However, the positions of the peaks of dual-frequency approach are slightly different from the positions of single–frequency approach. Taking the case where $R_{01} = 10$ μm [Figure 4.4(a)] as an example. When $R_{02} < R_{r2} < R_{r1}$, all the f_B under single- and dual-frequency excitation are positive, corresponding to the "attractive regions" in Figure 4.3. When $R_{02} > R_{r1} > R_{r2}$, all the f_B under single and dual-frequency excitation are negative, corresponding to the "repulsive regions" in Figure 4.3. When $R_{r2} < R_{02} < R_{r1}$, f_B in the low-frequency approach (100 kHz) is positive while f_B in the high-frequency approach (200 kHz) is negative.

Therefore, f_B under the dual-frequency excitation varies from negative to positive, corresponding to the "uncertain regions" in Figure 4.3(c).

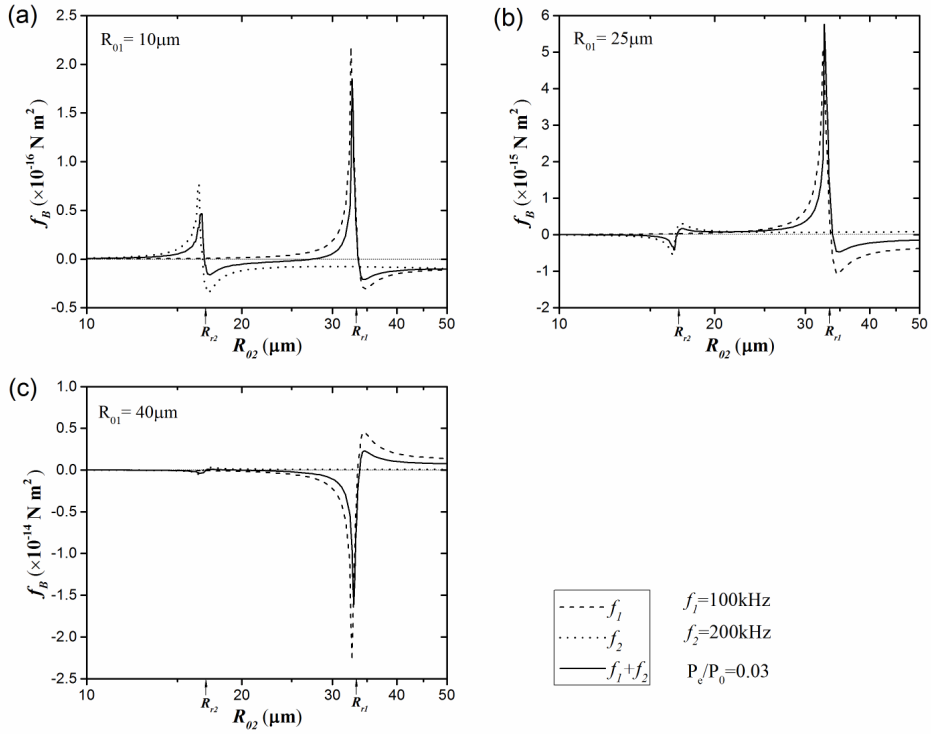

Figure 4.4 The variations of the secondary Bjerknes force coefficient f_B versus equilibrium bubble radius of bubble 2 when the radius of bubble 1 is fixed as: (a) $R_{01}=10$ μm, (b) $R_{01}=25$ μm, (c) $R_{01}=40$ μm. The bubbles are driven by single-frequency [$f_s=100$ kHz (dashed line), $f_s=200$ kHz (dotted line)] and dual-frequency [$f_1=100$ kHz and $f_2=200$ kHz (solid line)] excitation respectively. $P_e/P_0=0.03$. The horizontal line indicates $f_B=0$.

When the pressure amplitude is higher, the influence of the nonlinearity will be important. Figure 4.5 shows the variations of f_B in the $R_{01}-R_{02}$

plane under a relatively high sound pressure amplitude ($P_e/P_0 = 0.3$). Here, the driving frequencies are 100 kHz and 150 kHz respectively. Comparing these results with the cases under the low pressure amplitude, there are still boundaries near the resonances radii corresponding to the driving frequencies. Furthermore, new peaks of f_B and new "repulsive regions" appear in the original "attractive regions". These phenomena are marked by white circles in Figure 4.5. They can also be classified as below:

a) Harmonics (marked by solid lines) occur near the corresponding resonance radii corresponding to the frequency nf_1 or mf_2, where n=2,3 and m=2 in Figure 4.5.

b) Subharmonics (marked by dashed lines) occur near the resonance radii corresponding to the frequency f_1/n or f_2/m. Limited by the range of the bubble radii, only the subharmonic of the high frequency component (150 kHz) is shown. In Figure 4.5 (b) and (c), m = 2.

c) Combination resonances (marked by the dash dotted line) occur near the resonance radii corresponding to the frequency $nf_1 + mf_2$. In Figure 4.5(c), n=m=1.

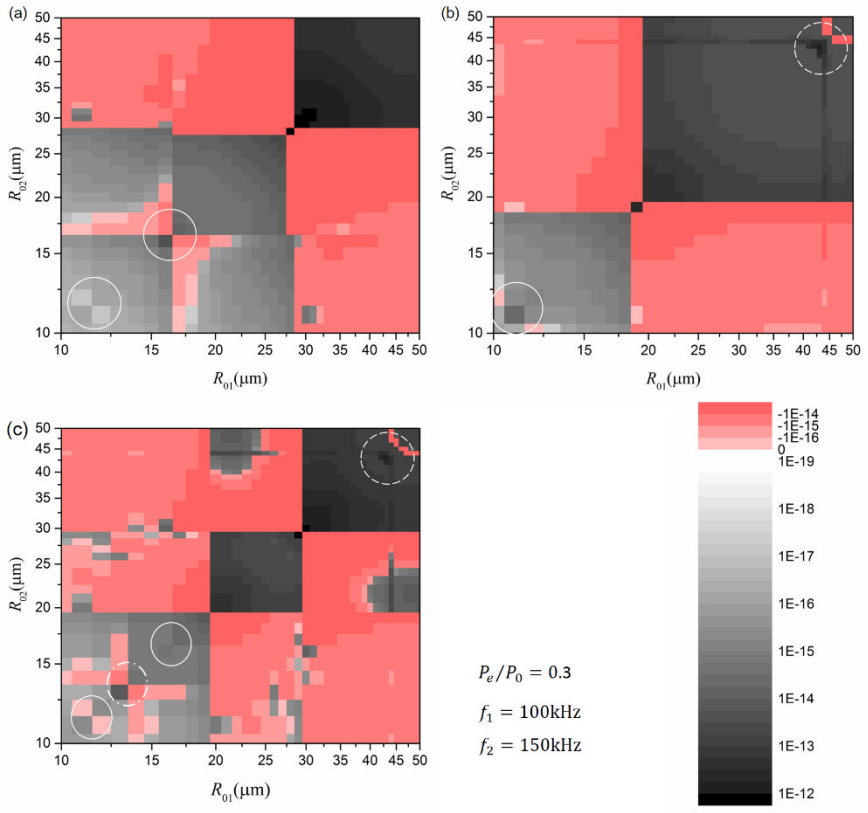

Figure 4.5 The variations of the secondary Bjerknes force coefficient f_B in the $R_{01} - R_{02}$ plane under single-frequency [$f_s = 100$ kHz (a), $f_s = 150$ kHz (b)] and dual-frequency [$f_1 = 100$ kHz and $f_2 = 150$ kHz (c)] excitation. $P_e/P_0 = 0.3$. The repulsive forces (i.e., $f_B < 0$) are represented by red areas while the attractive forces (i.e., $f_B > 0$) are represented by grey scales. The scale bars are located at the bottom right corner. The resonances marked with white circles are harmonics (solid line), subharmonics (dashed line) and combination resonance (dash-dotted line).

Like the main resonances, there are peaks of f_B near the harmonics, subharmonics and combination resonances. And the sign of f_B changes when the bubble radius cross over these resonance radii. In particular, for harmonics of higher order [i.e., the second harmonic in Figure 4.5(a)], only a peak of f_B appears while the sign of f_B does not change. Doinikov (Doinikov, 1999) derived an analytical solution of the secondary Bjerknes force by including the first harmonic of bubble oscillation under the single-frequency excitation [Doinikov, 1999, Eq. (37)]. If the second harmonic included, it will be

$$F_B = \left[F_1^{(1)} + F_1^{(2)} + F_1^{(3)} \right] \boldsymbol{e}_{12} . \tag{4.43}$$

Here, $F_1^{(1)}$ represents the force induced by the linear component of bubble oscillation, which is of order ε^2. $F_1^{(2)}$ represents the force induced by the first harmonic component of bubble oscillation, which is of order ε^4. $F_1^{(3)}$ represents the force induced by the second harmonic component of bubble oscillation, which is of order ε^6. Therefore, as shown in Figure 4.5, when $\varepsilon = P_e / P_0 = 0.3$, the effect of the first harmonic will become important and can change the value significantly as well as the sign of f_B. However, under this pressure, the effect of the second order harmonic is not strong enough, so it can only change the value of f_B but not the sign, as shown in Figure 4.5(a).

By comparing Figures 4.5(a) and 4.5(b) with 4.5(c), we can conclude that the secondary Bjerknes forces in the $R_{01} - R_{02}$ plane under dual-frequency excitation involve all the harmonics and subharmonics corresponding to the two component frequencies. Meanwhile, there are unique combination resonances in the $R_{01} - R_{02}$ plane under dual-frequency excitation. Therefore, the variation of the sign of f_B in the $R_{01} - R_{02}$ plane under the dual-frequency excitation shows much more complicated patterns.

4.4 Influence of the pressure amplitude

Oguz and Prosperetti (1990) investigated the interaction of two oscillating bubbles under the single-frequency excitation with the pressure amplitude below 0.5 bar. The nonlinear effects turn the secondary Bjerknes force to be repulsive in the case of the bubbles both driven below their resonance frequencies. However, according to the classical theory, the secondary Bjerknes force should be attractive in this region [referring to Eq. (4.42)]. Mettin et al. (1997) investigated the secondary Bjerknes force in very strong sound fields (pressure amplitude exceeding 1 bar) in the $R_{01} - R_{02}$ plane. The repulsion also appears when the bubbles both driven far below their resonance frequencies. And the repulsive zone changes with the pressure amplitude. In this section, the influence of the pressure amplitude

(P_e/P_0 is up to 0.2) on the secondary Bjerknes force under dual-frequency excitation is investigated numerically and compared with those under single-frequency excitation.

Figures 4.6 and 4.7 show the variations of the values of f_B in the $R_{01}-R_{02}$ planes with the total driving pressure amplitude P_e/P_0 equalling to 0.1 and 0.2 respectively. The driving frequencies are 100 kHz and 200 kHz. By comparing Figures 4.3, 4.6 and 4.7, one can conclude that the total pressure amplitude can influence the signs and the values of f_B. Obviously, the increasing pressure amplitude will increase the absolute value of f_B, leading to enforcement of the mutual interactions between bubbles. With the increase of the pressure amplitude, the boundaries of the regions move toward the smaller bubble radii, which is owing to the resonance frequencies of bubbles getting lower induced by the nonlinearity during bubble oscillation (termed as "bending phenomenon"). For the dual-frequency approach, the regions covered by the attractive and repulsive forces in the "uncertain regions" vary with the pressure amplitude as follows: the attractive region increases in regions $R_{r2} < R_{02} < R_{r1} < R_{01}$ and $R_{r2} < R_{01} < R_{r1} < R_{02}$ while it decreases in regions $R_{01} < R_{r2} < R_{02} < R_{r1}$ and $R_{02} < R_{r2} < R_{01} < R_{r1}$. Therefore, for the

bubbles with radii near the resonances, the sign of the forces between the bubbles will change with the increase of the pressure amplitude.

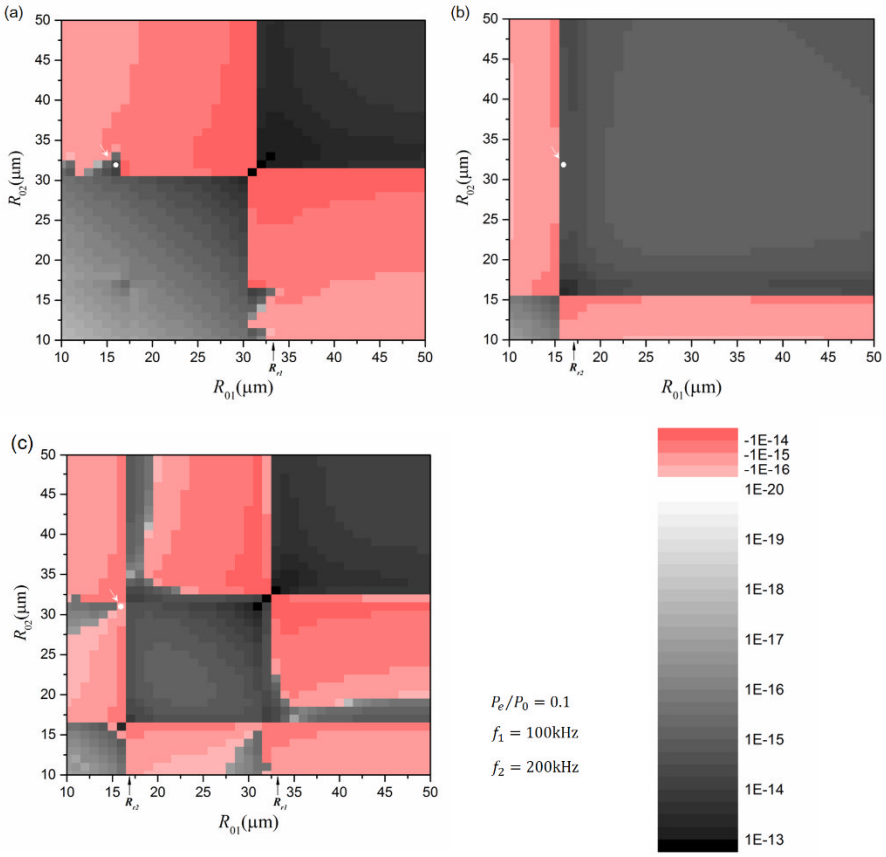

Figure 4.6 The variations of the secondary Bjerknes force coefficient f_B in the $R_{01} - R_{02}$ plane under single-frequency [$f_s = 100$ kHz (a), $f_s = 200$ kHz (b)] and dual-frequency [$f_1 = 100$ kHz and $f_2 = 200$ kHz (c)] excitation. $P_e/P_0 = 0.1$. R_{r1} and R_{r2} indicate the corresponding resonance radii of the driving frequencies respectively. The repulsive forces (i.e., $f_B < 0$) are represented by red areas while the attractive forces (i.e., $f_B > 0$) are represented by grey scales. The scale bars are located at the bottom right corner. The white points and the arrows indicate the two-bubble system with $R_{01} = 16$ μm and $R_{02} = 32$ μm.

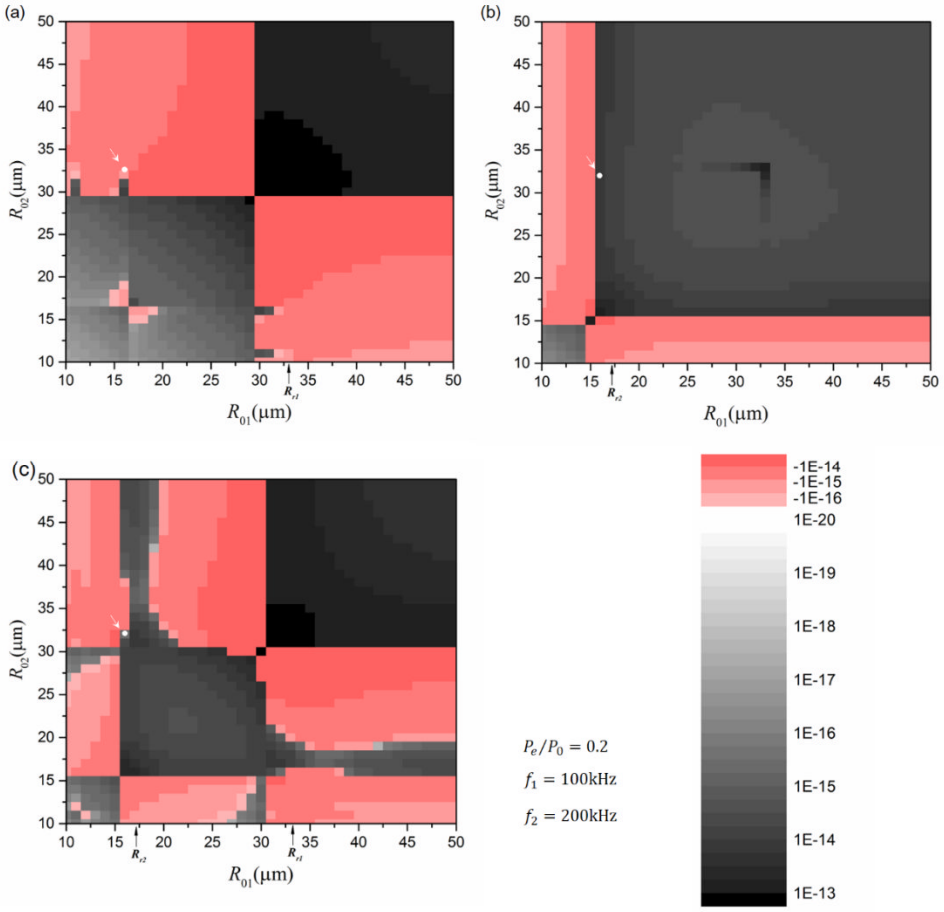

Figure 4.7 The variations of the secondary Bjerknes force coefficient f_B in the $R_{01} - R_{02}$ plane under single-frequency [$f_s = 100$ kHz (a), $f_s = 200$ kHz (b)] and dual-frequency [$f_1 = 100$ kHz and $f_2 = 200$ kHz (c)] excitation. $P_e/P_0 = 0.2$. R_{r1} and R_{r2} indicate the corresponding resonance radii of the driving frequencies respectively. The repulsive forces (i.e., $f_B < 0$) are represented by red areas while the attractive forces (i.e., $f_B > 0$) are represented by grey scales. The scale bars are located at the bottom right corner. The white points and the arrows indicate the two-bubble system with $R_{01} = 16$ μm and $R_{02} = 32$ μm.

The system with $R_{01} = 16$ μm and $R_{02} = 32$ μm is a typical example indicated by white points in Figures 4.3, 4.6 and 4.7, which could reveal the detailed influence of the added frequency in the dual-frequency approach and the amplitude of the acoustic pressure on the value of f_B. Figure 4.8 illustrates the variations of the value of f_B with the pressure amplitude. For the two-bubble system with $R_{01} = 10$ μm and $R_{02} = 14$ μm, which is away from the "boundaries", f_B is positive under both single- and dual-frequency excitation and increases with the pressure monotonically. In contrast, in the system with $R_{01} = 16$ μm and $R_{02} = 32$ μm, which is near the resonances, the sign of f_B changes with the pressure amplitude. For single-frequency excitation, the sign of f_B changes once at $P_e/P_0 = 0.19$ for excitation with driving frequency f_1 or at $P_e/P_0 = 0.08$ for excitation with driving frequency f_2. For dual-frequency excitation, the sign of f_B changes twice at $P_e/P_0 = 0.065$ and 0.18 respectively. In particular parameter zone, the values of f_B under the dual-frequency excitation are no longer between the values of the two single-frequency cases. Instead, in the region where P_e/P_0 is between 0.08 to 0.18, the values of f_B for the dual-frequency approach are negative while the values for the single-frequency approaches are all positive.

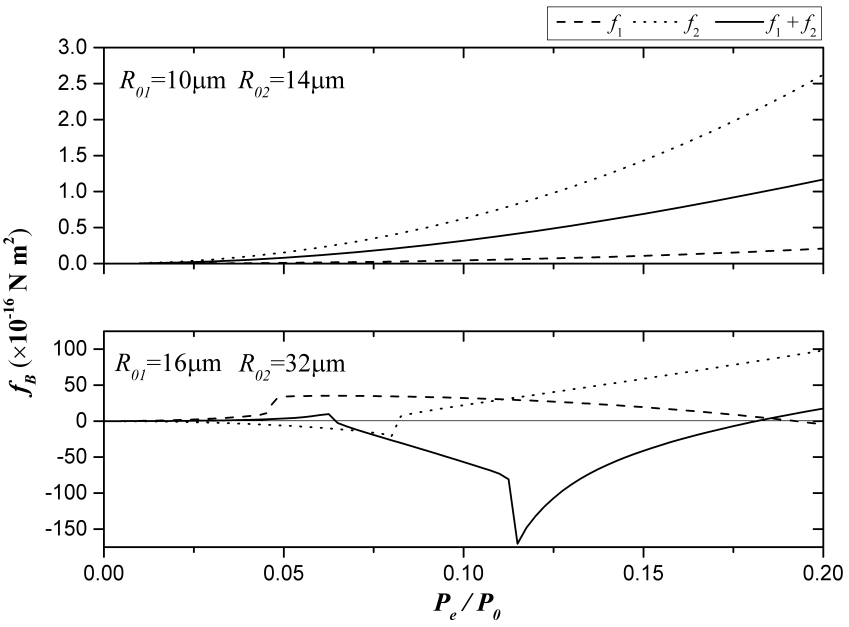

Figure 4.8 The variations of the secondary Bjerknes force coefficient f_B with the sound pressure amplitude P_e/P_0 under single-frequency [$f_s = 100$ kHz (dashed line), $f_s = 200$ kHz (dotted line)] and dual-frequency [$f_1 = 100$ kHz and $f_2 = 200$ kHz (solid line)] excitation. In the upper image, $R_{01} = 10$ μm and $R_{02} = 14$ μm. In the lower image, $R_{01} = 16$ μm and $R_{02} = 32$ μm. The horizontal line indicates where $f_B = 0$.

The differences between the single-frequency approach and the dual-frequency approach are illustrated in Figure 4.9. Figure 4.9(a) shows the variations of the pressure amplitude in one driving period. Figure 4.9(b) shows the oscillation curves of the bubbles in one driving period. In Figures 4.9 and 4.10, *T* equals to the period of the excitation with

$f_s = 100$ kHz, i.e., $T = 1 \times 10^{-5}$ s. Under the single-frequency excitation, the two bubbles oscillate in phase in most of the time. However, under the dual-frequency excitation, the two bubbles oscillate out of phase in most of the time. Therefore, the time average value of $\dot{v}_1 \dot{v}_2$ [as shown in Figure 4.9(c)] in one period is positive, leading to positive f_B under single-frequency excitation while it is negative, leading to negative f_B under the dual-frequency excitation.

For further study of the influence of the pressure amplitude on the bubbles with radii near the resonances, Figure 4.10 compares the bubble oscillations under dual-frequency excitation with different driving pressure amplitudes. As shown in Figure 4.10(a), when the pressure amplitude is low (e.g., $P_e / P_0 = 0.03$), the two bubbles oscillate in phase for the most of the time. As shown in Figure 4.10(b), the time average of $\dot{v}_1 \dot{v}_2$ yields positive f_B. With P_e / P_0 rising to 0.1, the oscillation phase of the bigger bubble ($R_{02} = 32$ μm) shifts while the oscillation phase of the smaller bubble ($R_{01} = 16$ μm) remains so that the two bubbles oscillate out of phase. When P_e / P_0 rises to 0.2, the phase of the bigger bubble remains the same while those of the smaller bubble shifts so that the two bubbles oscillate in phase again. Therefore, as shown in Figure

4.10(b), the time average value of $\dot{v}_1\dot{v}_2$ is negative, leading to negative f_B when $P_e/P_0 = 0.1$ and returns to positive f_B when $P_e/P_0 = 0.2$.

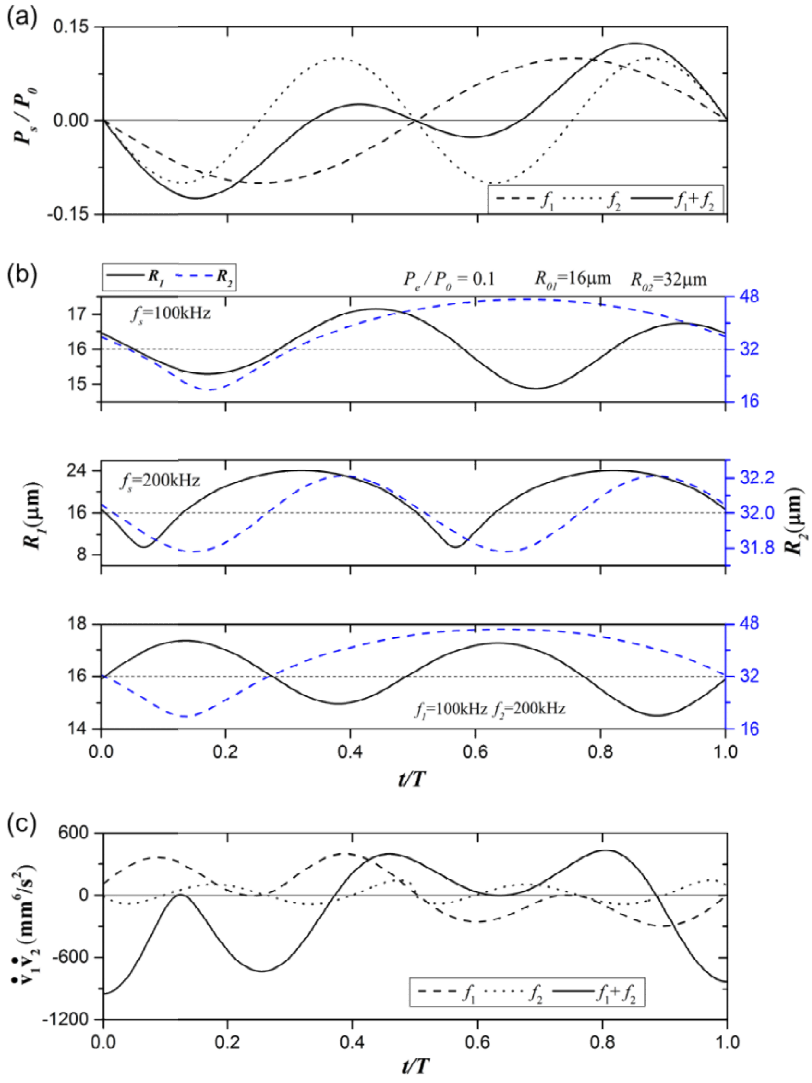

Figure 4.9 (a) Normalized driving pressure P_s/P_0 versus normalized time t/T. (b) The instantaneous bubble radii R_1 (black line) and R_2 (blue line) versus normalized time t/T during one driving period. (c) $\dot{v}_1\dot{v}_2$ versus normalized time. $P_e/P_0 = 0.1$. $R_{01} = 16$ μm. $R_{02} = 32$ μm. $f_1 = 100$ kHz and $f_2 = 200$ kHz. $T = 1/f_1$.

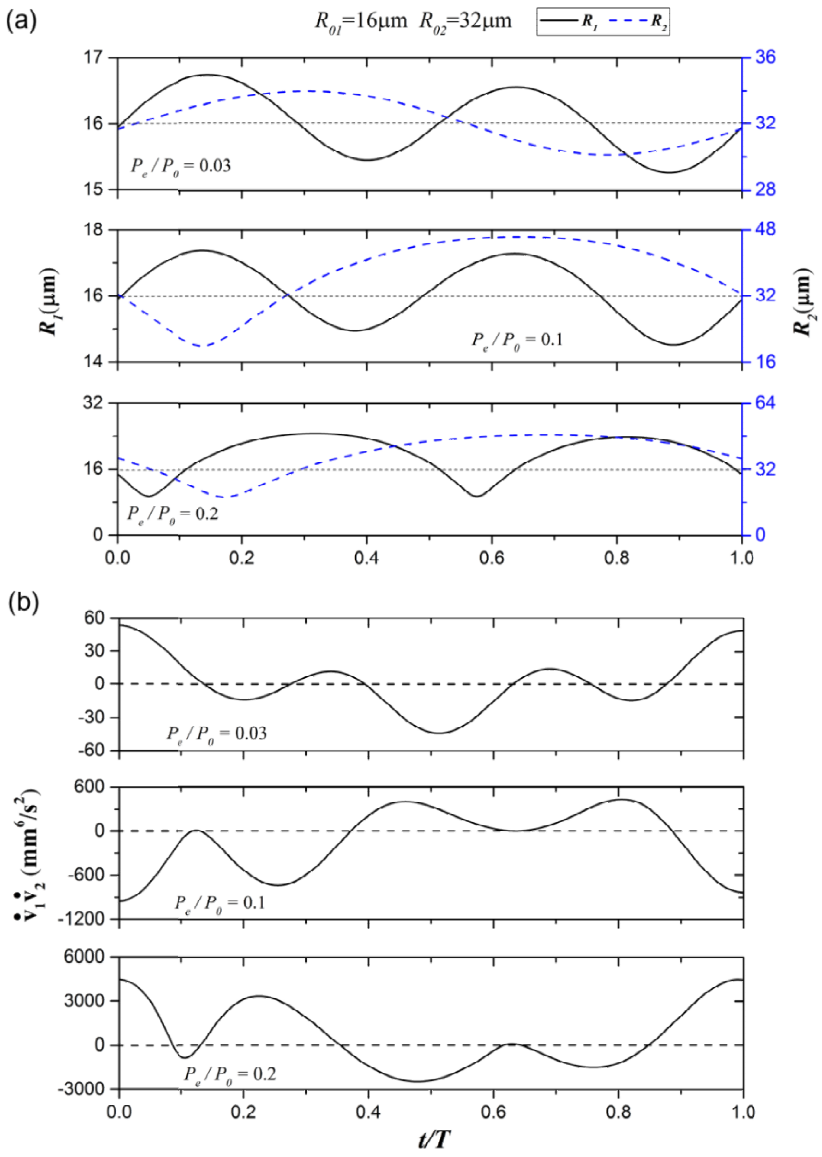

Figure 4.10 The bubble oscillations under dual-frequency excitation ($f_1 = 100$ kHz and $f_2 = 200$ kHz) with different pressure amplitudes. (a) The instantaneous bubble radii R_1 (black line) and R_2 (blue line) versus normalized time t/T during one driving period. (b) $\dot{v}_1\dot{v}_2$ versus normalized time. P_e/P_0 = 0.03, 0.1, and 0.2 respectively. $R_{01} = 16$ μm. $R_{02} = 32$ μm. $T = 1/f_1$.

4.5 Summary

In this chapter, both the analytical and numerical solutions of the secondary Bjerknes force between two gas bubbles under dual-frequency excitation are obtained. The primary assumptions are: the bubble oscillates spherically symmetrically in a Newtonian fluid (i.e., water); only radial motion of the bubble is considered; vapour pressure in the bubble is omitted. According to the analytical solution, when the amplitudes of the acoustic excitation are low ($P_e/P_0 \ll 1$), the secondary Bjerknes force under dual-frequency excitation can be considered as the linear combination of those under the two component single-frequency approaches. The analytical solution and the numerical simulation results agree well when the pressure amplitude is quite low, e.g., $P_e/P_0 = 0.01$.

The basic features of the secondary Bjerknes force under dual-frequency excitation are investigated numerically. There are peaks and change of the sign of the secondary Bjerknes force near the resonance bubble radii corresponding to the driving frequencies. For single-frequency excitation, the predicted values of f_B in the $R_{01} - R_{02}$ plane could be divided into four regions by the resonance radius corresponding to the driving frequency and the values of f_B can be categorized into two groups (i.e., attractive and repulsive regions). For dual-frequency excitation, the f_B in

the $R_{01} - R_{02}$ plane can be divided into nine regions by the resonance radii corresponding to the two component frequencies and the values of f_B can be categorized into three groups (i.e., attractive, repulsive and uncertain regions). When the pressure amplitude is relatively high, the harmonics and subharmonics become prominent in the $R_{01} - R_{02}$ plane under both single- and dual-frequency excitation. There are combination resonances in the $R_{01} - R_{02}$ plane under the dual-frequency excitation. All these resonances could lead to the change of the sign of the secondary Bjerknes force.

The pressure amplitude will influence the positions of boundaries of the regions in the $R_{01} - R_{02}$ plane. With the increase of the pressure amplitude, the boundaries lean over toward smaller bubble radii. And it will also affect both the values and the sign of the secondary Bjerknes force, especially for the cases with bubble radii close to the resonance radii. Under particular conditions, the secondary Bjerknes force under dual-frequency excitation is repulsive while the secondary Bjerknes forces under the two component single-frequency excitation are both attractive.

Chapter 5 Conclusions

5.1 Achievements

The dynamics of gas bubbles in liquids under dual-frequency acoustic excitation have been investigated with respect to the fundamental characteristics of bubble oscillations, acoustical scattering cross section and the secondary Bjerknes force. In the numerical study, it is assumed that the bubble oscillates spherically symmetrically in a Newtonian fluid (i.e., water). Only radial motion of bubbles is considered. And the vapour pressure in the bubble is omitted.

The results from this PhD research programme show that under dual-frequency excitation, the traditional resonances (e.g., the main, harmonic, subharmonic, and ultraharmonic resonances corresponding to the two component sound waves) observed under single-frequency excitation are all present. Besides these resonances, there are some new resonances (named as “combination resonances” and “simultaneous resonances”) observed in the bubble dynamics under dual-frequency excitation, leading to much complex phenomena. The frequencies corresponding to the combination resonances can be expressed by the

linear combination of the two component frequencies. Compared with the single-frequency excitation, the oscillation amplitude of bubbles and the acoustical scattering cross section are enhanced by the addition of the second sound wave in particular parameter zones, owing to the existence of more resonances (e.g., a lot of combination resonances) under the dual-frequency excitation.

The analytical solutions of acoustical scattering cross section of gas bubbles and the secondary Bjerknes force between two interacting gas bubbles under dual-frequency excitation are obtained. The predictions of the values of scattering cross section and the secondary Bjerknes force by the analytical method agree well with the numerical simulations for the cases with low acoustic pressure amplitudes ($P_e/P_0 \ll 1$). According to the analytical solution, the secondary Bjerknes force under dual-frequency excitation can be considered as the linear combination of those under the two component single-frequency approaches.

The values of the secondary Bjerknes force under dual-frequency excitation are evaluated and plotted in the $R_{01} - R_{02}$ plane numerically. The secondary Bjerknes force in the $R_{01} - R_{02}$ plane can be divided into nine regions by the resonance radii corresponding to the two component

frequencies and the nature of the secondary Bjerknes force can be thus categorized into three groups (i.e., attractive, repulsive and uncertain zones). Compared with the single-frequency excitation, the sign of the secondary Bjerknes force in the $R_{01} - R_{02}$ plane varies in a more complicated pattern under dual-frequency excitation.

It has also been shown from this PhD programme that a number of parameters (e.g., the pressure amplitude, the equilibrium bubble radii, the power allocation between the component waves, the phase difference and the driving frequency) can influence the bubble dynamics under dual-frequency excitation, which has been fully discussed in this thesis with demonstrating examples.

5.2 Future work

1. In this thesis, the polytropic exponent in Eq. (2.2) was assumed as a constant (i.e., κ =1.4 or 1.33). Furthermore, we also assumed that the thermal damping can be ignored (i.e., $\mu_{th} = 0$). These assumptions were adopted because no rigorous model is available in the literature by now for the predictions of the polytropic exponent and thermal damping of oscillations of the bubbles excited by dual-frequency acoustic excitation. For these thermal effects, under single-frequency

excitation, the theoretical model for predicting κ and μ_{th} is well-known. According to theoretical works (Devin, 1959; Prosperetti, 1977; Zhang and Li, 2010; Zhang, 2013b) and experimental data (Crum, 1983), the values of polytropic exponent (κ) and effective thermal viscosity (μ_{th}) depends on many physical parameters (e.g., frequency of acoustic wave and bubble radius).

In Appendix B, influence of the thermal effects (i.e., the predictions of κ and μ_{th}) on the nonlinear oscillations of gas bubbles (e.g., the main, harmonic, subharmonic and ultraharmonic resonances) under single-frequency excitation are investigated based on the framework of Propseretti (1977). And the predictions of simplified model with a constant value of κ and $\mu_{th} = 0$ are also given for comparison. It can be concluded that the basic findings obtained in this thesis will not be impaired by employing the simplified models of thermal effects. Furthermore, a more advanced model of thermal effects (if available in the future) can be easily incorporated into the present work.

2. In this thesis, most of the investigations are focused on the bubble oscillations excited by small or medium acoustical pressure amplitude, termed as “stable cavitation” (Neppiras, 1980). During this process, mass transfer through rectified diffusion across bubble interfaces plays

a key role on the bubble behaviour (Plesset and Prosperetti, 1977; Neppiras, 1980; Crum, 1984; Zhang and Li, 2014b), which may affect the acoustical cross section and the values of the Bjerknes force through changing the equilibrium bubble radius. In Appendix C, the characteristics of the mass transfer across bubble interfaces under dual-frequency excitation have been investigated. A criterion based on bubble growth regions for optimizing the parameters of dual-frequency approach is proposed. In particular, the influence of the power allocation and the frequency ratio between two component acoustic waves on the bubble growth is discussed. In the future, more effort will be made on the topic of the mass transfer across bubble interfaces under dual-frequency excitation, for instance, the rate and the time of the bubble growth under the dual-frequency excitation, which are the primary parameters concerned in the sonochemistry and ultrasound enhanced biomedical techniques.

3. In this thesis, only Newtonian fluid (i.e., water) is considered. When cavitation is applied in the field of biomedicine (e.g., ultrasound enhanced drug delivery, tissue ablation, and ultrasound diagnosis), bubbles are usually surrounded by tissue or body fluid, which are viscoelastic liquids (Mollica et al., 2007). Acoustic cavitation is also

an effective way to degas the alloy, by accumulating gas in the melt (Eskin, 2001). Multi-frequency acoustic approach could also promote the effects of cavitation in these fields (Zheng et al., 2005; Barati et al., 2007; Guo et al., 2013). The property of the liquid will affect bubble behaviour significantly. For example, the amplitude of bubble oscillation could be enhanced by a viscoelastic liquid, compared to the Newtonian liquid (Allen and Roy, 2000). For recent reviews of the bubble dynamics in the non-Newtonian liquid, readers are referred to Brujan (2010) and Allen and Roy (1998). Therefore, in future, the effects of the non-Newtonian fluid on the bubble dynamics under dual-frequency excitation should be considered, which are indispensable for deepening the theoretical understanding and improving the practical applications of dual-frequency approach.

Appendix A: Constants used for calculations

If not specified, the following values for air and water are used for calculations in Chapters 2-4 and Appendix B and C: density of the liquid ρ_l =998.20 kg/m^3; viscosity of the liquid μ_l =1.0 mPa s; effective thermal viscosity $\mu_{th} = 0$; surface tension coefficient σ =0.0728 N/m; speed of sound in the liquid c_l =1486 m/s; ambient pressure P_0 =101300 Pa; polytrophic exponent $\kappa = 1.33$.

Appendix B: Influence of Thermal Effects on the Nonlinear Radial Oscillations of Gas Bubbles in Liquids under Single-Frequency Acoustic Excitation

This Appendix focuses on the influence of the values of the polytropic exponent and the effective thermal viscosity on the nonlinear oscillations (e.g., harmonics, subharmonics and ultraharmonics) of gas bubbles in liquids under single-frequency acoustic excitation. Parts of this Appendix have been published as a journal paper (Zhang and Li, 2014a).

In the literature, the polytropic exponent (κ) is usually assumed to be a constant, such as 1.0 (Eller, 1969), 1.33 (Lauterborn, 1976) and 1.4 (Eller, 1972; Yang and Church, 2005; Collin and Coussios, 2011; Webb et al., 2011). Additionally, the thermal damping is usually ignored (i.e., $\mu_{th} = 0$). However, according to a more advanced model (Prosperetti, 1977), the

polytropic exponent varies significantly with the bubble radii and acoustic driving frequencies. Hence, in this appendix, Prosperetti's model (Prosperetti, 1977) is employed to calculate the polytropic exponent and the effective thermal viscosity. Then their effects on the nonlinear oscillations of bubbles are discussed. For comparison, the predictions of the bubble behaviour based on the approaches employing a constant polytropic exponent (i.e., $\kappa = 1.0$ and 1.4, respectively) and ignoring thermal dissipation (i.e., $\mu_{th} = 0$) are also shown. Thus, the influence of thermal effects (i.e., values of the polytropic exponent and the effective thermal viscosity) on the nonlinear radial oscillations of gas bubbles under single-frequency excitation in the liquids is quantitatively evaluated.

The equation of bubble motion is the equation developed by Keller and Miksis (1980) [Eqs. (2.1)-(2.3)]. To close the model, μ_{th} and κ in Eq. (2.2) can be solved following the framework of Prosperetti (1977). The formulas of μ_{th} and κ are (Prosperetti, 1977; Zhang, 2013b):

$$\mu_{th} = \frac{1}{4}\omega\rho_g R_0^2 \,\mathrm{Im}\,\varphi, \tag{B1}$$

$$\kappa = \frac{\omega^2 \rho_g R_0^2 \,\mathrm{Re}\,\varphi}{3\left(P_0 + 2\sigma / R_0\right)}, \tag{B2}$$

with

$$\varphi = \frac{\Gamma_1 - \Gamma_2}{\lambda_1 \Gamma_2 - \lambda_2 \Gamma_1}, \tag{B3}$$

$$\lambda_i = \beta_i \coth \beta_i - 1 \quad i=1,2\,, \tag{B4}$$

$$\beta_1 = (1+i)\left(\frac{1}{2}\gamma G_2\right)^{1/2}\left\{1+\frac{1}{2}i\left[(\gamma-1)/\gamma\right]G_1 + O(G_1^2)\right\}, \tag{B5}$$

$$\beta_2 = \left(G_1 G_2\right)^{1/2}\left\{i+\frac{1}{2}\left[(\gamma-1)/\gamma\right]G_1 + O(G_1^2)\right\}, \tag{B6}$$

$$\Gamma_1 = 2\left(i + G_1/\gamma\right) + O(G_1^2)\,, \tag{B7}$$

$$\Gamma_2 = 2\left(\gamma-1\right)G_1\left[1+iG_1/\gamma\right]/\gamma + O\left(G_1^3\right), \tag{B8}$$

$$G_1 = M_g D_{g,v}\omega/\gamma R_g T_\infty\,, \tag{B9}$$

$$G_2 = \omega R_0^2 / D_{g,v}\,. \tag{B10}$$

Here, ρ_g is the density of the gas; R_g is the universal gas constant; M_g is the molecular weight of the gas in the bubble; $D_{g,v}$ is the thermal diffusivity of the gas defined at constant volume; T_∞ is the ambient temperature. A correction up to second order of G_1 [e.g., the second term in the bracket of Eq. (B7)] has been proposed by Zhang (2013b). The natural frequency ω_0 of bubble oscillation under single-frequency excitation is calculated by Eq. (2.5).

The equation of bubble motion [Eqs. (2.1)-(2.3)] is directly solved by an explicit Runge-Kutta formula (Dormand and Prince, 1980) for a wide range of parameters, such as bubble radius, pressure amplitude and frequency of acoustic excitation. The physical parameters employed in the simulations are: $D_{g,v}$=2.90×10^{-5} m^2/s; R_g =8.314 J/(mol K); M_g =28.88

g; ρ_g =1.204 kg/m^3; T_∞ =293.15 K; ε varies between 0.05 and 1.2; and R_0 =2, 10 and 50 μm respectively. Other constants are listed in Appendix A. In the following figures and discussions, non-dimensional values are used, such as ω/ω_0, ε and $\left(R_{\max}-R_0\right)/R_0$ (Here, $R_{\max}$ is the maximum radius of the bubble during steady-state oscillations); "Present" refers to the predictions using values of κ and μ_{th} predicted by Eqs. (B1)-(B10); "κ=1.0, μ_{th}=0" and "κ=1.4, μ_{th}=0" refer to the predictions using 1.0 and 1.4 as the values of polytropic exponent respectively without energy dissipation through heat transfer.

Figures B1-B3 show the frequency response curves predicted by three approaches for equilibrium bubble radii of 2, 10 and 50 μm respectively for a wide range of parameters (e.g., $0.05 \le \varepsilon \le 1.2$; $0.1 \le \omega/\omega_0 \le 3$). In order to show the differences clearly, comparisons of the frequency response curves by three approaches are demonstrated in Figures B4-B6. The expressions n/m (Here, *m* and *n* are two integers) marked above the peaks of the curves in Figures B1-B3 are the orders of the resonances (referring to Sec. 1.3.1 and Lauterborn 1976 for detailed definition). Cases with *m* =1 and *n* =2, 3… correspond to harmonics; cases with *m* =2, 3… and *n* =1 correspond to subharmonics; cases with *m* =2, 3… and *n* =2, 3… correspond to ultraharmonics. Figure B7 shows an example of the onset

curve [i.e., curve of $(R_{\max} - R_0)/R_0$ versus ε] of gas bubbles with radius R_0 =10 μm at the subharmonic region ($\omega/\omega_0 \approx 2$). Figure B8 shows the comparisons of the threshold pressure of the subharmonics of the order $n/m = \frac{1}{2}$ versus the equilibrium bubble radius. Figures B1-B8 reveal typical characteristics of nonlinear oscillations of gas bubbles in the liquids, such as main resonances, harmonics, subharmonics and ultraharmonics. Furthermore, near resonances, the frequency response curves lean over towards low frequencies (corresponding to small values of ω/ω_0) at higher acoustic pressure amplitudes (corresponding to large ε) as shown in Figures B1-B6. Those nonlinear features observed in this Appendix agree well with the well-known results given by Lauterborn (1976), confirming the validities of our simulations. In the following discussions, our efforts are mainly focused on the influence of thermal effects (e.g., values of κ and μ_{th}) on the bubble responses to the acoustic excitation.

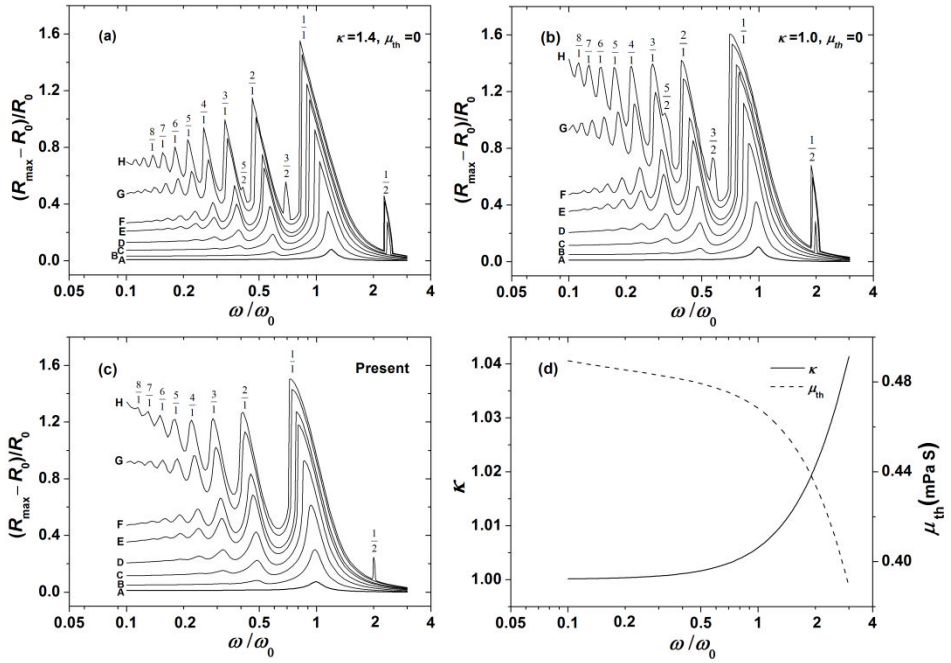

Figure B1 Frequency response curves predicted by three approaches (a) "κ=1.4, μ_{th}=0", (b) "κ=1.0, μ_{th}=0", and (c) "Present" for bubbles with equilibrium radius R_0=2 μm. Non-dimensional amplitudes of acoustic excitation (ε) are (A) 0.05, (B) 0.2, (C) 0.4, (D) 0.6, (E) 0.8, (F) 0.9, (G) 1.1, and (H) 1.2 respectively. The numbers above the peaks of the curves are the orders of the resonances. The values of κ (solid line) and μ_{th} (dashed line) employed in the approach "Present" [calculated by Eqs. (B1)-(B10)] are shown in (d).

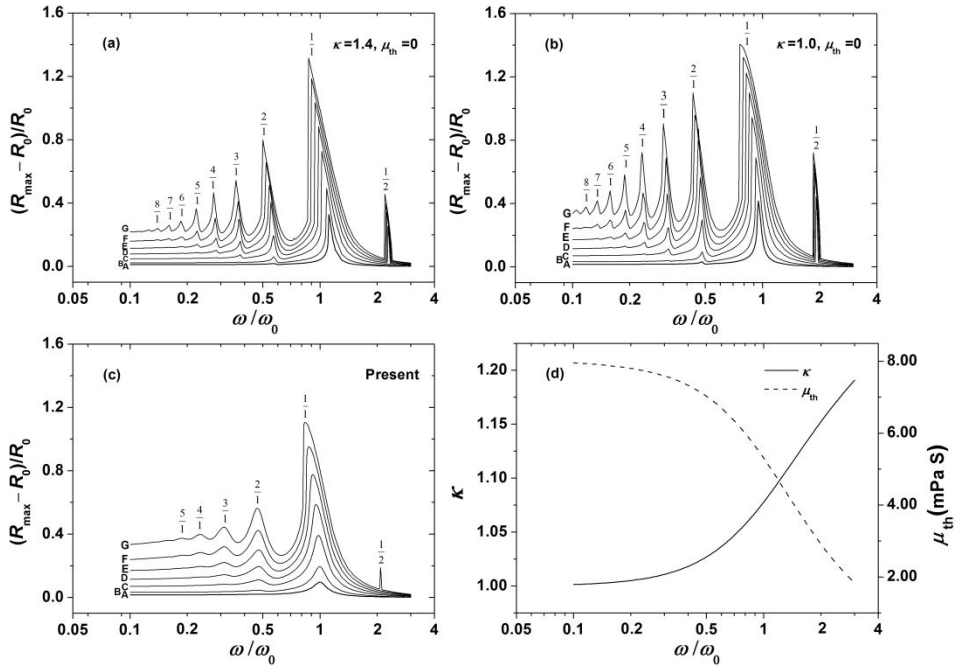

Figure B2 Frequency response curves predicted by three approaches (a) "κ=1.4, μ_{th}=0", (b) "κ=1.0, μ_{th}=0", and (c) "Present" for bubbles with equilibrium radius R_0=10 μm. Non-dimensional amplitudes of acoustic excitation (ε) are (A) 0.05, (B) 0.1, (C) 0.2, (D) 0.3, (E) 0.4, (F) 0.5, and (G) 0.6 respectively. The numbers above the peaks of the curves are the orders of the resonances. The values of κ (solid line) and μ_{th} (dashed line) employed in the approach "Present" [calculated by Eqs. (B1)-(B10)] are shown in (d).

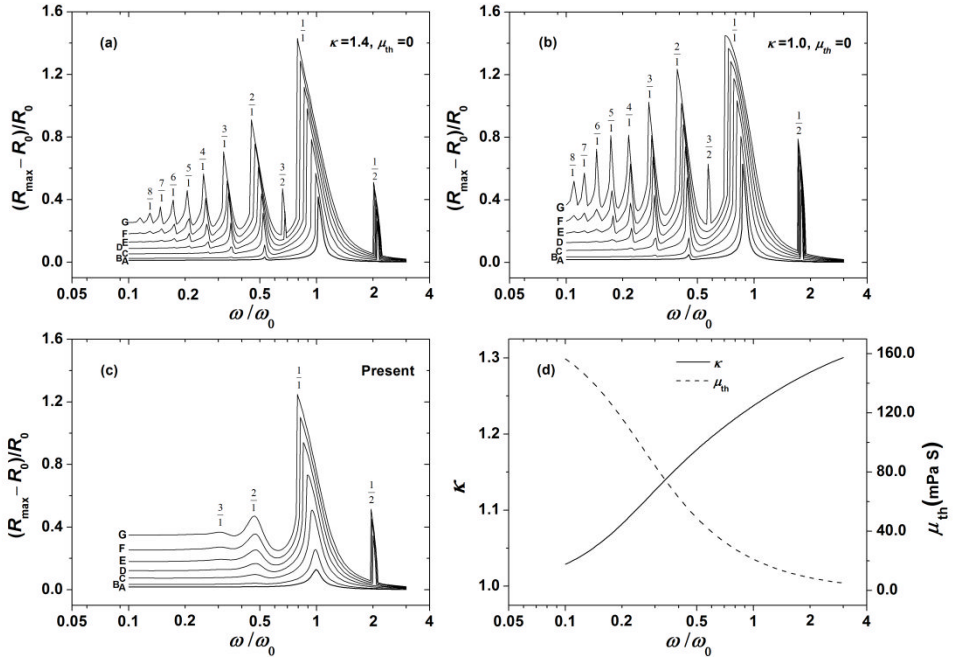

Figure B3 Frequency response curves predicted by three approaches (a) "κ=1.4, μ_{th}=0", (b) "κ=1.0, μ_{th}=0", and (c) "Present" for bubbles with equilibrium radius R_0=50 μm. Non-dimensional amplitudes of acoustic excitation (ε) are (A) 0.05, (B) 0.1, (C) 0.2, (D) 0.3, (E) 0.4, (F) 0.5, and (G) 0.6 respectively. The numbers above the peaks of the curves are the orders of the resonances. The values of κ (solid line) and μ_{th} (dashed line) employed in the approach "Present" [calculated by Eqs. (B1)-(B10)] are shown in (d).

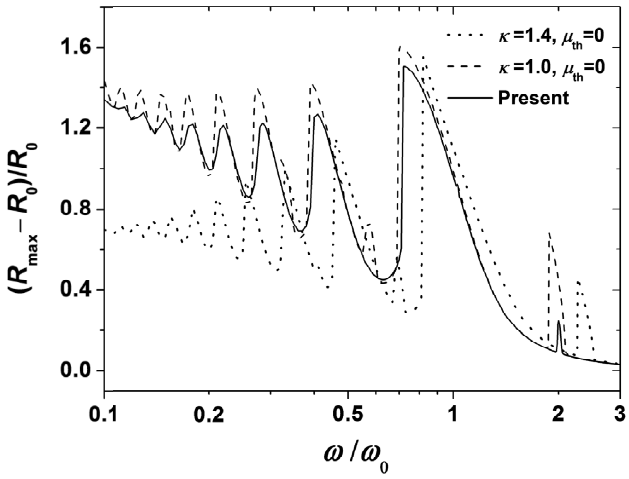

Figure B4 Frequency response curves predicted by three approaches "κ =1.4, μ_{th} =0" (dotted line), "κ =1.0, μ_{th} =0" (dashed line), and "Present" (solid line) for bubbles with equilibrium radius R_0=2 μm. ε =1.2.

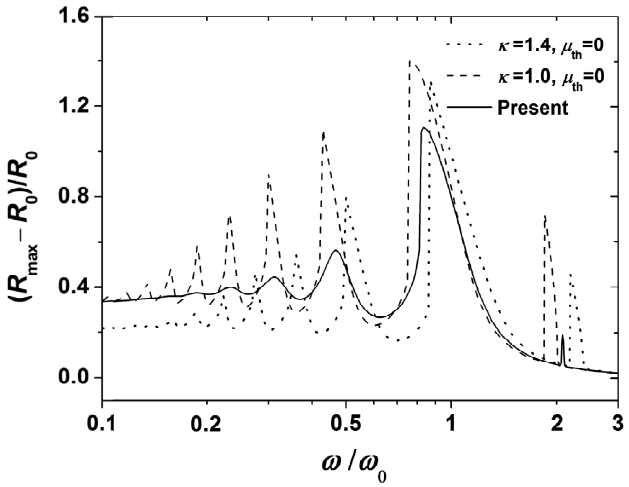

Figure B5 Frequency response curves predicted by three approaches "κ =1.4, μ_{th} =0" (dotted line), "κ =1.0, μ_{th} =0" (dashed line), and "Present" (solid line) for bubbles with equilibrium radius R_0=10 μm. ε =0.6.

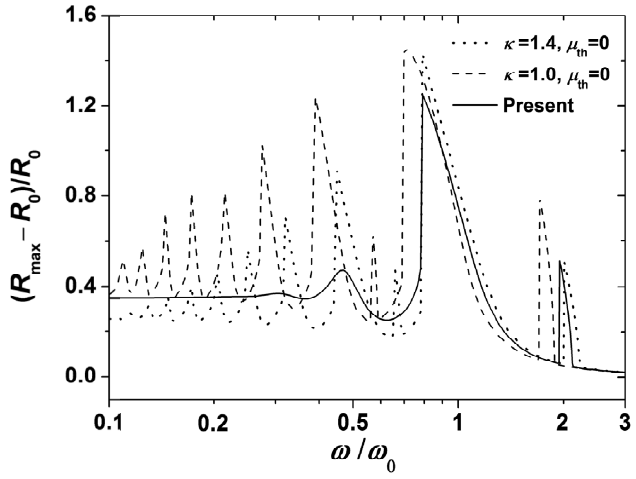

Figure B6 Frequency response curves predicted by three approaches "κ =1.4, μ_{th} =0" (dotted line), "κ=1.0, μ_{th} =0" (dashed line), and "Present" (solid line) for bubbles with equilibrium radius R_0=50 μm. ε =0.6.

From Figures B1-B8, it can be seen clearly that the predictions by the three approaches are significantly different, which can be summarized as follows. The locations and amplitudes of the main, harmonic and subharmonic resonances predicted by "Present" are quite different from those predicted by other two approaches ("κ=1.4, μ_{th} =0" and "κ=1.0, μ_{th} =0" respectively). As shown by Eq. (2.5), natural frequency (ω_0) is strongly dependent on the polytropic exponent (κ). Therefore, values of ω_0 predicted by "κ=1.4, μ_{th} =0" are larger than those by "κ=1.0, μ_{th} =0" and "Present", resulting in the locations of the resonances by "κ=1.4, μ_{th} =0" shifting to the right (i.e., larger values of ω/ω_0) as shown in Figures B1-B6. Energy dissipation through heat transfer across interfaces

of gas bubbles (represented by μ_{th}) is one of the important damping mechanisms during oscillations of gas bubbles in the liquids. By accounting for the energy dissipation through heat transfer, the oscillation amplitudes (especially near resonances) are greatly suppressed, referring to Figures B1-B6.

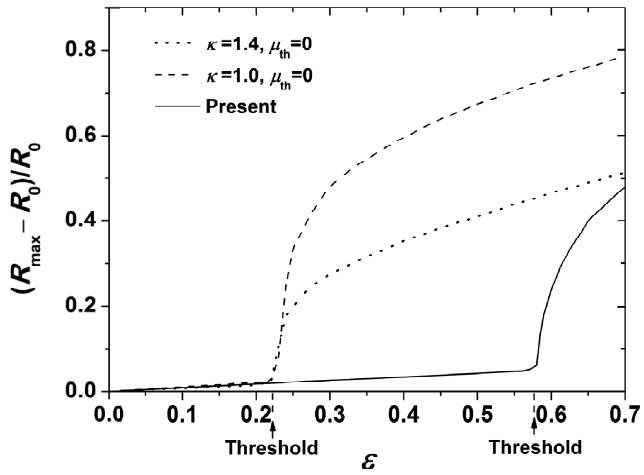

Figure B7 Comparisons of the onset curves of subharmonic resonance with the order of $\frac{1}{2}$ predicted by three approaches "κ=1.4, μ_{th}=0" (dotted line), "κ=1.0, μ_{th}=0" (dashed line), and "Present" (solid line). R_0=10 μm. The values of the threshold of the subharmonic resonances with the order of $\frac{1}{2}$ have been marked in the figure.

In particular, the influence of the values of κ and μ_{th} on bubble behaviours is also strongly dependent on bubble radii. For small bubbles (R_0=2 μm), the polytropic exponent varies between 1 and 1.04; the effective thermal viscosity varies between 0.389 mPa s and 0.489 mPa s as

shown in Figure B1(d). Noticing that μ_l =1.0 mPa s for water, if assuming κ =1.4 and μ_{th} =0, it will cause serious errors leading to large differences between "κ =1.4, μ_{th} =0" and "Present" in Figures B1 and B4. The locations of resonances can be predicted well by "κ =1.0, μ_{th} =0" but the oscillation amplitudes near resonances predicted by "κ =1.0, μ_{th} =0" are much higher than those predicted by "Present" owing to ignoring heat transfer across bubble interfaces in "κ =1.0, μ_{th} =0". For the three approaches, the main resonances, the harmonics of all orders (up to $\frac{8}{1}$) and the first subharmonics (with the order of $\frac{1}{2}$) have been all revealed in predictions (referring to Figure B1) for the same parameter zone. However, the ultraharmonics (e.g., $n/m=\frac{3}{2}$, $\frac{5}{2}$ in Figure B1) predicted by "κ =1.0, μ_{th} =0" and "κ =1.4, μ_{th} =0" are not observed in "Present", indeed indicating higher values of the threshold for those ultraharmonics. From Figure B1, it can be seen that the values of the threshold of subharmonics for the order of $\frac{1}{2}$ predicted by "Present" are much higher than those by "κ =1.0, μ_{th} =0" and "κ =1.4, μ_{th} =0". For more detailed analysis, readers are referred to Figures B7 and B8. For fixed bubble radii, onset curves of subharmonics for the order of $\frac{1}{2}$ are obtained by calculating the values of $\left(R_{\max}-R_0\right)/R_0$ at ω/ω_0 =2 versus variable ε as shown in Figure B7. Based on this onset curve, thresholds of the $\frac{1}{2}$-order subharmonics (as marked in Figure B7) are obtained. Figure B8

summarizes the values of the threshold of $\frac{1}{2}$-order subharmonics versus equilibrium bubble radius. As shown in Figures B1-B3 and B8, the values of the threshold of the $\frac{1}{2}$-order subharmonics predicted by the "Present" are higher than those by "κ=1.0, μ_{th}=0" and "κ=1.4, μ_{th}=0". These differences increase with the increase of bubble radius (R_0).

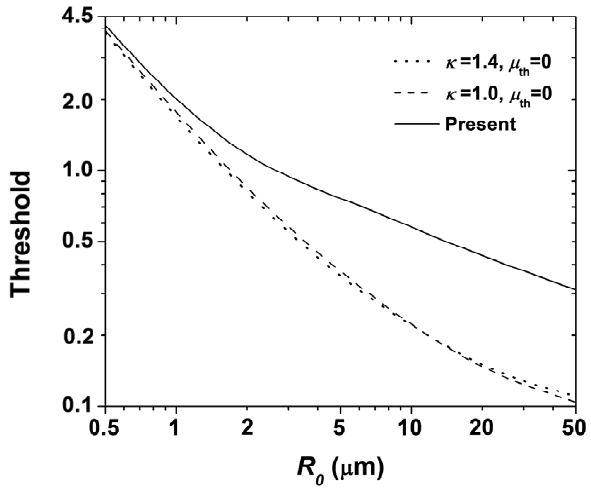

Figure B8 Comparisons of the threshold of subharmonic resonance with the order of $\frac{1}{2}$ predicted by three approaches "κ=1.4, μ_{th}=0" (dotted line), "κ=1.0, μ_{th}=0" (dashed line), and "Present" (solid line) versus equilibrium bubble radius (R_0).

As shown in Figures B2(d) and B3(d), for intermediate and large bubbles (R_0=10 μm and 50 μm respectively), the polytropic exponent varies in the regions [1, 1.19] and [1.03, 1.30] respectively; the effective thermal viscosity varies in the regions [1.84 mPa s, 7.96 mPa s] and [4.98 mPa s, 156.52 mPa s]. For these cases, the polytropic exponent shows strong

variations and the energy dissipation through heat transfer is much more significant than that through water viscosity. Hence, as shown in Figures B2, B3, B5 and B6, both "κ=1.0, μ_{th}=0" and "κ=1.4, μ_{th}=0" cannot predict the bubble behaviours accurately in comparison with "Present" in terms of their locations and amplitudes for main, harmonic and subharmonic resonances. Unlike the cases for small bubbles (e.g., R_0=2 μm in Figures B1 and B4), certain harmonics of high orders (e.g., $n/m > \frac{5}{1}$ in Figure B2 and $n/m > \frac{3}{1}$ in Figure B3) predicted by "κ=1.0, μ_{th}=0" and "κ=1.4, μ_{th}=0" are not presenting in predictions of "Present" because the accounted thermal damping mechanism (i.e., μ_{th} term) damps the bubble oscillations, leading to a strong suppression of harmonics. Similarly for the cases of R_0=2 μm (referring to Figures B1 and B4), ultraharmonics predicted by "κ=1.0, μ_{th}=0" and "κ=1.4, μ_{th}=0" are also not appearing in predictions of "Present" (as shown in Figures B2, B3, B5 and B6). Figures B2 and B3 show higher values of the threshold of subharmonics with order $\frac{1}{2}$ predicted by "Present" in comparison with those by other two approaches.

The effectiveness of the polytropic model has been confirmed by numerous studies (Prosperetti, 1977; Crum, 1983; Crum and Prosperetti, 1983). Due to its simplicity and comparable accuracy, the polytropic

model is still prevalent in the current literature not only for exploring the highly nonlinear bubble phenomenon but also for performing some advanced simulations of non-spherical bubble dynamics. However, the polytropic model cannot be used for simulating very strong gas bubble oscillations because a prominent non-uniformity will form inside gas bubbles. A complete understanding of those highly nonlinear oscillations of gas bubbles can be obtained by solving a full set of nonlinear equations inside and outside the bubbles rather than using a polytropic model. For a complete discussion of the validity of polytropic model, readers are referred to Prosperetti et al. (1988).

In summary, the values of κ and μ_{th} would not affect the basic characteristics of nonlinear bubble oscillations (e.g., the existence of main, harmonic, subharmonic and ultraharmonic resonances; the "jump phenomenon" and the "bending phenomenon"). However, they could influence the responses of the gas bubbles to the single-frequency acoustic excitation on the aspects of the locations and magnitudes of the resonances, and the thresholds of subhormonics and ultraharmonics.

Appendix C: Mass Transfer across Interfaces of Gas Bubbles under Dual-Frequency Acoustic Excitation

In this Appendix, mass transfer across bubble interfaces under dual-frequency acoustic excitation is investigated. Parts of this Appendix have been submitted as a journal paper (Zhang et al., 2015, under review).

Specifically, the influence of two paramount parameters (i.e., the pressure amplitudes and frequencies of external acoustic excitation) of the dual-frequency approach on the mass transfer across bubble-liquid interfaces is studied numerically. The size of the region in which bubbles grow through the effects of mass transfer during stable cavitation is proposed as a criterion for the optimization of the multiple-frequency system.

The equation of bubble motion used is that developed by Keller and Miksis (1980) [Eqs. (2.1)-(2.4)]. The bubble growth rate can be given as

(Crum, 1984),

$$\frac{dR_0}{dt}=\frac{DR_gT_\infty C_0}{R_0P_0}\left[\langle R/R_0\rangle+R_0\left(\frac{\left\langle (R/R_0)^4\right\rangle}{\pi tD}\right)^{1/2}\right]$$

$$\times\left(1+\frac{4\sigma}{3P_0R_0}\right)^{-1}\left(\frac{C_i}{C_0}-\frac{\left\langle (R/R_0)^4(P_{in}/P_0)\right\rangle}{\left\langle (R/R_0)^4\right\rangle}\right). \quad \text{(C1)}$$

Here, R_g is the universal gas constant; T_∞ is the ambient temperature in the liquid; C_0 is the saturation concentration of the gas in the liquid; C_i is the concentration of the gas in the liquid at infinity; D is the diffusion constant; and $\langle\ \rangle$ denotes time-averaged terms, which can be determined based on the solution of the equations of bubble motion [i.e., Eqs. (2.1)-(2.4)]. Up to the second order of P_{A1}/P_0, the three time-averaged terms can be described as (Zhang, 2012b),

$$\left\langle R/R_0\right\rangle=1+B_2\left(P_{A1}/P_0\right)^2, \quad \text{(C2)}$$

$$\left\langle (R/R_0)^4\right\rangle=1+\left[4B_2+3\left(A_{11}^2+A_{12}^2\right)\right]\left(P_{A1}/P_0\right)^2, \quad \text{(C3)}$$

$$\left\langle (R/R_0)^4(P_{in}/P_0)\right\rangle=\left(1+\frac{2\sigma}{P_0R_0}\right)\left\langle (R/R_0)^{4-3\kappa}\right\rangle=$$

$$\left(1+\frac{2\sigma}{P_0R_0}\right)\left\{1+\left[\left(4-3\kappa\right)B_2+\frac{\left(4-3\kappa\right)\left(3-3\kappa\right)}{4}\left(A_{11}^2+A_{12}^2\right)\right]\left(P_{A_1}/P_0\right)^2\right\}, \quad \text{(C4)}$$

where

$$A_{11}=-\frac{P_0}{M\rho_lR_0^2}\left[\frac{1+\left(\omega_1R_0/c_l\right)^2}{\left(\omega_0^2-\omega_1^2\right)^2+4\beta_{tot}^2\omega_1^2}\right]^{1/2}, \quad \text{(C5)}$$

$$A_{12} = -\frac{P_0 P_{A2}}{M \rho_l R_0^2 P_{A1}} \left[\frac{1 + \left(\omega_2 R_0 / c_l\right)^2}{\left(\omega_0^2 - \omega_2^2\right)^2 + 4\beta_{tot}^2 \omega_2^2} \right]^{1/2}, \tag{C6}$$

$$B_2 = -\frac{1}{4\omega_0^2 M}\left(A_{11}^2 \omega_1^2 + A_{12}^2 \omega_2^2\right) + \frac{1}{4}\frac{A_{11}^2 + A_{12}^2}{\rho_l R_0^2 \omega_0^2 M}\left[3\kappa\left(3\kappa+1\right)\left(P_0 + \frac{2\sigma}{R_0}\right) - \frac{4\sigma}{R_0}\right], \tag{C7}$$

with

$$\omega_0^2 = \frac{1}{M \rho_l R_0^2}\left[3\kappa\left(P_0 + \frac{2\sigma}{R_0}\right) - \frac{2\sigma}{R_0}\right],$$

$$\beta_{tot} = \frac{2\mu_l}{M \rho_l R_0^2} + \frac{R_0}{2c_l}\omega_0^2,$$

$$M = 1 + \frac{4\mu_l}{\rho_l R_0^2}\frac{R_0}{c_l}.$$

Hence, the bubble growth or dissolution rate can be obtained by integration of Eq. (C1). According to Eq. (C1), there exists a threshold of the pressure amplitude, the value of which corresponds to the balance of the amount of gas diffused into and out of the bubbles [i.e., $dR_0/dt = 0$ in Eq. (C1)]. The constants employed in the simulations are: D=2.4×10^{-9} m^2/s; R_g =8.314 J/mol/K; T_∞ =293.15 K; $\omega_1 = 5\times10^5 s^{-1}$; $\omega_2 = 1.5\times10^6 s^{-1}$, $2.5\times10^6 s^{-1}$ and $5\times10^6 s^{-1}$ respectively (i.e., $\omega_2 = 3\omega_1$, $5\omega_1$ and $10\omega_1$). Other constants are the same as those listed in Appendix A. The pressure amplitudes of the component sound waves are P_{A1} and P_{A2} respectively. The total pressure amplitude is denoted as $P_e = \left(P_{A1}^2 + P_{A2}^2\right)^{1/2}$. The power allocation between two component waves is

indicated by $N = P_{A2}/P_{A1}$. The total threshold pressure amplitude and corresponding pressure amplitudes of two acoustic waves under dual-frequency approach are denoted as P_{Te}, P_{TA1} and P_{TA2} respectively. Thus, $P_{Te} = \left(P_{TA1}^2 + P_{TA2}^2\right)^{1/2}$. If $P_e > P_{Te}$, the bubble will grow while if $P_e < P_{Te}$, the bubble will dissolve.

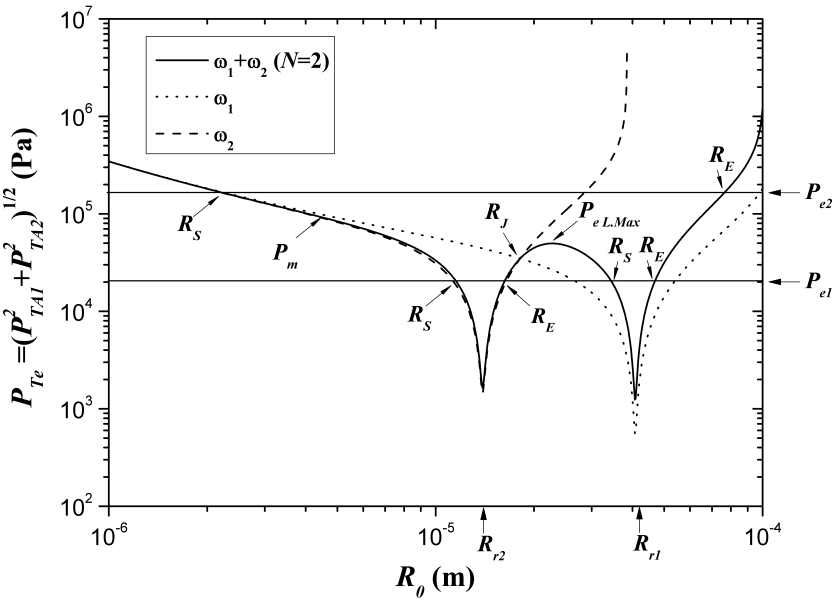

Figure C1 The predicted threshold of the total acoustic pressure amplitude of rectified mass diffusion under single-frequency [marked as "ω_1" (dotted line) and "ω_2" (dashed line)] and dual-frequency [marked as "$\omega_1 + \omega_2$" (solid line), N=2] acoustic excitation. $\omega_1 = 5\times10^5 s^{-1}$. $\omega_2 = 3\omega_1 = 1.5\times10^6 s^{-1}$. R_{r1} and R_{r2} are the resonance bubble radii of gas bubbles under acoustic excitation with frequencies ω_1 and ω_2 respectively. R_S and R_E are the start and the end bubble radii of bubble growth region respectively. For others, readers are referred to the texts.

Figure C1 compares the predicted total threshold of acoustic pressure amplitudes of mass diffusion under single-frequency and dual-frequency acoustic excitation (N=2). Firstly, some definitions employed in present analysis are briefly explained. Between two resonance bubble radii (R_{r1} and R_{r2} respectively), there exists a local maximum of the threshold value (marked as $P_{e\,L.\max}$), which is a paramount parameter as shown in the following discussions. The left branches of dual-frequency approach and single-frequency approach merge at the point corresponding to the pressure amplitude P_m. Hence, the threshold curve can be divided into three regions using $P_{e\,L.\max}$ and P_m.

Region A: If $P_e < P_{e\,L.\max}$, there are four intersections (denoted as R_S and R_E respectively) between the threshold curve and P_e (the solid line marked as P_{e1}). Here, R_S and R_E are the bubble radii corresponding to the start and the end of the bubble growth regions respectively. According to the theory of mass diffusion, only the bubble with radius in the region (R_S, R_E) can grow under acoustic excitation to the final equilibrium bubble radius R_E. However, because the acoustic pressure amplitude is not large enough (i.e., $P_e < P_{e\,L.\max}$), the bubble growth regions do not significantly increase through the use of dual-frequency excitation.

Region B: If $P_{e\,L.\max} < P_e < P_m$, there are only two cross points between the

threshold curve and P_e. Compared with the single-frequency approach, the bubble growth region under the dual-frequency approach has significantly increased.

Region C: If $P_e > P_m$, there are only two cross points between the threshold curve and P_e (the solid line marked as P_{e2}). Compared with the single-frequency approach with frequency ω_2, the bubble growth region under dual-frequency approach increases dramatically though the comparison with the single-frequency approach with frequency ω_1 indicates the bubble growth region under dual-frequency approach almost remains the same.

Figures C2 and C3 show the predictions of the threshold of mass diffusion under single-frequency and dual-frequency acoustic excitation with different ratios of the pressure amplitudes (*N*) for the cases $\omega_2 = 3\omega_1$ and $\omega_2 = 10\omega_1$ respectively. According to Figures C2 and C3, one can find that all the curves with different *N* pass a fixed point denoted as $\left(R_J, P_{e,J}\right)$, which is the intersection of the threshold curves of the two single-frequency excitation. For this special point, the threshold of the mass diffusion is independent of *N*. Figure C4 shows the influence of the pressure ratio (*N*) on the local maximum threshold pressure ($P_{e\,L.\max}$) of dual-frequency excitation. The minimum of $P_{e\,L.\max}$ in each curve is

marked as closed squares in the figure. Table C1 summarises the bubble growth regions under acoustic excitation with different pressure amplitudes (P_e) and N.

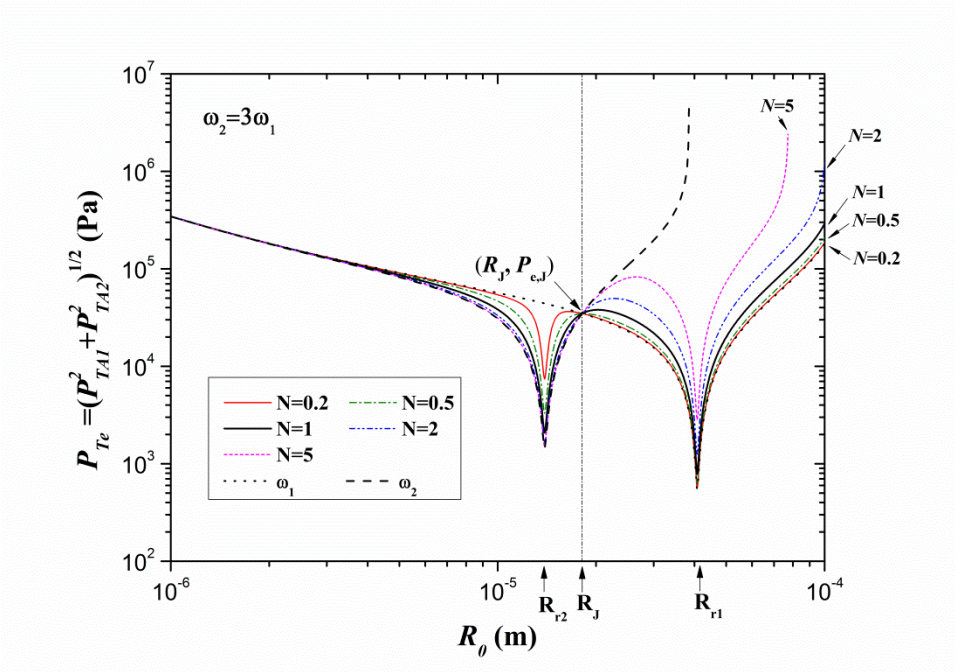

Figure C2 The predicted threshold of the total acoustic pressure amplitude [$P_{Te} = \left(P_{TA1}^2 + P_{TA2}^2 \right)^{1/2}$] of rectified mass diffusion under single-frequency [marked as "ω_1" (dotted line) and "ω_2" (dashed line)] and dual-frequency ("$\omega_1 + \omega_2$" with different N) acoustic excitation. $N = P_{A2}/P_{A1}$ = 0.2, 0.5, 1, 2, 5 respectively. $\omega_1 = 5\times10^5 s^{-1}$. $\omega_2 = 3\omega_1 = 1.5\times10^6 s^{-1}$. R_{r1} and R_{r2} are resonance bubble radii of gas bubbles under acoustic excitation with frequencies ω_1 and ω_2 respectively. $\left(R_J, P_{e,J}\right)$ is the intersection point of all the threshold curves.

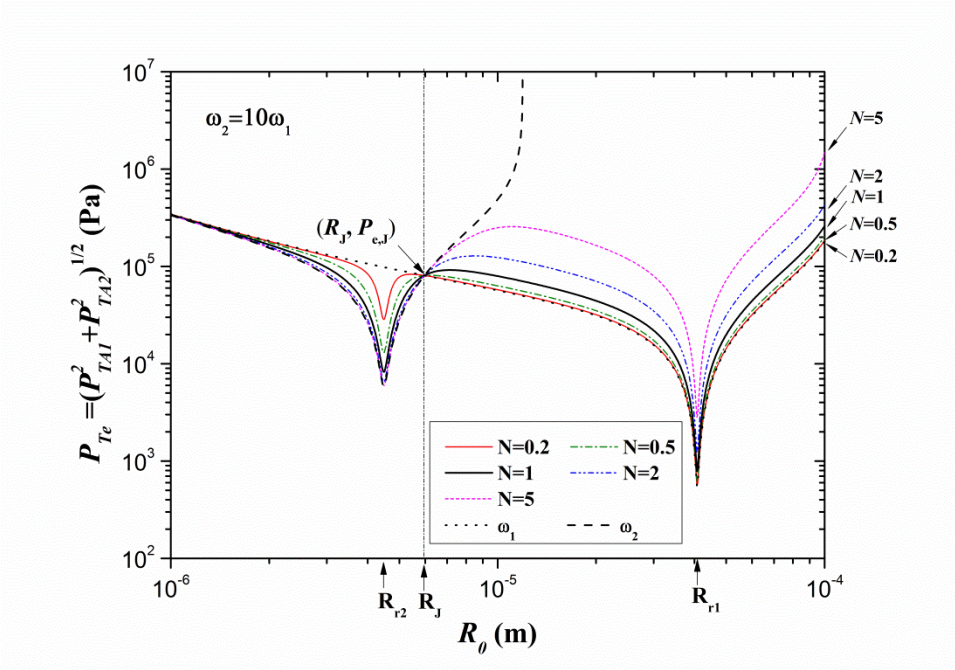

Figure C3 The predicted threshold of the total acoustic pressure amplitude [$P_{Te}=\left(P_{TA1}^2+P_{TA2}^2\right)^{1/2}$] of rectified mass diffusion under single-frequency [marked as "ω_1" (dotted line) and "ω_2" (dashed line)] and dual-frequency ("$\omega_1+\omega_2$" with different *N*) acoustic excitation. $N=P_{A2}/P_{A1}$ = 0.2, 0.5, 1, 2, 5 respectively. $\omega_1=5\times10^5 s^{-1}$. $\omega_2=10\omega_1=5\times10^6 s^{-1}$. R_{r1} and R_{r2} are resonance bubble radii of gas bubbles under acoustic excitation with frequencies ω_1 and ω_2 respectively. $\left(R_J,P_{e,J}\right)$ is the intersection point of all the threshold curves.

Table C1 Bubble growth regions under single-frequency excitation and dual-frequency excitation with different N. P_e=60000 Pa, 45000 Pa and 38000 Pa respectively. N=0.2, 0.5, 1, 2 and 5 respectively. $\omega_2 = 3\omega_1$.

		N	Bubble growth region (μm) (R_E, R_S)
$P_e = 60000Pa$			
$P_e > P_{e\,L.\max,\,N=2}$	Dual-frequency	0.2	(8.91, 72.87)
		0.5	(8.11, 70.68)
		1	(7.40, 65.52)
$P_e < P_{e\,L.\max,\,N=5}$		2	(6.98, 57.41)
		5	(6.80, 21.23); (32.40, 48.47)
	Single-frequency	ω_1	(9.09, 73.54)
		ω_2	(6.74, 20.98)
		N	Bubble growth region (μm) (R_E, R_S)
$P_e = 45000Pa$			
$P_e > P_{e\,L.\max,\,N=1}$	Dual-frequency	0.2	(11.63, 66.47)
		0.5	(10.21, 64.58)
		1	(9.18, 60.24)
$P_e < P_{e\,L.\max,\,N=2}$		2	(8.60, 20.07); (26.27, 53.64)
		5	(8.37, 19.35); (34.62, 46.63)
	Single-frequency	ω_1	(14.23, 67.06)
		ω_2	(8.30, 19.33)
		N	Bubble growth region (μm) (R_E, R_S)
$P_e = 38000Pa$			
$P_e > P_{e\,L.\max,\,N=0.5}$	Dual-frequency	0.2	(12.58, 15.49); (18.00, 61.07)
		0.5	(11.31, 59.88)
		1	(10.38, 18.19); (23.23, 56.37)
$P_e < P_{e\,L.\max,\,N=0.2}$		2	(9.78, 18.16); (29.78, 50.96)
		5	(9.54, 18.16); (35.85, 45.15)
	Single-frequency	ω_1	(18.00, 63.22)
		ω_2	(9.44, 18.18)

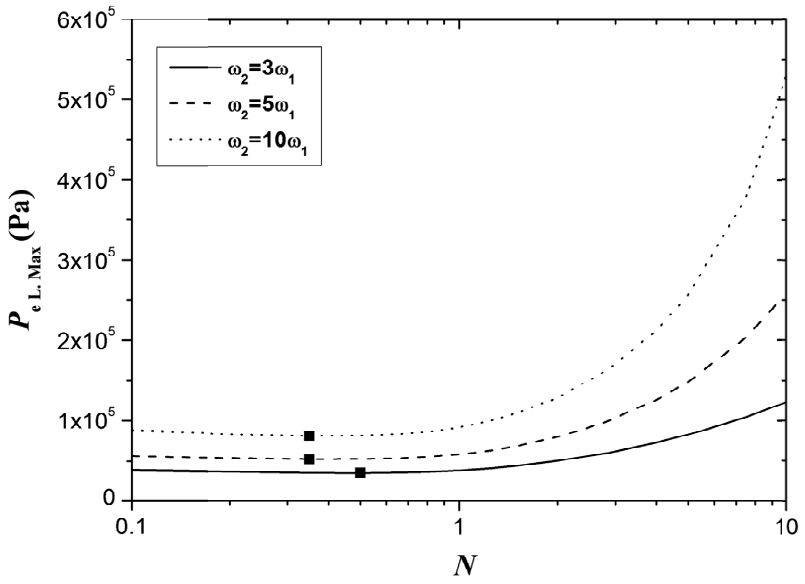

Figure C4 Predicted local maximum threshold pressure ($P_{e\ L.Max}$) versus the ratio of two excitation acoustic pressure amplitudes (*N*). "■" indicates the minimum of $P_{e\ L.Max}$. $N = P_{A2}/P_{A1}$ = 0.1-10. $\omega_1 = 5\times10^5 s^{-1}$. $\omega_2 = 3\omega_1$ (solid line), $5\omega_1$ (dashed line), $10\omega_1$ (dotted line) respectively.

The characteristics of the threshold curves (Figures C2-C4 and Table C1) can be summarized as follows:

1. *N* has great influence on the threshold curves of dual-frequency approach. For *N* <1, with the decrease of *N*, the threshold curves become much narrower near $R_0 \approx R_{r2}$ while those near $R_0 \approx R_{r1}$ almost remain the same as those under single-frequency excitation with frequency ω_1. For *N* >1, with the increase of *N*, the threshold curves become much narrower near $R_0 \approx R_{r1}$ vary while those near $R_0 \approx R_{r2}$ almost remain the same as those under single-frequency excitation with frequency ω_2.
2. R_J is an important parameter dividing the Figures C2 and C3 into two regions. For $R_0 < R_J$, the threshold of acoustic pressure amplitude decreases with the increase of *N*. For $R_0 > R_J$, the threshold of acoustic pressure amplitude increases with the increase of *N*.
3. The ratio of the frequencies (ω_2/ω_1) has great influence on the threshold curve. Firstly, the region between two resonance radii (R_{r1} and R_{r2} respectively) will increase with the increase of the ratio of frequencies. Secondly, the threshold pressure amplitude will also increase with the increase of the ratio of frequencies as shown in Figures C2 and C3. For example, for *N*=0.2, the minimum threshold pressure near $R_0 \approx R_{r2}$ is 7415 Pa and 28571 Pa for $\omega_2 = 3\omega_1$ and

$\omega_2 = 10\omega_1$ respectively. Hence, the difference of threshold pressure amplitude is significant for the large frequency ratio. Thirdly, the local maximum threshold pressure amplitude (especially when N >1) also increases with the increase of the ratio of frequencies. For example, as shown in Figure C4, when N=10, $P_{e\,L.\max}$ of ω_2/ω_1 =5 and 10 are more than two and four times of those of ω_2/ω_1 =3. This implies that for a given pressure amplitude, bubble growth regions will shrink with the increase of the frequency ratio.

4. For $N \le 1$, the changes of $P_{e\,L.\max}$ versus N is quite limited while for $N > 1$, $P_{e\,L.\max}$ increases significantly with the increase of N. For high values of N, if the $P_{e\,L.\max} > P_m$, the size of bubble growth region under dual-frequency excitation is nearly the same as those under single-frequency excitation. Therefore, for facilitating the effects of mass transfer, the pressure amplitude of the low-frequency component (ω_1) should be higher than those of the high-frequency component (ω_2) (i.e., the ratio of pressure amplitudes $N \le 1$).

In summary, a criterion based on bubble growth regions for optimizing the parameters of a dual-frequency approach is proposed. According to the numerical simulations, it is more effective to facilitate cavitation (e.g., the growth of bubbles) through allocating the power to the low-frequency

component of dual-frequency acoustic waves. With the increase of the frequency ratio, the difference between the size of bubble growth regions under dual-frequency and single-frequency excitation shrinks.

References

Adewuyi, Yusuf G. "Sonochemistry: environmental science and engineering applications." Industrial & Engineering Chemistry Research 40.22 (2001): 4681-4715.

Allen, John S., and Ronald A. Roy. "Dynamics of gas bubbles in viscoelastic fluids. I. Linear viscoelasticity." The Journal of the Acoustical Society of America 107.6 (2000): 3167-3178.

Allen, John, and Ronald A. Roy. "Bubble dynamics in non‐Newtonian fluids." The Journal of the Acoustical Society of America 103.5 (1998): 3013-3013.

Akhatov, I., U. Parlitz, and W. Lauterborn. "Pattern formation in acoustic cavitation." The Journal of the Acoustical Society of America 96.6 (1994): 3627-3635.

Ashokkumar, Muthupandian. "The characterization of acoustic cavitation bubbles–An overview." Ultrasonics sonochemistry 18.4 (2011): 864-872.

Barati, Amir H., et al. "Effect of exposure parameters on cavitation induced by low-level dual-frequency ultrasound." Ultrasonics sonochemistry 14.6 (2007): 783-789.

Barbat, Tiberiu, Nasser Ashgriz, and Ching-Shi Liu. "Dynamics of two interacting bubbles in an acoustic field." Journal of Fluid Mechanics 389 (1999): 137-168.

Behnia, Sohrab, et al. "Nonlinear transitions of a spherical cavitation bubble." Chaos, Solitons & Fractals 41.2 (2009a): 818-828.

Behnia, Sohrab, et al. "Towards classification of the bifurcation structure of a spherical cavitation bubble." Ultrasonics 49.8 (2009b): 605-610.

Behnia, Sohrab, et al. "Suppressing chaotic oscillations of a spherical cavitation bubble through applying a periodic perturbation." Ultrasonics sonochemistry 16.4 (2009c): 502-511.

Behnia, S., et al. "Chaotic behavior of gas bubble in non-Newtonian fluid: a numerical study." Nonlinear Dynamics 74.3 (2013a): 559-570.

Behnia, S., et al. "Observations on the dynamics of bubble cluster in an ultrasonic field." Nonlinear Dynamics 72.3 (2013b): 561-574.

Bjerknes, V. (1906). Fields of force.

Braiman, Y., and I. Goldhirsch. "Taming chaotic dynamics with weak periodic perturbations." Physical review letters 66.20 (1991): 2545.

BRENNEN, CE. "Cavitation and bubble dynamics [M] Oxford University Press." New York, USA (1995).

Brenner, Michael P., Sascha Hilgenfeldt, and Detlef Lohse. "Single-bubble sonoluminescence." Reviews of modern physics 74.2 (2002): 425.

Brotchie, Adam, Muthupandian Ashokkumar, and Franz Grieser. "Effect of water-soluble solutes on sonoluminescence under dual-frequency sonication." The Journal of Physical Chemistry C 111.7 (2007): 3066-3070.

Brotchie, Adam, Franz Grieser, and Muthupandian Ashokkumar. "Sonochemistry and sonoluminescence under dual-frequency ultrasound irradiation in the presence of water-soluble solutes." The Journal of Physical Chemistry C 112.27 (2008): 10247-10250.

Brotchie, Adam, et al. "Cavitation activation by dual-frequency ultrasound and shock waves." Phys. Chem. Chem. Phys. 11.43 (2009): 10029-10034.

Brujan, Emil. Cavitation in Non-Newtonian Fluids: With Biomedical and Bioengineering Applications. Springer Science & Business Media, 2010.

Cabeza, C., et al. "Experimental detection of a subharmonic route to chaos in acoustic cavitation through the tuning of a piezoelectric cavity." The Journal of the Acoustical Society of America 103.6 (1998): 3227-3229.

Carpenedo, L., et al. "Space-time interaction of two ultrasonic fields and sonoluminescence during transient cavitation in distilled water." Acoustics letters 10.11 (1987): 178-181.

Chacón, R., and J. Díaz Bejarano. "Routes to suppressing chaos by weak periodic perturbations." Physical review letters 71.19 (1993): 3103.

Ciuti, Piero, et al. "Cavitation activity stimulation by low frequency field pulses." Ultrasonics sonochemistry 7.4 (2000): 213-216.

Ciuti, P., et al. "Study into mechanisms of the enhancement of multibubble sonoluminescence emission in interacting fields of different frequencies." Ultrasonics sonochemistry 10.6 (2003): 337-341.

Clarke, J. W. L., and T. G. Leighton. "A method for estimating time-dependent acoustic cross-sections of bubbles and bubble clouds prior to the steady state." The Journal of the Acoustical Society of America 107.4 (2000): 1922-1929.

Collin, Jamie RT, and Constantin C. Coussios. "Quantitative observations of cavitation activity in a viscoelastic medium." The Journal of the Acoustical Society of America 130.5 (2011): 3289-3296.

Coussios, Constantin C., and Ronald A. Roy. "Applications of acoustics and cavitation to noninvasive therapy and drug delivery." Annu. Rev. Fluid Mech. 40 (2008): 395-420.

Cox, Tara M., et al. Understanding the impacts of anthropogenic sound on beaked whales. SPACE AND NAVAL WARFARE SYSTEMS CENTER SAN DIEGO CA, 2006.

Crum, L. A. "Acoustic cavitation series: part five rectified diffusion." Ultrasonics 22.5 (1984): 215-223.

Crum, Lawrence A., et al. "Monitoring bubble growth in supersaturated blood and tissue ex vivo and the relevance to marine mammal bioeffects." Acoustics Research Letters Online 6.3 (2005): 214-220.

Crum, Lawrence A. "Bjerknes forces on bubbles in a stationary sound field." The Journal of the Acoustical Society of America 57.6 (1975): 1363-1370.

Crum, Lawrence A. "The polytropic exponent of gas contained within air bubbles pulsating in a liquid." The Journal of the Acoustical Society of America 73.1 (1983): 116-120.

Crum, Lawrence A., and Andrea Prosperetti. "Nonlinear oscillations of gas bubbles in liquids: an interpretation of some experimental results." The Journal of the Acoustical Society of America 73.1 (1983): 121-127.

Czerski, H. "An Inversion of Acoustical Attenuation Measurements to Deduce Bubble Populations." Journal of Atmospheric and Oceanic Technology 29.8 (2012): 1139-1148.

d'Agostino, Luca, and Christopher E. Brennen. "Acoustical absorption and scattering cross sections of spherical bubble clouds." The Journal of the Acoustical Society of America 84.6 (1988): 2126-2134.

Dezhkunov, N. V. "Investigation of sonoluminescence amplification under the interaction of ultrasonic fields widely differing in frequency." Journal of engineering physics and thermophysics 76.1 (2003): 142-150.

Devin Jr, Charles. "Survey of thermal, radiation, and viscous damping of pulsating air bubbles in water." The Journal of the Acoustical Society of America 31.12 (1959): 1654-1667.

Doinikov, Alexander A. "Effects of the second harmonic on the secondary Bjerknes force." Physical Review E 59.3 (1999): 3016.

Doinikov, A. A., and S. T. Zavtrak. "On the mutual interaction of two gas

bubbles in a sound field." Physics of Fluids (1994-present) 7.8 (1995): 1923-1930.

Doinikov, Alexander A. "Viscous effects on the interaction force between two small gas bubbles in a weak acoustic field." The Journal of the Acoustical Society of America 111.4 (2002): 1602-1609.

Doinikov, A. A., and S. T. Zavtrak. "Radiation forces between two bubbles in a compressible liquid." The Journal of the Acoustical Society of America 102.3 (1997): 1424-1431.

Doinikov, Alexander A., Richard Manasseh, and Andrew Ooi. "Time delays in coupled multibubble systems (L)." The Journal of the Acoustical Society of America 117.1 (2005): 47-50.

Doinikov, Alexander A. "Translational motion of two interacting bubbles in a strong acoustic field." Physical Review E 64.2 (2001): 026301.

Doinikov, Alexander A. "Translational motion of a bubble undergoing shape oscillations." Journal of Fluid Mechanics 501 (2004): 1-24.

Dollet, Benjamin, et al. "Nonspherical oscillations of ultrasound contrast agent microbubbles." Ultrasound in medicine & biology 34.9 (2008): 1465-1473.

Dormand, John R., and Peter J. Prince. "A family of embedded Runge-Kutta formulae." Journal of computational and applied mathematics 6.1 (1980): 19-26.

Eckmann, Jean-Pierre. "Roads to turbulence in dissipative dynamical systems." Reviews of Modern Physics 53.4 (1981): 643-654.

Einhorn, Cathy, Jacques Einhorn, and Jean-Louis Luche. "Sonochemistry-The use of ultrasonic waves in synthetic organic chemistry." Synthesis 1989.11 (1989): 787-813.

Ellenberger, Juerg, Jasper M. Van Baten, and Rajamani Krishna. "Exploiting the Bjerknes force in bubble column reactors." Chemical Engineering Science 60.22 (2005): 5962-5970.

Eller, Anthony I. "Growth of bubbles by rectified diffusion." The Journal of the Acoustical Society of America 46.5B (1969): 1246-1250.

Eller, Anthony I. "Bubble Growth by Diffusion in an 11‐kHz Sound Field." The Journal of the Acoustical Society of America 52.5B (1972): 1447-1449.

Eller, Anthony I., and Lawrence A. Crum. "Instability of the motion of a pulsating bubble in a sound field." The Journal of the Acoustical Society of America 47.3B (1970): 762-767.

Eskin, G. I., and D. G. Eskin. "Production of natural and synthesized aluminum-based composite materials with the aid of ultrasonic (cavitation) treatment of the melt." Ultrasonics Sonochemistry 10.4 (2003): 297-301.

Eskin, G. I. "Influence of cavitation treatment of melts on the processes of nucleation and growth of crystals during solidification of ingots and

castings from light alloys." Ultrasonics Sonochemistry 1.1 (1994): S59-S63.

Evans, Allan K. "Instability of converging shock waves and sonoluminescence." Physical Review E 54.5 (1996): 5004.

Fan, Joline M., and Zhe Cui. "Effect of acoustic standing wave in a bubble column." Industrial & engineering chemistry research 44.17 (2005): 7010-7018.

Feng, Ruo, et al. "Enhancement of ultrasonic cavitation yield by multi-frequency sonication." Ultrasonics sonochemistry 9.5 (2002): 231-236.

Feng, Z. C., and L. G. Leal. "Nonlinear bubble dynamics." Annual Review of Fluid Mechanics 29.1 (1997): 201-243.

Gaitan, D. Felipe, et al. "Sonoluminescence and bubble dynamics for a single, stable, cavitation bubble." The Journal of the Acoustical Society of America 91.6 (1992): 3166-3183.

Giordano, Nicholas J., and Hisao Nakanishi. Computational physics. Pearson Education India, 2006.

Gogate, Parag R., et al. "Cavitation reactors: efficiency assessment using a model reaction." AIChE Journal 47.11 (2001): 2526-2538.

Guo, Sijia, Yun Jing, and Xiaoning Jiang. "Temperature rise in tissue ablation using multi-frequency ultrasound." Ultrasonics, Ferroelectrics and

Frequency Control, IEEE Transactions on 60.8 (2013).

Hargreaves, Kirk, and Thomas J. Matula. "The radial motion of a sonoluminescence bubble driven with multiple harmonics." The Journal of the Acoustical Society of America 107.3 (2000): 1774-1776.

Harkin, Anthony, Tasso J. Kaper, and Ali Nadim. "Coupled pulsation and translation of two gas bubbles in a liquid." Journal of Fluid Mechanics 445 (2001): 377-411.

He, Pei Z., et al. "The affection on the tissue lesions of difference frequency in dual-frequency high-intensity focused ultrasound (HIFU)." Ultrasonics sonochemistry 13.4 (2006): 339-344.

Henglein, A. "Sonochemistry: historical developments and modern aspects." Ultrasonics 25.1 (1987): 6-16.

Hernot, Sophie, and Alexander L. Klibanov. "Microbubbles in ultrasound-triggered drug and gene delivery." Advanced drug delivery reviews 60.10 (2008): 1153-1166.

Hilgenfeldt, Sascha, Detlef Lohse, and Michael P. Brenner. "Phase diagrams for sonoluminescing bubbles." Physics of Fluids (1994-present) 8.11 (1996): 2808-2826.

Hilgenfeldt, Sascha, Detlef Lohse, and Michael Zomack. "Response of bubbles to diagnostic ultrasound: a unifying theoretical approach." The European Physical Journal B-Condensed Matter and Complex Systems 4.2

(1998): 247-255.

Holzfuss, Joachim, Matthias Rüggeberg, and Robert Mettin. "Boosting sonoluminescence." Physical review letters 81.9 (1998): 1961.

Ida, Masato. "Alternative interpretation of the sign reversal of secondary Bjerknes force acting between two pulsating gas bubbles." Physical Review E 67.5 (2003): 056617.

Ida, Masato. "Phase properties and interaction force of acoustically interacting bubbles: A complementary study of the transition frequency." Physics of Fluids (1994-present) 17.9 (2005): 097107.

Ida, Masato. "Bubble-bubble interaction: A potential source of cavitation noise." Physical Review E 79.1 (2009): 016307.

G. Iernettia, P. Ciutia, N.V. Dezhkunovb, M. Realic, A. Francescutto, G.K. Johrie, “Enhancement of high-frequency acoustic cavitation effects by a low-frequency stimulation”, Ultrasonics Sonochemistry, 4 (1997) 263-268.

Jepson, P. D., et al. "Gas-bubble lesions in stranded cetaceans." Nature 425.6958 (2003): 575-576.

Jing, Zhujun, and Ruiqi Wang. "Complex dynamics in Duffing system with two external forcings." Chaos, Solitons & Fractals 23.2 (2005): 399-411.

Jordan, Dominic William, and Peter Smith. Nonlinear ordinary differential equations: an introduction for scientists and engineers. New York, 2007.

Kanthale, Parag M., Parag R. Gogate, and Aniruddha B. Pandit. "Modeling aspects of dual frequency sonochemical reactors." Chemical Engineering Journal 127.1 (2007): 71-79.

Kanthale, Parag M., et al. "Experimental and theoretical investigations on sonoluminescence under dual frequency conditions." Ultrasonics sonochemistry 15.4 (2008): 629-635.

Kanthale, Parag M., et al. "Cavity cluster approach for quantification of cavitational intensity in sonochemical reactors." Ultrasonics sonochemistry 10.4 (2003): 181-189.

Keller, Joseph B., and Michael Miksis. "Bubble oscillations of large amplitude." The Journal of the Acoustical Society of America 68.2 (1980): 628-633.

Ketterling, Jeffrey A., and Robert E. Apfel. "Using phase space diagrams to interpret multiple frequency drive sonoluminescence." The Journal of the Acoustical Society of America 107.2 (2000): 819-826.

Komarov, Sergey, et al. "Characterization of acoustic cavitation in water and molten aluminum alloy." Ultrasonics sonochemistry 20.2 (2013): 754-761.

Krefting, Dagmar, Robert Mettin, and Werner Lauterborn. "Two-frequency driven single-bubble sonoluminescence." The Journal of the Acoustical Society of America 112.5 (2002): 1918-1927.

Lauterborn, Werner, and Thomas Kurz. "Physics of bubble oscillations." Reports on Progress in Physics 73.10 (2010): 106501.

Lauterborn, Werner. "Numerical investigation of nonlinear oscillations of gas bubbles in liquids." The Journal of the Acoustical Society of America 59.2 (1976): 283-293.

Lauterborn, W., and U. Parlitz. "Methods of chaos physics and their application to acoustics." The Journal of the Acoustical Society of America 84.6 (1988): 1975-1993.

Lauterborn, W., J. Holzfuss, and A. Billo. "Chaotic behavior in acoustic cavitation." Ultrasonics Symposium, 1994. Proceedings., 1994 IEEE. Vol. 2. IEEE, 1994.

Lauterborn, Werner, et al. "Acoustic cavitation and bubble dynamics." Archives of Acoustics 33.4 (2008): 609-617.

Lauterborn, Werner, and Eckehart Cramer. "Subharmonic route to chaos observed in acoustics." Physical Review Letters 47.20 (1981): 1445.

Lauterborn, Werner, and Claus-Dieter Ohl. "Cavitation bubble dynamics." Ultrasonics sonochemistry 4.2 (1997): 65-75.

Leighton, T. The acoustic bubble. Academic press, 1994.

Leroy, Valentin, et al. "Transmission of ultrasound through a single layer of bubbles." The European Physical Journal E: Soft Matter and Biological Physics 29.1 (2009): 123-130.

Lohse, Detlef, and Sascha Hilgenfeldt. "Inert gas accumulation in sonoluminescing bubbles." The Journal of chemical physics 107.17 (1997): 6986-6997.

Lohse, Detlef, et al. "Sonoluminescing air bubbles rectify argon." Physical review letters 78.7 (1997): 1359.

Qing-Yu, Ma, et al. "Difference-frequency ultrasound generation from microbubbles under dual-frequency excitation." Chinese Physics B 19.9 (2010): 094302.

Marković, S., et al. "Ultrasonic de-agglomeration of barium titanate powder."Ultrasonics sonochemistry 15.1 (2008): 16-20.

Marinesco, N., and J. J. Trillat. "Action of supersonic waves upon the photographic plate." Proc R Acad Sci 196 (1933): 858-860.

Mason, Timothy J. "Sonochemistry: current uses and future prospects in the chemical and processing industries." Philosophical Transactions of the Royal Society of London. Series A: Mathematical, Physical and Engineering Sciences 357.1751 (1999): 355-369.

Maxwell, Adam D., et al. "Cavitation clouds created by shock scattering from bubbles during histotripsy." The Journal of the Acoustical Society of America 130.4 (2011): 1888-1898.

Medwin, H. "Counting bubbles acoustically: a review." Ultrasonics 15.1 (1977): 7-13.

Mettin, R., et al. "Bjerknes forces between small cavitation bubbles in a strong acoustic field." Physical review E 56.3 (1997): 2924.

Mettin, R., et al. "Acoustic cavitation structures and simulations by a particle model." Ultrasonics Sonochemistry 6.1 (1999): 25-29.

Moholkar, Vijayanand S., Sander Rekveld, and Marijn MCG Warmoeskerken. "Modeling of the acoustic pressure fields and the distribution of the cavitation phenomena in a dual frequency sonic processor." Ultrasonics 38.1 (2000): 666-670.

Moholkar, Vijayanand S. "Mechanistic optimization of a dual frequency sonochemical reactor." Chemical Engineering Science 64.24 (2009): 5255-5267.

Mollica, Francesco, Luigi Preziosi, and Kumbakonam Ramamani Rajagopal. Modeling of biological materials. Springer Science & Business Media, 2007.

Nayfeh, Ali H., and Dean T. Mook. Nonlinear oscillations. John Wiley & Sons, 1979.

Neppiras, Ernest A. "Acoustic cavitation." Physics Reports 61.3 (1980): 159-251.

Newhouse, V. L., and P. Mohana Shankar. "Bubble size measurements using the nonlinear mixing of two frequencies." The Journal of the Acoustical Society of America 75.5 (1984): 1473-1477.

Newman, C. M. H., and T. Bettinger. "Gene therapy progress and prospects: ultrasound for gene transfer." Gene therapy 14.6 (2007): 465-475.

Nikitenko, S. I., et al. "Potential applications of sonochemistry in spent nuclear fuel reprocessing: a short review." Ultrasonics sonochemistry 17.6 (2010): 1033-1040.

Oguz, Hasan N., and Andrea Prosperetti. "A generalization of the impulse and virial theorems with an application to bubble oscillations." Journal of Fluid Mechanics 218 (1990): 143-162.

Ott, Edward. Chaos in dynamical systems. Cambridge university press, 2002.

Parlitz, U., et al. "Bifurcation structure of bubble oscillators." The Journal of the Acoustical Society of America 88.2 (1990): 1061-1077.

Pelekasis, Nikolaos A., et al. "Secondary Bjerknes forces between two bubbles and the phenomenon of acoustic streamers." Journal of Fluid Mechanics 500 (2004): 313-347.

Pelekasis, Nikolaos A., and John A. Tsamopoulos. "Bjerknes forces between two bubbles. Part 1. Response to a step change in pressure." Journal of Fluid Mechanics 254 (1993a): 467-499.

Pelekasis, Nikolaos A., and John A. Tsamopoulos. "Bjerknes forces between two bubbles. Part 2. Response to an oscillatory pressure field."

Journal of Fluid Mechanics 254 (1993b): 501-527.

Phelps, A. D., and T. G. Leighton. "Investigations into the use of two frequency excitation to accurately determine bubble sizes." Bubble Dynamics and Interface Phenomena. Springer Netherlands, 1994. 475-484.

Plesset, Milton S., and Andrea Prosperetti. "Bubble dynamics and cavitation." Annual Review of Fluid Mechanics 9.1 (1977): 145-185.

Prosperetti, A. "Bubble phenomena in sound fields: part one." Ultrasonics 22.2 (1984a): 69-77.

Prosperetti, A. "Bubble phenomena in sould fields: part two." Ultrasonics 22.3 (1984b): 115-124.

Prosperetti, Andrea. "Thermal effects and damping mechanisms in the forced radial oscillations of gas bubbles in liquids." The Journal of the Acoustical Society of America 61.1 (1977): 17-27.

Prosperetti, Andrea, Lawrence A. Crum, and Kerry W. Commander. "Nonlinear bubble dynamics." The Journal of the Acoustical Society of America 83.2 (1988): 502-514.

Prosperetti, Andrea. "Nonlinear oscillations of gas bubbles in liquids: steady-state solutions." The Journal of the Acoustical Society of America 56.3 (1974): 878-885.

Putterman, S. J., and K. R. Weninger. "Sonoluminescence: How bubbles

turn sound into light." Annual Review of Fluid Mechanics 32.1 (2000): 445-476.

Rychak, Joshua J., Alexander L. Klibanov, and John A. Hossack. "Acoustic radiation force enhances targeted delivery of ultrasound contrast microbubbles: in vitro verification." Ultrasonics, Ferroelectrics and Frequency Control, IEEE Transactions on 52.3 (2005): 421-433.

Sauter, C., et al. "Influence of hydrostatic pressure and sound amplitude on the ultrasound induced dispersion and de-agglomeration of nanoparticles." Ultrasonics sonochemistry 15.4 (2008): 517-523.

Servant, G., et al. "On the interaction between ultrasound waves and bubble clouds in mono-and dual-frequency sonoreactors." Ultrasonics Sonochemistry 10.6 (2003): 347-355.

Shah, Yatish T., A. B. Pandit, and V. S. Moholkar. Cavitation reaction engineering. Springer, 1999.

Shankar, P. M., J. Y. Chapelon, and V. L. Newhouse. "Fluid pressure measurement using bubbles insonified by two frequencies." Ultrasonics 24.6 (1986): 333-336.

Shaw, Stephen J. "Translation and oscillation of a bubble under axisymmetric deformation." Physics of Fluids (1994-present) 18.7 (2006): 072104.

Shortencarier, Michaelann J., et al. "A method for radiation-force

localized drug delivery using gas-filled lipospheres." Ultrasonics, Ferroelectrics and Frequency Control, IEEE Transactions on 51.7 (2004): 822-831.

Simon, G., et al. "Periodic orbit theory applied to a chaotically oscillating gas bubble in water." Nonlinearity 15.1 (2002): 25.

Sivakumar, Manickam, Prashant A. Tatake, and Aniruddha B. Pandit. "Kinetics of p-nitrophenol degradation: effect of reaction conditions and cavitational parameters for a multiple frequency system." Chemical Engineering Journal 85.2 (2002): 327-338.

Song, Yizhi, et al. "Ultrasound-mediated DNA transfer for bacteria." Nucleic acids research 35.19 (2007): e129.

Storey, Brian D., and Andrew J. Szeri. "Water vapour, sonoluminescence and sonochemistry." Proceedings of the Royal Society of London. Series A: Mathematical, Physical and Engineering Sciences 456.1999 (2000): 1685-1709.

Suslick, Kenneth S., and David J. Flannigan. "Inside a collapsing bubble: sonoluminescence and the conditions during cavitation." Annu. Rev. Phys. Chem. 59 (2008): 659-683.

Sutin, A. M., et al. "Nonlinear acoustic method for bubble density measurements in water." The Journal of the Acoustical Society of America 103.5 (1998): 2377-2384.

Szeri, Andrew J., and L. Gary Leal. "The onset of chaotic oscillations and rapid growth of a spherical bubble at subcritical conditions in an incompressible liquid." Physics of Fluids A: Fluid Dynamics (1989-1993) 3.4 (1991): 551-555.

Tamura, Takahiro, Naohiko Inaba, and Juichi Miyamichi. "Mechanism for taming chaos by weak harmonic perturbations." Physical review letters 83.19 (1999): 3824.

Tatake, Prashant A., and Aniruddha B. Pandit. "Modelling and experimental investigation into cavity dynamics and cavitational yield: influence of dual frequency ultrasound sources." Chemical Engineering Science 57.22 (2002): 4987-4995.

Ter Haar, G. R., and S. Daniels. "Evidence for ultrasonically induced cavitation in vivo." Physics in medicine and biology 26.6 (1981): 1145.

Vichare, Nilesh P., et al. "Energy analysis in acoustic cavitation." Industrial & engineering chemistry research 39.5 (2000): 1480-1486.

Waghmare, Y. G., F. Carl Knopf, and Richard G. Rice. "The Bjerknes effect: Explaining pulsed‐flow behavior in bubble columns." AIChE journal 53.7 (2007): 1678-1686.

Wagterveld, R. M., et al. "Visualization of acoustic cavitation effects on suspended calcite crystals." Ultrasonics sonochemistry 18.1 (2011): 216-225.

Webb, Ian R., Stephen J. Payne, and Constantin-C. Coussios. "Effect of temperature on rectified diffusion during ultrasound-induced heating." The Journal of the Acoustical Society of America 130.5 (2011): 3450-3457.

Weston, Di E. "Sound propagation in the presence of bladder fish." Underwater acoustics 2 (1967): 55-88.

Wildt, R. "Acoustic theory of bubbles." Physics of Sound in the Sea 8 (1946): 460-477.

Wolfrum, B., et al. "Luminescence of transient bubbles at elevated ambient pressures." Physical Review E 64.4 (2001): 046306.

Wu, Chung-Yuo, Jenho Tsao, and Yi-Hong Chou. "An ultrasonic microbubble semi-intermodulated imaging technique." Ultrasound in medicine & biology 31.9 (2005): 1199-1210.

Wu, Junru, Jason Pepe, and William Dewitt III. "Nonlinear behaviors of contrast agents relevant to diagnostic and therapeutic applications." Ultrasound in medicine & biology 29.4 (2003): 555-562.

Wyczalkowski, Matthew, and Andrew J. Szeri. "Optimization of acoustic scattering from dual-frequency driven microbubbles at the difference frequency." The Journal of the Acoustical Society of America 113.6 (2003): 3073-3079.

Xu, Zhen, et al. "Controlled ultrasound tissue erosion." Ultrasonics, Ferroelectrics and Frequency Control, IEEE Transactions on 51.6 (2004):

726-736.

Yang, Xinmai, and Charles C. Church. "A model for the dynamics of gas bubbles in soft tissue." The Journal of the Acoustical Society of America 118.6 (2005): 3595-3606.

Yasuda, Keiji, et al. "Enhancement of sonochemical reaction of terephthalate ion by superposition of ultrasonic fields of various frequencies." Ultrasonics sonochemistry 14.6 (2007): 699-704.

Yoo, Hee Ju, and Chang Dae Han. "Oscillatory behavior of a gas bubble growing (or collapsing) in viscoelastic liquids." Aiche Journal 28.6 (1982): 1002-1009.

Yoshida, Kenji, Takaaki Fujikawa, and Yoshiaki Watanabe. "Experimental investigation on reversal of secondary Bjerknes force between two bubbles in ultrasonic standing wave." The Journal of the Acoustical Society of America 130.1 (2011): 135-144.

Zhang, Yuning. "A generalized equation for scattering cross section of spherical gas bubbles oscillating in liquids under acoustic excitation." Journal of Fluids Engineering 135.9 (2013a): 091301.

Zhang, Yuning. "Heat transfer across interfaces of oscillating gas bubbles in liquids under acoustic excitation." International Communications in Heat and Mass Transfer 43 (2013b): 1-7.

Zhang, Yuning, Analysis of radial oscillations of gas bubbles in Newtonian

or viscoelastic mediums under acoustic excitation (Ph.D. Thesis), University of Warwick, 2012a.

Zhang, Yuning. "Rectified mass diffusion of gas bubbles in liquids under acoustic field with dual frequencies." International Communications in Heat and Mass Transfer 39.10 (2012b): 1496-1499.

Zhang, Yuning, Duncan Billson and Shengcai Li. "Influences of pressure amplitudes and frequencies of dual-frequency acoustic excitation on the mass transfer across interfaces of gas bubbles." International Communications in Heat and Mass Transfer (2015), in press.

Zhang, Yuning and Xiaoze Du. “Effects of liquid compressibility on the secondary Bjerknes force between oscillating cavitation bubbles.” Ultrasonics Sonochemistry (2015), under review.

Zhang, Yuning and Shengcai Li. "Acoustical Scattering Cross Section of Gas Bubbles under Dual-Frequency Acoustic Excitation." Ultrasonics Sonochemistry (2015), in press.

Zhang, Yuning and Shengcai Li. " The secondary Bjerknes force between two oscillating gas bubbles under dual-frequency acoustic excitation." Ultrasonics Sonochemistry (2015), under review.

Zhang, Yuning, and S. C. Li. "Notes on radial oscillations of gas bubbles in liquids: Thermal effects." The Journal of the Acoustical Society of America 128.5 (2010): EL306-EL309.

Zhang, Yuning, and Shengcai Li. "Thermal effects on nonlinear radial oscillations of gas bubbles in liquids under acoustic excitation." International Communications in Heat and Mass Transfer 53 (2014a): 43-49.

Zhang, Yuning, and Shengcai Li. "A general approach for rectified mass diffusion of gas bubbles in liquids under acoustic excitation." Journal of Heat Transfer 136.4 (2014b): 042001.

Zheng, Hairong, et al. "Advantages in using multifrequency excitation of contrast microbubbles for enhancing echo particle image velocimetry techniques: initial numerical studies using rectangular and triangular waves." Ultrasound in medicine & biology 31.1 (2005): 99-108.